A Systematic Study of Silicon Germanium Interdiffusion for Next Generation Semiconductor Devices

by

Yuanwei Dong

M.Sc., Fudan University, 2009

A THESIS SUBMITTED IN PARTIAL FULFILLMENT OF

THE REQUIREMENTS FOR THE DEGREE OF

DOCTOR OF PHILOSOPHY

in

The Faculty of Graduate and Postdoctoral Studies

(Materials Engineering)

THE UNIVERSITY OF BRITISH COLUMBIA

(Vancouver)

July 2014

Abstract

SiGe heterostructures with higher Ge fractions and larger Ge modulations, and thus higher compressive stress, are key structures for next-generation electronic and optoelectronic devices. Si-Ge interdiffusion during high temperature growth or fabrication steps changes the distribution of Ge fraction and stress, and increases atomic intermixing, which degrades device performance. It is of technological importance to study Si-Ge interdiffusion behaviours and build accurate Si-Ge interdiffusivity models.

In this work, three aspects of Si-Ge interdiffusion behaviours were investigated both by experiments and by theoretical analysis.

1) Based on the correlation between self-diffusivity, intrinsic diffusivity and interdiffusivity in binary alloy systems, a unified interdiffusivity model was built over the full Ge fraction range. It provides a zero-strain, no-dopant-effect, and low-dislocation-density reference for studies of more impacting factors. This model was then validated with literature data and our experimental data using different annealing techniques.

Next, with the well-established reference, the impact of biaxial compressive strain on Si-Ge interdiffusion was further investigated under two specific strain scenarios: with full coherent strain and with partial strain.

2) Complete theoretical analysis was presented to address the compressive strain's role in Si-Ge interdiffusion. The role of compressive strain was modeled in two aspects: a) strain energy contributes to the interdiffusion driving force; b) the strain derivative q' of interdiffusivity, reflecting the strain-induced changes of both prefactor and activation energy. For the temperature range (720 °C to 880 °C) and Ge fraction range (0.36 to 0.75), a temperature

dependence of the strain derivative q', q'=-0.081T+110 eV/unit strain, was reported in Si-Ge interdiffusion.

3) For the case with partial strain, the apparent interdiffusivity model developed for the case with full coherent strain in 2) was modified to reflect strain change, and it was then validated with experimental data.

In summary, a set of interdiffusivity models were established based on experimental data and theoretical analysis for three strain scenarios. These models can be employed to predict the thermal stability of SiGe heterostructures, and optimize the design of SiGe structures and of thermal budgets for next-generation SiGe based devices.

Preface

The work in this thesis was funded by Natural Science and Engineering Research Council of Canada (NSERC), Crosslight Software Inc. (Vancouver, BC) and the Four Year Fellowship awarded by Department of Materials Engineering at the University of British Columbia (UBC). Most of the work has been done in Department of Materials Engineering at UBC in the past three years, including the designs of experiments, the strain analysis with Raman spectroscopy, the thermal anneals with Linkam heating stage and the TSUPREM-4^{TM} simulations. All the theoretical modeling and simulations were conducted by the author. Experimentally, the author designed the sample structures and all the annealing conditions, prepared samples for secondary ion mass spectrometer (SIMS), and performed X-ray diffraction (XRD) and Raman measurements, and the data analysis of those characterizations. Without the contributions from the collaborators, however, this thesis could not have been accomplished.

All the samples were grown by Mr. G. Riggott at Microsystems Technology Laboratories of Prof. J. L. Hoyt's group at Massachusetts Institute of Technology (MIT). Moreover, the tube furnace anneals were performed by Mr. W. Chern in Exploratory Materials Laboratory (EML) at MIT.

The advanced rapid thermal anneals (RTA) such as soak and spike RTA were carried out by Mr. J. Chan and Mr. S. McCoy in Mattson Technology Canada (Vancouver, BC).

The SIMS measurements were performed by Dr. G. Goodman and Mr. S. Smith in Evans Analytical Group (EAG), a provider of commercial material characterizations. The sample preparation and the analysis of the SIMS data were performed by the author.

XRD measurements were performed by the author upon a PANalytical X'Pert PRO MRD tool in Semiconductor Defect Spectroscopy Laboratory led by Prof. P. Mooney at Simon Fraser

University. All the data analysis and simulations with software Epitaxy were carried out by the author.

The measurements of dislocation density with the etch pit density (EPD) technique were performed by the author in the AMPEL Nanofabrication Facility. In addition, the interpretation and quantitative analysis of those EPD images were made by the author.

In addition, two journal articles have been published based on the work in Chapter 4 and 5. A book chapter including the same work has been submitted, and is currently under edition. Another journal article will be submitted soon based on the work in Chapter 6.

1) **Yuanwei Dong**, Yiheng Lin, Simon Li, Steve McCoy and Guangrui Xia, *A unified interdiffusivity model and model verification for tensile and relaxed Si-Ge interdiffusion over the full germanium content range.* Journal of Applied Physics, 2012. **111**(4): p. 044909.
2) **Yuanwei Dong**, Winston Chern, Patricia M Mooney, Judy L Hoyt and Guangrui (Maggie) Xia, *On the role and modeling of compressive strain in Si-Ge interdiffusion for SiGe heterostructures*, Semiconductor Science and Technology, 2014. **29** (1)**:** p.015012.
3) **Yuanwei Dong,** Patricia M Mooney, Feiyang Cai and Guangrui (Maggie) Xia, *Modeling of Si-Ge interdiffusion under partial strain relaxation in epitaxial SiGe heterostructures*, under review by ECS Journal of Solid State Science and Technology.
4) Guangrui (Maggie) Xia, **Yuanwei Dong,** Book Chapter: *Si-Ge interdiffusion, dopant diffusion and segregation in SiGe and SiGe: C based devices*, under edition for the book of *Emerging Semiconductors Devices and Technology* edited by Tomasz Brozek and Kris Iniewski, 2014, to be published by CRC Press.

Table of Contents

List of Tables

List of Figures

Acknowledgements

"What I cannot create, I do not understand."

—Richard P. Feynman

First, I would like to express my gratitude to Prof. Guangrui Xia, my advisor, for guidance, patience and trust in me throughout the career of my Ph.D. I really appreciate the flexibility in defining the course of this work and the opportunities to train me as an independent researcher provided by Prof. Xia.

I would like to express my appreciation to the members of my Ph.D committee, Chairman, Prof. Warren Poole, Prof. David Dixon, and Prof. Peter Barr. In my comprehensive exam in 2012, their insightful questions inspired me to think how to carry out the following research work on Si-Ge interdiffusion. In addition, I really appreciate the Four Year Fellowships awarded to me, which allow me engrossed in the research work.

I would also like to thank NSERC and Crosslight Software Inc. for supporting the work in this thesis.

I am very grateful to the Prof. Hoyt's group at MIT for their support and help in the structure design and growth of the SiGe samples. I learned a lot from the fruitful discussions with Prof. Hoyt. In addition, I am very thankful to Mr. Gary Riggott for growing the high-quality samples and to Mr. Winston Chern for doing tube furnace anneals at MIT.

Specially, I am so indebted to Prof. Mooney, not only for the free access to the XRD tool in her group, but also for the enlightening discussions during the XRD training and measurements, and the insightful comments and suggestions on my work. I can never forget the three days in

which Prof. Mooney trained me how to operate the XRD tool and how to use Epitaxy software. I am deeply touched and impressed by her great passion and rigorous attitudes in research work.

This work has been greatly benefited from many collaborators. I would like to thank Mr. J. Chan and Mr. S. McCoy in Mattson Technology Canada for performing soak and spike RTAs. Many thanks are to Dr. G. Goodman and Mr. S. Smith in Evans Analytical Group for useful discussions over SIMS analysis. I am also grateful to Dr. Simon Li, Dr. Leo Li, Dr. Fred Fu and Mr. Sheng Gao from Crosslight Software Inc. for their support in model implementation in CSUPREM and helpful discussions. Many thanks are to Mr. M. French from Intel for useful discussions on strain analysis for SiGe materials with Raman spectroscopy. I would like to thank Dr. Yew Heng Lin from Nanyang Technological University in Singapore for his great help in SiGe wet etching. Special thanks are to Dr. M. Beaudoin and Dr. A. Kulpa from AMPEL Nanofabrication Facility for their support and help during this work. I am surely thankful to Mr. Y. Lin and Mr. F. Cai in our group for their helps in this work.

Last but not the least, I would like to thank Hai Lin, my beloved wife, for her enduring encouragement and understanding in the past years. My parents have always supported me and my gratitude to them cannot be expressed in words. I would like to dedicate this thesis to my parents and my wife for all their love and support.

Dedication

To my parents and my wife

Chapter 1 Introduction

1.1 Background and motivations

As electronic and optoelectronic devices are continuously scaled down for better performance and larger densities, novel materials and process techniques have been developed and integrated into state-of-the-art semiconductor device manufacturing. In the last two decades, $Si_{1-x}Ge_x$ ($0 \leq x \leq 1$) alloys have become key materials in electronic devices. Examples are source/drain stressors to enhance carrier mobilities [1] or channel materials in p-type metal-oxide-semiconductor field-effect transistors (MOSFETs) for a higher hole mobility [2, 3], the tunnelling layer in tunnelling FETs [4], and the quantum wells in resonant tunnelling diodes [5]. For optoelectronic application, SiGe alloys and pure Ge are also employed in modulators [6], Ge photodiodes [7, 8] and Ge/Si lasers [9]. $Si/Si_{1-x}Ge_x$ and $Si_{1-x}Ge_x/Si_{1-y}Ge_y$ heterostructures with abrupt changes in Ge concentration have become key structures for many electronic and optoelectronic devices, as shown in Figure 1.1.

During the growth and fabrication of these devices, especially the ones that require high temperature processes, unavoidably, Si and Ge atoms interdiffuse at the interface between two layers in heterostructures. This interdiffusion increases exponentially with Ge concentration and compressive stress, and also increases with implant damages [10, 11]. Si-Ge interdiffusion is generally undesirable. It degrades MOSFET performance by reducing strain and carrier confinement, and by increasing alloy scattering [12]. It also decreases the photodetector efficiency [13], and delays the lasing of Ge/Si lasers [14]. Therefore, understanding Si-Ge interdiffusion behaviour is a topic with great technological significance, which is the goal of this work.

Si-Ge interdiffusion is becoming more and more significant in current technology, and an accurate interdiffusion model with wide application ranges is therefore in great need. Although many efforts have been devoted to measuring and modeling Si-Ge interdiffusivities in different Ge ranges and structures and to investigating microscopic interdiffusion mechanisms [10, 15-23], no unified Si-Ge interdiffusion model over the full Ge fraction range (0%-100%) has been established for SiGe thin films without strain. In addition, Si self-diffusion and Ge self-diffusion in SiGe homogeneous alloys have been investigated experimentally and theoretically [24-30]. However, until now, no quantitative correlation between Si-Ge interdiffusivity and Si, Ge self-interdiffusivities has been established. On the other hand, most of the studies on Si-Ge interdiffusion so far have mainly focused on the interdiffusion under furnace anneal conditions, which have isothermal temperature profiles. In the semiconductor industry, however, advanced anneal techniques, such as soak rapid thermal anneals (RTA), spike RTAs and flash RTAs, are being used as the mainstream anneal techniques. The latter two RTA techniques are generally non-isothermal, and RTA techniques have much faster ramp rates and shorter anneal times at the peak temperature than furnace anneals. Because of the wide industrial applications of SiGe alloys, a comprehensive model for Si-Ge interdiffusion over the full Ge fraction range and applicable to soak and spike RTAs is in great demand, and is of great technical significance for structure designs and thermal budget designs of advanced SiGe devices.

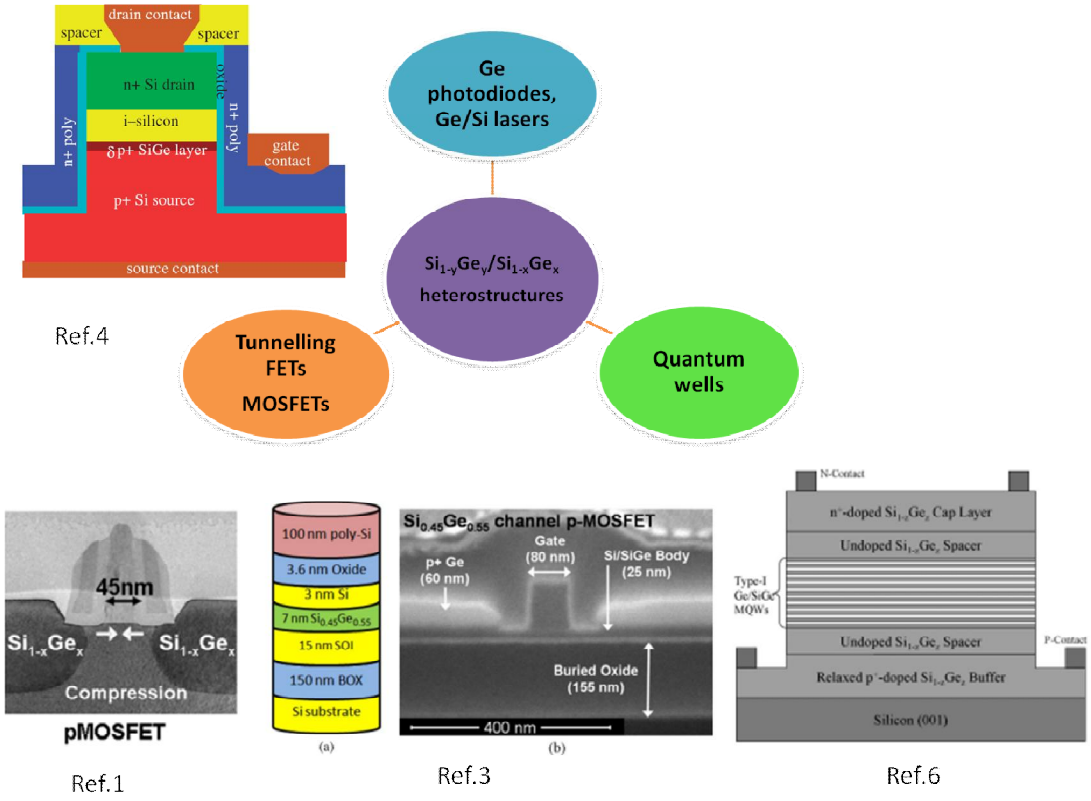

Figure 1.1 Basic structures of electronic and optoelectronic devices based on SiGe heterostructures.

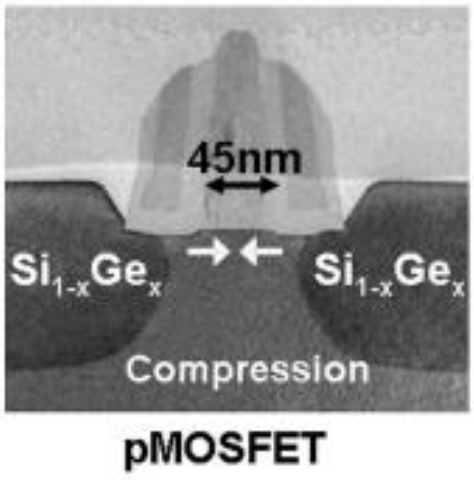

Figure 1.2 TEM image of a p-type MOSFET with $Si_{1-x}Ge_x$ as source and drain. Reprinted with permission from Ref. [1]. Copyright © 2004 IEEE.

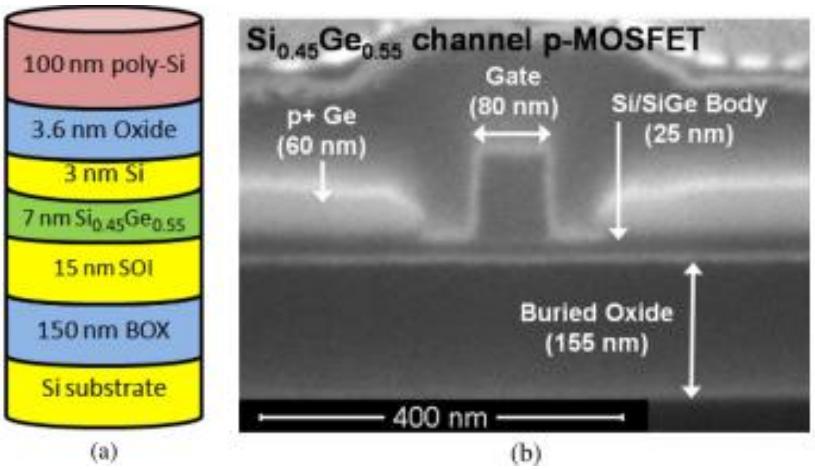

Figure 1.3 (a) Schematic gate stack of a strained SiGe p-MOSFET; (b) SEM image of strained SiGe p-MOSFET. Reprinted with permission from Ref. [3]. Copyright © 2009 IEEE.

Compressive strain has been widely applied in SiGe devices to enhance their performance. As shown in Figure 1.2, in a p-type MOSFET (p-MOSFET), SiGe is generally employed as a source or drain to introduce compressive strain, which can enhance the hole mobility in the Si channel by >50% [1]. SiGe is also an important material for MOSFETs' channels. In Figure 1.3, a typical strained SiGe p-MOSFET is shown, which employed a thin SiGe film under the high compressive strain with Ge fraction up to 0.55 [3]. Compressive strain can increase carrier mobilities significantly; in the meantime, it also has a significant impact on Si-Ge interdiffusion. Strain can enhance or retard the diffusion of dopants as well as Si-Ge interdiffusion. For SiGe, tensile strain has a negligible impact on Si-Ge interdiffusivity while compressive strain can enhance Si-Ge interdiffusivity considerably, as reported by G. Xia *et al.* [10]. However, G. Xia *et al*.'s work only focused on the interdiffusivity in a limited Ge fraction range (x_{Ge}≤0.56). An accurate interdiffusion model for the interdiffusion under compressive strain over a wider Ge fraction range is still lacking. Moreover, in real devices, it is very common that the compressive strain relaxes during high temperature steps. Few studies are reported on the Si-Ge interdiffusion with strain relaxation.

1.2 Significance of interdiffusion in SiGe heterostructures

Interdiffusion in SiGe heterostructures has a significant impact on the performance of SiGe based devices.

1) Alloy scattering due to Ge out-diffusion into a Si channel can degrade carrier mobilities severely (more severely for electrons than holes) in strained Si metal-oxide-semiconductor field effect transistors (MOSFETs) on relaxed SiGe virtual substrates [31-33]. Currie *et al.* demonstrated that both electron mobilities and hole mobilities were degraded due to the interdiffusion under a series of rapid thermal anneals (RTA) [33]. In their work, it was pointed out that the increased Ge fraction in the channel degraded the mobilities via many scattering effects. In addition, the diffused Ge atoms from the virtual substrates could reach the Si/SiO_2 interface and increase the interface state density there, which also degrades the performance of a transistor.

2) When Ge concentrations decrease due to interdiffusion during the fabrication processes involving high thermal budgets such as the activation of the implanted dopants in source/drain or channel regions, the mismatch strains designed to enhance carrier mobilities become lower. This adverse impact is significant for dual-channel p-MOSFETs consisting of strained Si and $Si_{1-y}Ge_y$ ($y > x$) layers on relaxed $Si_{1-x}Ge_x$ virtual substrates. It was evidently shown that the hole mobility in the compressive $Si_{1-y}Ge_y$ (y=0.80) layers was degraded under a higher source/drain anneal temperature (800 °C, 30mins) [12]. At an effective field of 0.3 MV/cm, the hole mobility enhancement factor decreased from 3.6X to 2.3X due to Ge fraction decrease during the anneal. Moreover, it was found that hole mobilities are highly susceptible, but electron mobilities are more immune to the anneal conditions.

3) Interdiffusion at hetero-interfaces deteriorates the interface abruptness. An abrupt interface is critical to maintain good electron/hole confinements in superlattice structures such as multiple quantum wells for optoelectronic devices. Si-Ge interdiffusion at the interfaces can change the shape of the quantum well potentials [34]. The change in well width and well depth caused by interdiffusion can modify the subband energy levels in quantum wells. It was reported that the activation energy of hole emission from $Si/Si_{0.60}Ge_{0.40}$ quantum wells decreased as the annealing time increased [34]. Moreover, in the study on Ge-on-SOI (silicon-on-insulator) by Dehlinger *et al*, they found that there was a noticeable discrepancy between the measured quantum efficiency and the theoretical prediction, which was attributed to the gradual SiGe layer at the Ge/Si interface caused by interdiffusion [13].

Considering all the adverse impacts on SiGe based devices, it is crucial to get a better understanding of Si-Ge interdiffusion, in order to design appropriate structures and thermal budgets, especially for SiGe devices with higher Ge fractions. Therefore, this thesis discusses several important aspects introduced in Section 1.1, and furthers the understanding of Si-Ge interdiffusion.

1.3 Scope of the thesis

In this thesis, after the discussion of theoretical fundamentals (such as solution models, diffusion theories etc.) and experimental aspects (such as the design and growth of samples, characterization techniques of Ge fraction and strain etc.) in Chapter 2 and 3, Chapter 4 to 6 focus on the study of Si-Ge interdiffusion behaviours without strain, with full coherent strain and with partial strain.

In Chapter 4, based on the correlation between Si-Ge interdiffusivity and Si, Ge self-diffusivities, a unified Si-Ge interdiffusion model is built theoretically over the full Ge fraction range ($0 \leq$

$x_{Ge} \leq 1$) for the interdiffusion under zero strain. The parameters of the model are calculated based on the data of Si and Ge self-diffusivities from Kube *et al*'s work [29, 30]. The validity of the new model is confirmed by the experiments conducted under rapid thermal anneal (soak RTA and spike RTA) conditions. The no-strain interdiffusion model serves as the basis for the work in Chapter 5, where the role of the compressive strain in Si-Ge interdiffusion is investigated.

In Chapter 5, the impact of the compressive strain on Si-Ge interdiffusion is investigated in the medium Ge range both by experiments and by modeling and simulations. The Ge fraction and strain in each layer of the samples are well characterized with secondary ion mass spectrometry (SIMS), Raman spectroscopy and X-ray diffraction (XRD). In addition, the threading dislocation density (TDD) is measured by the etch pit density technique to rule out the impact of the TDD on interdiffusion. It is demonstrated that the compressive strain enhances Si-Ge interdiffusion and the strain derivative q' of interdiffusivity has a temperature dependence. The two main roles of the biaxial compressive strain in Si-Ge interdiffusion are clarified for the first time: 1) strain energy gradient contributes to the driving force of interdiffusion and 2) strain can change the interdiffusivity itself.

In Chapter 6, with the two ideal interdiffusivity boundaries (without strain in Chapter 4 and with full strain in Chapter 5), the interdiffusion under partial strain is investigated. Some new light is shed on the complicated correlation between interdiffusion, strain relaxation and dislocations. Strain relaxation makes the strain enhancement of Si-Ge interdiffusion less effective. The Si-Ge interdiffusion under this condition can be modeled with an average degree of relaxation R.

To summarize, this thesis provides practical models to predict the interdiffusion for three different strain scenarios, which is very helpful in the design and the growth of SiGe heterostructures, and the design of thermal conditions in device fabrication.

Chapter 2 Material Properties and Theoretical Fundamentals

2.1 Material properties of Si, SiGe alloy and Ge

Silicon and germanium belong to the IVA group in the periodic table. They have the same crystalline structure (diamond cubic structure), and both have four valence electrons. Therefore, Si and Ge have similar physical properties such as self-diffusivity, Young's modulus, Poisson ratio etc. For single crystals, the lattice constant of Ge is larger than that of Si, $\frac{a_{Ge}}{a_{Si}}$ =1.0418, and the lattice constant of $Si_{1-x}Ge_x$ alloys has a nearly linear correlation with x. Thus, strain can be introduced by lattice mismatch between SiGe layers with different compositions. On the other hand, due to the same distribution of their outermost electrons, Si and Ge have similar chemical properties. Si and Ge are miscible over the complete range of Ge atomic fraction, so the $Si_{1-x}Ge_x$ alloy can be formed over the entire Ge fraction range and forms a random solid solution. The phase diagram of the Si and Ge binary system is shown in Figure 2.1 [35].

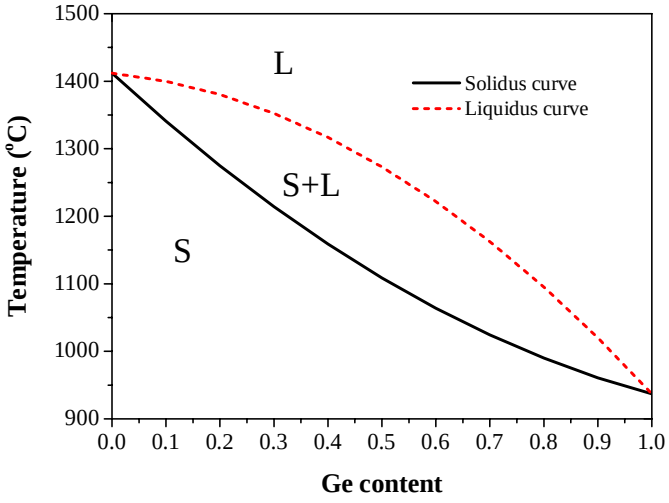

Figure 2.1 The phase diagram of Si-Ge system.

Most of the material properties of $Si_{1-x}Ge_x$ alloys, show a linear dependence of Ge fraction, which can be empirically expressed linearly with the properties of each constituent Si and Ge, $P_{Si_{1-x}Ge_x} = P_{Si}(1 - x_{Ge}) + P_{Ge}x_{Ge}$. For some cases, a quadratic equation is employed for further accuracy. The properties of $Si_{1-x}Ge_x$ alloys used in this thesis are shown as follows:

1) Lattice constant (modified Vegard's law) [36]:

   At 300 K, $a_{Si_{1-x}Ge_x} = 5.431 + 0.20x_{Ge} + 0.027x_{Ge}^2$ Å 2.1

2) Atomic density:

   $AD_{Si_{1-x}Ge_x} = AD_{Si}(1 - x_{Ge}) + AD_{Ge}x_{Ge} = (5.0 - 0.58x_{Ge}) \times 10^{22}/cm^3$ 2.2

3) Elastic properties: Young's modulus and Poisson's Ratio

   The crystalline structure of Si, SiGe and Ge makes the elastic properties four-fold symmetric, but the materials are anisotropic. The elastic properties of these materials will be important when considering strain shared between the layers of different compositions or crystalline orientations. In this work, the strain condition is restricted to the biaxial strain in the (100) plane, which corresponds to the pseudomorphic growth on a (100)-oriented substrate. For this case, Young's modulus and Poisson's ratio of SiGe alloys can be expressed as [37]

   $Y_{Si_{1-x}Ge_x} = Y_{Si}(1 - x_{Ge}) + Y_{Ge}x_{Ge}$ 2.3

   $\upsilon_{Si_{1-x}Ge_x} = \upsilon_{Si}(1 - x_{Ge}) + \upsilon_{Ge}x_{Ge}.$ 2.4

   At 300K [38],

   $Y_{Si_{1-x}Ge_x} = (130.2 - 28.1x_{Ge})\ GPa$;

   $\upsilon_{Si_{1-x}Ge_x} = 0.278 - 0.005x_{Ge}.$

2.2 Solution models for SiGe alloys

For solutions, the ideal solution model is the simplest one to describe solution behaviours, which is usually used to understand the thermodynamics of mixtures of ideal gases. For an ideal binary solution, the entropy of mixing per mole is

$$\Delta S_{mix}^{id} = -R_g(x_A ln x_A + x_B ln x_B) \quad 2.5$$

where x_A and x_B are the mole fractions of the A and B components, and R_g is the ideal gas constant.

The enthalpy of mixing is zero for an ideal solution, ΔH_{mix}^{id} = 0 [39]. Therefore, the Gibbs free energy of mixing per mole is

$$\Delta G_{mix}^{id} = \Delta H_{mix}^{id} - T\Delta S_{mix}^{id} = R_g T(x_A ln x_A + x_B ln x_B) \quad 2.6$$

where T is the absolute temperature.

For real solutions, other solution models were developed. The regular solution model is one of them. A regular solution is a solution that diverges from the behaviour of an ideal solution only moderately. In its simplest form, the definition of a regular solution contains two features [39]:

1) The entropy of mixing is the same as that for an ideal solution:

   $\Delta S_{mix}^{rs} = \Delta S_{mix}^{id} = -R_g(x_A ln x_A + x_B ln x_B)$ for a binary solution.

   where the superscript "rs" denotes a regular solution, and "id" denotes an ideal solution.
2) The enthalpy of mixing is not zero as in an ideal solution, but is some function of the composition: $\Delta H_{mix}^{rs} = \alpha x_A x_B$, where α is the interaction parameter.

Thus, the Gibbs free energy of mixing obtained from this model is

$$\Delta G_{mix}^{rs} = \Delta H_{mix}^{rs} - T\Delta S_{mix}^{rs} = \alpha x_A x_B + R_g T(x_A ln x_A + x_B ln x_B) \quad 2.7$$

Based on Feature 1, the excess entropy of mixing is zero for a regular solution. Here "excess" means the difference between the actual value of the solution and the value for an ideal solution. As a consequence of this definition, the excess molar Gibbs free energy is equal to the enthalpy of mixing.

$$(\Delta G_{mix}^{rs})^{xs} = \Delta H_{mix}^{rs} = \alpha x_A x_B \quad 2.8$$

where "xs" denotes the excess value.

For either A or B component, we can get the following equations [39]:

$$\Delta \bar{G}_A^{xs} = \Delta \bar{H}_A; \quad 2.9$$

$$\Delta \bar{G}_B^{xs} = \Delta \bar{H}_B. \quad 2.10$$

$$\bar{G}_A^{xs} = R_g T ln\gamma_A ; \quad 2.11$$

$$\bar{G}_B^{xs} = R_g T ln\gamma_B . \quad 2.12$$

$$\Delta \bar{H}_A = \alpha x_B^2 ; \Delta \bar{H}_B = \alpha x_A^2 \quad 2.13$$

where γ_A and γ_B, $\Delta \bar{H}_A$ and $\Delta \bar{H}_B$, $\Delta \bar{G}_A^{xs}$ and $\Delta \bar{G}_B^{xs}$ are the activity coefficient, partial molar enthalpy of mixing, and the excess partial molar Gibbs free energy of A and B components respectively.

Combined the three sets of Equations (2.9~2.13), we can obtain

$$\frac{\partial ln\gamma_A}{\partial ln x_A} = \frac{\partial ln\gamma_B}{\partial ln x_B} = \frac{-2\alpha x_A x_B}{R_g T}, \quad 2.14$$

which is the key equation to calculate the correlation factor between self-diffusivity and intrinsic diffusivity.

In this work, we use the regular solution model for SiGe solid solutions. In Section 4.2.3, $\frac{\partial ln\gamma_A}{\partial lnx_A}$ is calculated for the temperature range and the full Ge range used in our study. The value of $\frac{\partial ln\gamma_A}{\partial lnx_A}$ is in the range of 0 to 0.5, which is zero in the ideal solution model. Therefore, SiGe alloys should be considered as a regular solution instead of an ideal solution.

2.3 Diffusion laws and continuity equation

2.3.1 Fick's laws in isotropic materials

The equations governing diffusion processes in solid materials are Fick's laws: the first law and the second law. These two laws represent a continuum description and are purely phenomenological. In the first law, Fick introduced the concept of the diffusion coefficient (or diffusivity) and suggested a linear response between the concentration gradient and diffusion flux. It is easily generalised to three dimensions using a vector notation [40]:

$$\boldsymbol{J} = -D\nabla C, \tag{2.15}$$

where $\boldsymbol{J}$ is the diffusion flux, D is the diffusivity, and C is the concentration.

The diffusion flux $\boldsymbol{J}$ is opposite to the direction of the concentration gradient ∇C. Equation 2.15 applies to simple diffusion cases with chemical concentration gradients only. Complicated scenarios leading to modifications to Equation 2.15 may arise from anisotropy, elastic strain fields, external fields and high-diffusivity paths such as threading dislocations and grain boundaries [41].

Based on the conservation law, the mass balance (without sources and sinks) can be expressed as

Inflow-outflow=accumulation (or loss rate).

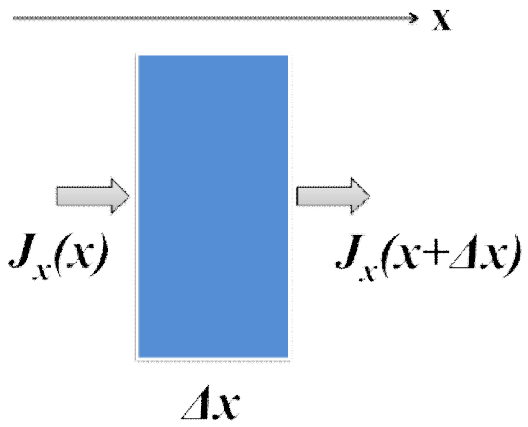

Figure 2.2 1D-infinitesimal test volume: the in- and outgoing x-component of the diffusion fluxes are indicated by arrow.

For one dimension diffusion flux, a test volume is set: Δx is an infinitesimal step along x axis, and S_{yz} is the cross-section area, shown in Figure 2.2. The mass balance can be expressed as

$$[J_x(x) - J_x(x+\Delta x)]S_{yz} = \frac{\partial C}{\partial t}\Delta x S_{yz} \qquad 2.16$$

Using Taylor expansions of the flux component along x axis, the expression in the square bracket of Equation 2.16 can be replaced by $-\Delta x \frac{\partial J_x}{\partial x}$. Then we can obtain

$$-\frac{\partial J_x}{\partial x} = \frac{\partial C}{\partial t} \qquad 2.17$$

The SiGe heterostructures we used in this work are all blanket thin film stacks on (100) Si substrates, and the diffusion we measured was along the [001] direction normal to the Si surface. So the diffusion studied in this thesis is one-dimensional diffusion.

For three-dimensional diffusion flux, the equation of continuity can be written in a compact form by introducing the vector operation $divergence\ \nabla \bullet$ as

$$-\nabla \bullet J = \frac{\partial C}{\partial t} \qquad 2.18$$

Combined Equation 2.15 and 2.18, Fick's second law obtained as

$$\frac{\partial C}{\partial t} = \boldsymbol{\nabla} \bullet (D \nabla C) \qquad 2.19$$

From a mathematical viewpoint, Fick's second law is a second-order partial differential equation. If the diffusivity is independent of concentration, Equation 2.19 can be simplified as $\frac{\partial C}{\partial t} = D\boldsymbol{\nabla}^2$C. This form of Fick's second law is sometimes called the linear diffusion equation. It is a linear second-order partial differential equation of the concentration. One can strive for solutions of this equation, if boundary and initial conditions are formulated. If the diffusivity is dependent on concentration, Equation 2.19 is non-linear. The concentration dependence of diffusivity can be extracted by Boltzmann-Matano method [42].

2.3.2 Validity of the continuity equation for multi-layers on the atomic scale

The continuity equation is valid for interdiffusion in crystalline materials at large scales. However, on the atomic scale, it becomes inaccurate. In 1969, Cook *et al* modeled the interdiffusion behaviours in modulated multi-layers (the schematic structure is shown in Figure 2.3) with a discrete solution. Comparing their results with the treatment of Cahn under a continuum approximation [43], they found that the continuum and discrete approximations give the same results only if the wavelength λ of the modulated structures is no less than six times of the inter-atomic spacing, d, in the direction of the diffusion ($\lambda \geq 6d$) [44, 45]. However, their conclusion is based on the linear approximation, assuming the diffusivity is independent on concentration. If the diffusivity is of strong concentration dependence, Erdélyi *et al* demonstrated that the validity of the continuity equation required a larger wavelength (by about one order of magnitude) in their investigation [46]. For simplicity, they selected an ideal binary solid solution. They specifically treated the case of diffusivity with an exponential dependence on concentration.

$$ln\frac{D(c)}{D(0)} = mc \qquad 2.20$$

where c is the atomic fraction of the component in the binary system that has $D(c) > D(0)$, $D(0)$ is the diffusivity at c = 0, and $D(c)$ is the diffusivity at c. Thus the coefficient m is ≥ 0.

To figure out the critical wavelength at which the continuum approach deviated from the discrete approach, they compared the decay of the height of the first order X-ray peaks by simulations using both discrete and continuum approaches. For m = 0 (a linear approximation), they found that the minimum wavelength for which the continuity equation is valid is $\lambda_c = 8d$. For (100) Silicon films, the inter-atomic spacing along the (001) direction of diffusion is one fourth of the lattice constant a, so λ_c equals to $2a$, about 1.1 nm. The critical wavelengths for larger m are shown in Figure 2.4, adjusted to the lattice parameter of Silicon [47].

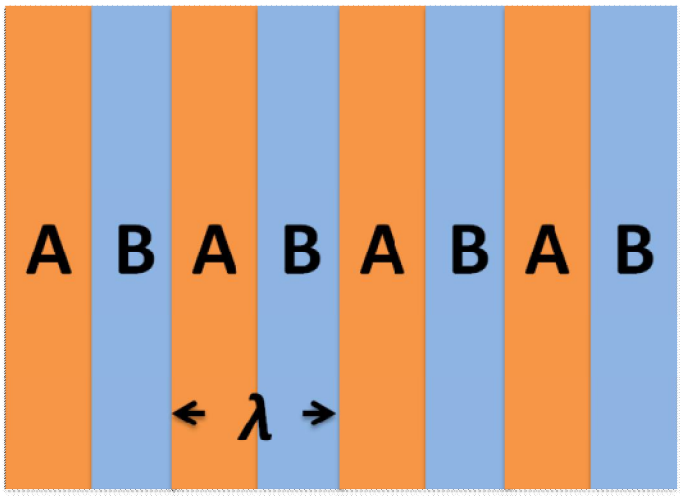

Figure 2.3 Schematic structure of modulated multi-layers. The wavelength λ is the thickness of the A/B bilayer.

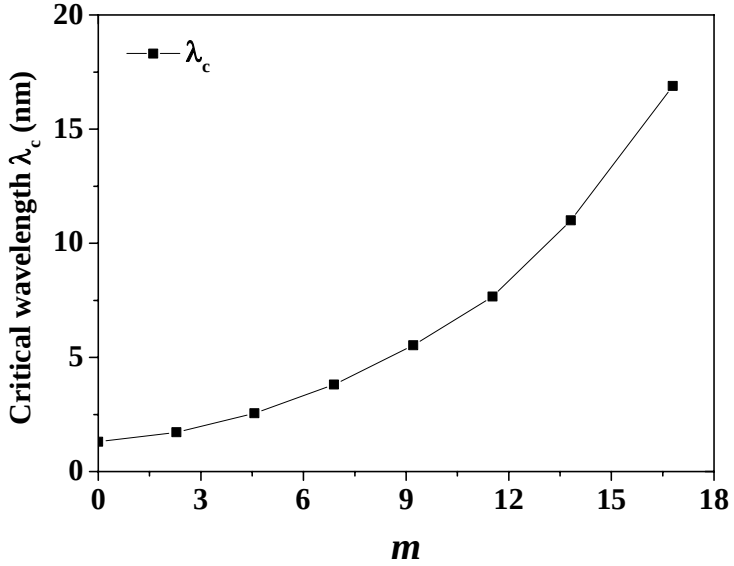

Figure 2.4 The critical wavelengths for which the continuity equation is valid for a concentration dependent diffusivity $D(c) = D(0)\exp(mc)$ at certain temperature for SiGe system, scaled from those for Mo-V system in Erdélyi *et al*'s work [46]**.**

For Si-Ge binary system, $\frac{D(1)}{D(0)}$ is around 10^5 over a wide temperature range (720°C~900°C) [48], so m is about 11.5. Accordingly, the critical wavelength is around 7.6 nm, which is close to the λ_c (≈8 nm) reported in Ref.[47]. The critical wavelength is crucial to interdiffusion studies with SiGe superlattice structures [15-20]. In this work, the thickness of the layers of interest (where interdiffusion happens) in the designed sample structures is larger than λ_c, so the continuum equation is applicable.

2.4 Definition of interdiffusion

2.4.1 Interdiffusion

When two species of atoms intermix, normally those two species tend to form a random solution to minimize the free energy. The rate of intermixing (or interdiffusion) depends on the diffusivity

of both species. For a better understanding, a binary diffusion couple (thick A layer/thick B layer) is used to interpret the concept of interdiffusion in Figure 2.5. After annealed at a temperature T for a duration, t, A and B atoms diffuse into each other. Relative to the frame fixed in the local crystal lattice, the intrinsic diffusion fluxes can be expressed by Fick's first law:

$$J_A = -D_A \frac{\partial C_A}{\partial x}; \qquad J_B = -D_B \frac{\partial C_B}{\partial x} \qquad 2.21$$

where D_A and D_B are the intrinsic diffusivities of A and B respectively.

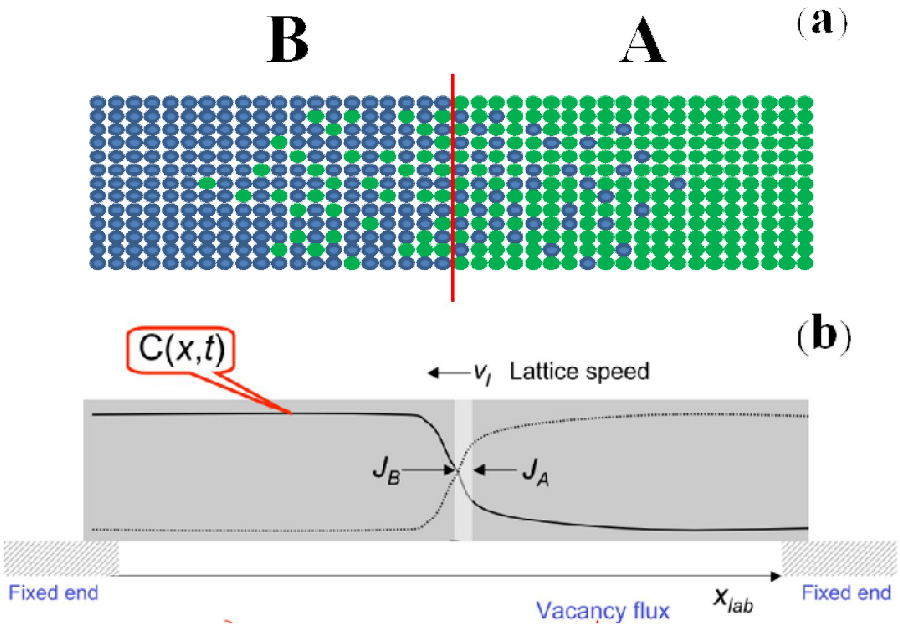

Figure 2.5 (a) Schematic diagram of a diffusion couple: A/B; (b) Schematic diagram of the diffusion fluxes of A and B at certain time point.

When D_A and D_B are unequal, the inequality of these two fluxes leads to a net mass flow accompanying the interdiffusion process, which causes the diffusion couple to shrink on one side and to swell on the other side. This observation is called Kirkendall effect, discovered by Kirkendall *et al* [49, 50]. In 1948, Darken gave the first theoretical interpretation of this effect. The lattice speed (Kirkendall velocity) can be expressed in terms of the intrinsic fluxes [51]:

$$\upsilon_L = -(J_A + J_B)\Omega \qquad 2.22$$

where υ_L is the lattice speed, and Ω is the molar volume, $\frac{1}{C_A+C_B}$.

Combined with Equation 2.21 and 2.22, we can obtain Darken's first equation for one dimension:

$$\upsilon_L = \Omega\left(\frac{\partial C_B}{\partial x}\right)(D_B - D_A) \; or \; \Omega\left(\frac{\partial C_A}{\partial x}\right)(D_A - D_B) \qquad 2.23$$

Following Darken's approach, the laboratory-fixed interdiffusion flux $\tilde{J}$ can be written as the sum of an intrinsic diffusion flux of either of the components plus a Kirkendall drift term:

$$\tilde{J} = J_i + \upsilon_L C_i = -D_i \frac{\partial C_i}{\partial x} + \upsilon_L C_i, \; i = A or \; B. \qquad 2.24$$

Insert Equation 2.23 into Equation 2.24 ($i = B$), we can obtain the interdiffusion flux and Darken's second equation:

$$\tilde{J} = -[D_A \Omega C_B + D_B(1 - \Omega C_B)]\frac{\partial C_B}{\partial x}, \qquad 2.25$$

then

$$\tilde{D} = x_B D_A + x_A D_B,$$

Where $\tilde{D}$ is the interdiffusivity, and x_A and x_B are the atomic fractions of A and B in the binary solution.

Darken equations are obtained under the assumption that the point defect concentration is under thermal equilibrium during the interdiffusion. There are enough vacancies to make the vacancy flux compensates the unequal fluxes of the A and B components. However, if there is a non-equilibrium vacancy distribution, the situation is different. Taking into account non-

equilibrium vacancies, Nazarov and Gurov performed an analysis of interdiffusion in binary alloys and found that the interdiffusion profile is governed by [52]:

$$\widetilde{D}_{Nazarov-Gurov} = \frac{D_A^* D_B^*}{x_A D_A^* + x_B D_B^*} \Phi \equiv \widetilde{D}_{Nernst-Planck} \quad 2.26$$

where D_A^* and D_B^* are the self-diffusivities of A and B respectively; Φ is the thermodynamic factor, $\Phi = 1 + \frac{\partial ln\gamma_A}{\partial lnx_A} = 1 + \frac{\partial ln\gamma_B}{\partial lnx_B}$.

The Nazarov-Gurov interdiffusivity expression in a binary alloy with non-equilibrium vacancies is identical to Nernst-Planck for interdiffusion in ionic crystals. In those non-equilibrium interdiffusion cases, there are no sufficient vacancies for interdiffusion, so the interdiffusion is dominated by the slower diffuser in the binary alloy. The interdiffusivity in Equation 2.26 is the effective interdiffusivity used to estimate the interdiffusion flux with Fick's diffusion laws.

Darken's second equation and Nernst-Planck equation (or Nazarov-Gurov equation) correspond to different time regimes. Darken's equation governs interdiffusion processes for long diffusion times [41].

The condition is fulfilled for Darken's equation when the average distance between vacancy sources and sinks, $\sqrt{D_V \tau_V}$, is small as compared to the width of the interdiffusion region, i.e.

$$\widetilde{D}_{Darken} t \gg D_V \tau_V \quad 2.27$$

where D_V denotes the vacancy diffusivity, and τ_V is the mean life-time of vacancies between their creation at vacancy sources and their annihilation at vacancy sinks.

For SiGe solid solutions, the interdiffusion process can be described by Darken's equation [47]. There are three reasons for that. First, the interfaces in SiGe heterostructures are not ideal. At the interface, there are extended defects such as misfit and threading dislocations, which can

act as sources and sinks of point defects. Second, the self-diffusivities of Si and Ge are very close [26-30], thus the vacancy flux is small based on Equation 2.23. Third, in Si, the mean life-time of vacancies is on the order of a few microseconds at typical annealing temperatures for semiconductor processing [53], and in addition, $\widetilde{D}_{Darken}$ and D_V are comparable [54]. Therefore, the anneal times used in our experiments ranging from tens of seconds to tens of minutes are long enough to meet the condition in Equation 2.27. Thus, in this work, the interdiffusion in SiGe solid solutions goes with Darken's equations.

2.5 Diffusion mechanisms in crystalline solids

In thin films, three types of diffusion paths are available [55].

1) Lattice diffusion mediated by point defects,
2) Dislocation mediated short-circuit diffusion, and
3) Grain boundary mediated short-circuit diffusion.

The SiGe thin film stacks we studied here are grown by an epitaxial method and are crystalline with a threading dislocation density around 10^4 to 10^6 cm^{-2}. Although defects exist, the film stacks are still single crystalline, not polycrystalline. Therefore, the 3) type does not need to be considered. In the following, we will discuss the other two diffusion paths.

2.5.1 Point defects: vacancy and interstitial

In crystalline solids including crystalline thin films in this work, two types of diffusion-relevant point defects are vacancies and interstitials. Vacancies and interstitials break the perfect lattice periodicity, and introduce certain "disorder" to minimize the free energy at thermal equilibrium. These two types of point defects can move through the crystal, acting as vehicles for diffusion of atoms. In metals, vacancies dominate the atomic diffusion. However, for semiconductors, not

only vacancies but also interstitials contribute to atomic diffusion [56]. For self-diffusion in semiconductors like Si and Ge, the atoms cannot diffuse directly through interstitial positions as small solute atoms do in larger lattice matrix atoms, such as carbon in iron. An indirect interstitial mechanism is dominant in self-diffusion, called “interstitialcy mechanism” [56]. In Figure 2.6 and Figure 2.7, the schematic diagrams of the atom movements through vacancy and interstitialcy mechanisms are shown.

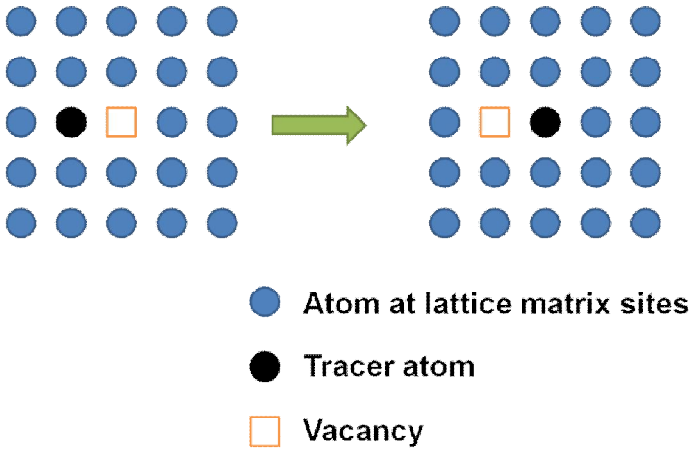

Figure 2.6 Schematic diagram of monovacancy mechanism of diffusion.

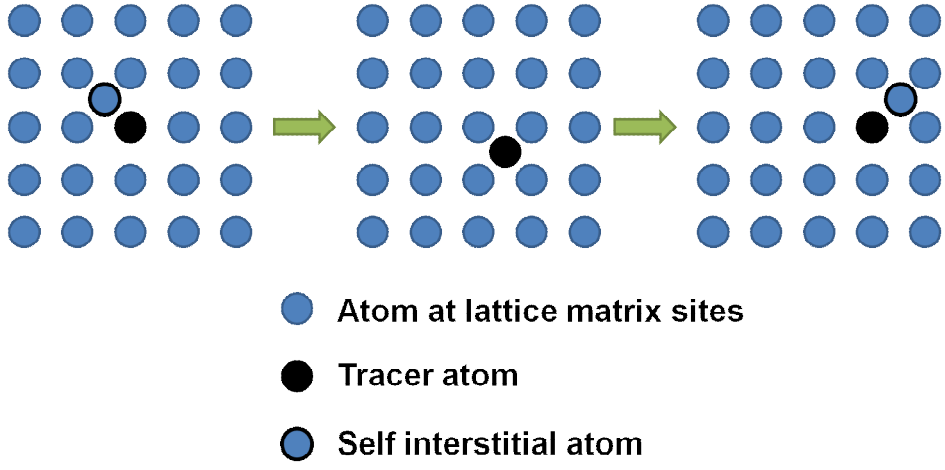

Figure 2.7 Schematic diagram of interstitialcy mechanism of diffusion.

In Figure 2.6, atoms can diffuse directly through vacancies. Under this diffusion mode, the diffusivity depends on the thermal concentration of vacancies, C_V^{eq}, and their diffusivity, D_V [40, 42].

$$C_V^{eq} = \exp\left(\frac{S_V^F}{k}\right)\exp\left(-\frac{H_V^F}{kT}\right)$$
$$D_V = g_V a_l^2 \nu_V^0 \exp\left(\frac{S_V^M}{k}\right)\exp\left(-\frac{H_V^M}{kT}\right) \quad 2.28$$

where H_V^F and H_V^M are the formation and migration enthalpies, S_V^F and S_V^M denote the respective entropies. g_V , a_l and ν_V^0 are the geometry factor, lattice constant and the vacancy attempt frequency.

In Figure 2.7, self-interstitial atoms act as diffusion vehicles. A self-interstitial replaces a tracer atom on a lattice site and pushes the tracer atom to an interstitial position. Then the tracer atom replaces a substitutional atom and pushes it into interstitial positions. Similarly under the interstitialcy diffusion mode, the diffusivity depends on the thermal concentration of self-interstitials, C_I^{eq}, and their diffusivity, D_I [40, 42].

$$C_I^{eq} = \exp\left(\frac{S_I^F}{k}\right)\exp\left(-\frac{H_I^F}{kT}\right)$$
$$D_I = g_I a_l^2 \nu_I^0 \exp\left(\frac{S_I^M}{k}\right)\exp\left(-\frac{H_I^M}{kT}\right) \quad 2.29$$

where H_I^F and H_I^M are the formation and migration enthalpies, S_I^F and S_I^M denote the respective enthopies. g_I , a_l and ν_I^0 are the geometry factor, lattice constant and the attempt frequency.

Taking into account both contributions of the vacancy and of the interstitialcy mechanism to self-diffusion, the tracer diffusivity can be expressed as

$$D^* = f_I C_I^{eq} D_I + f_V C_V^{eq} D_V + \underbrace{D_{ex}}_{\approx 0} \qquad 2.30$$

where f_I and f_V are the correlation factors for the interstitialcy mechanism and vacancy mechanism. D_{ex} denotes a possible contribution from the direct exchange of atoms at lattice sites. However, Blöchl *et al* demonstrated that D_{ex} is very small in silicon, four orders of magnitude less than interstitialcy mechanism, so normally D_{ex} is ignored [57].

In crystalline Si, intrinsic defects consist of vacancies and self-interstitials, so both vacancies and self-interstitials contribute to Si self-diffusion. In contrast, in crystalline Ge, vacancies predominate as intrinsic defects [56]. Thus, in Ge, the vacancy mechanism is predominant in self-diffusion.

2.5.2 Extended defects: dislocation

Extended defects are usefully classified by the number of dimensions in which they are extended, that is, of greater than the atomic size, into volume, surface and line defects [58]. For semiconductor thin films, grain boundaries and dislocations are the most frequently encountered extended defects, which have non-negligible impact on diffusion if their densities are high enough. In the devices based on SiGe thin films, the most important extended defects are threading dislocations (TDs) and misfit dislocations (MDs). MDs play a key role in strain relaxation in multilayered thin films while TDs can act as high diffusivity paths (pipe effect) for diffusions in thin films [59]. In epitaxial SiGe structures, the typical structure of those dislocations

is shown in Figure 2.8. MDs normally lie in the planes parallel to the surface while their TD arms go out of the planes and lie in the closely packed (111) planes.

Dislocations can degrade the performance of electronic devices, which are generally undesired in devices. This work focuses on the lattice diffusion, so the influence of these high diffusivity paths is unwanted also. Therefore, TDs should be minimized or at least reduced to a tolerable level for device applications, which is normally in the range of 10^5 to 10^6 cm^{-2}. In 2007, It was demonstrated that the impact of TDs on Si-Ge interdiffusion is negligible for a higher Ge fraction range when the threading dislocation density (TDD) is around 10^7 cm^{-2} [10]. When the dislocation density is up to 10^{10} cm^{-2}, Si-Ge interdiffusivity can be enhanced by two orders of magnitude when x_{Ge} < 0.20, reported by Gavelle *et al* [21].

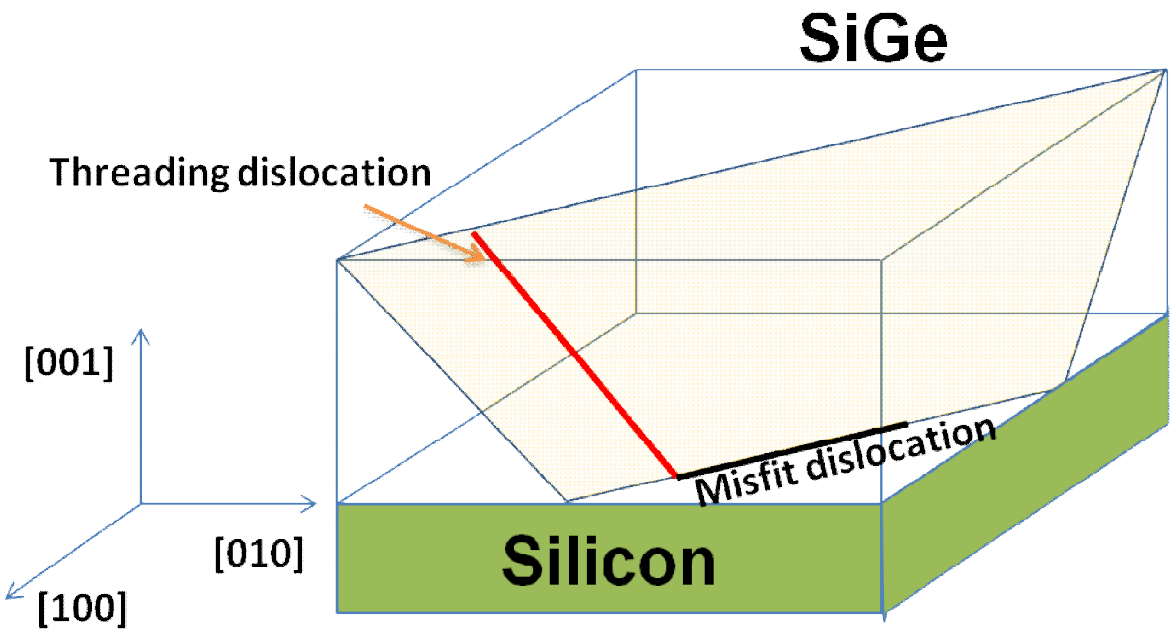

Figure 2.8 A schematic structure of a SiGe epitaxial thin film (a SiGe film is grown in (100) substrate) and a MD and TD in it.

2.5.3 Concentration dependent interdiffusivity and the effect of dislocation-assisted interdiffusion

Figure 2.9 summarizes the literature available Si-Ge interdiffusivities for relaxed SiGe measured as a function of Ge fraction. The data from Gavelle *et al*. are from highly defected Ge/Si structures with a dislocation density as high as 10^{10} cm^{-2} [21], while the dislocation densities from other studies are around 10^{4}~10^{6} cm^{-2} [10, 16-20]. For the data measured from low dislocation density materials, it is clear that Si-Ge interdiffusivity has a strong concentration dependence. From the Si end to the Ge end, the interdiffusivity increases by five orders of magnitude. In comparison, the interdiffusivity measured from high dislocation density materials increases by less than three orders of magnitude.

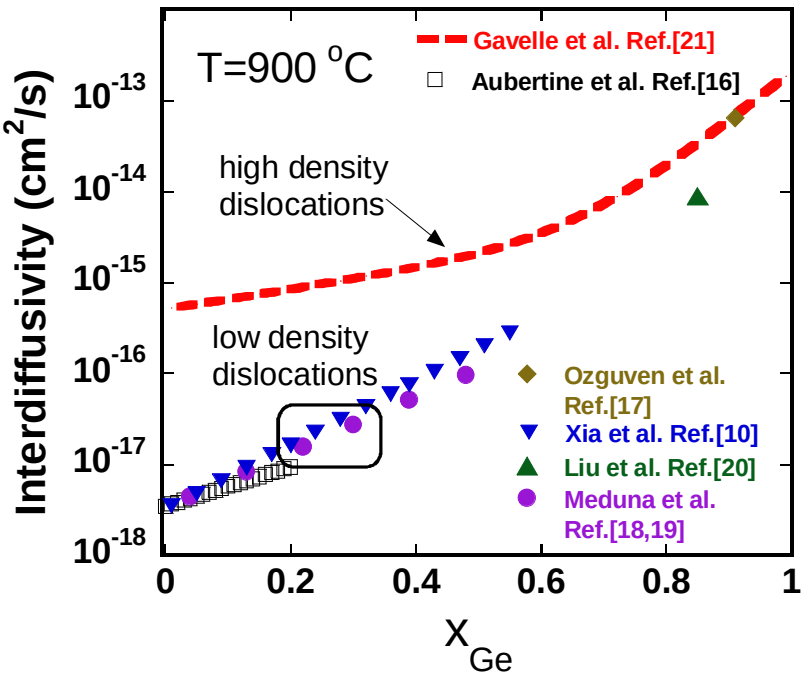

Figure 2.9 Summary of Si-Ge interdiffusivities for relaxed SiGe measured in literature as a function of Ge fraction at 900 °C.

When interdiffusivity has a strong concentration dependence, it can happen that an initially sloped interface profile becomes steeper or more box-like [60]. It may seem counter-intuitive, as normally diffusion makes the concentration profiles wider and flatter. However, if the diffusivity is strongly concentration dependent, most of the diffusion happens in the high concentration region, with much less diffusion in the low concentration regime.

Figure 2.10 illustrates this effect by comparison between the diffused profiles with and without strong concentration dependent diffusivities. Starting with a same triangle-shaped profile of the species A, Figure 2.10(a) shows the final profiles of A after a 40 mins-diffusion at 800 °C and one at 840 °C with a constant diffusivity. Figure 2.10(b) shows those with a strong concentration dependent diffusivity, where the diffusivity at the peak of species A's profile is two orders of magnitude larger than that at the bottom.

The final profiles in Figure 2.10(a) show a type of Gaussian-distribution diffusion, and the two edges of the triangle shaped profile become flatter. Compared with the profiles in Figure 2.10(a), the final profiles with a strong concentration dependent diffusivity in Figure 2.10(b) have steeper edges than those of the initial profile. For SiGe system, the interdiffusivity has a strong concentration dependence, so the interdiffusion profiles will be like the case in Figure 2.10(b). This is especially true for SiGe systems with a low dislocation density. With a high dislocation density, the dislocation-assisted diffusion becomes significant, which increases the interdiffusivity at low Ge concentrations as shown in Figure 2.9. This makes the overall interdiffusivity less concentration dependent, and the profiles after anneals less box-like. More details will be discussed in Section 6.5.

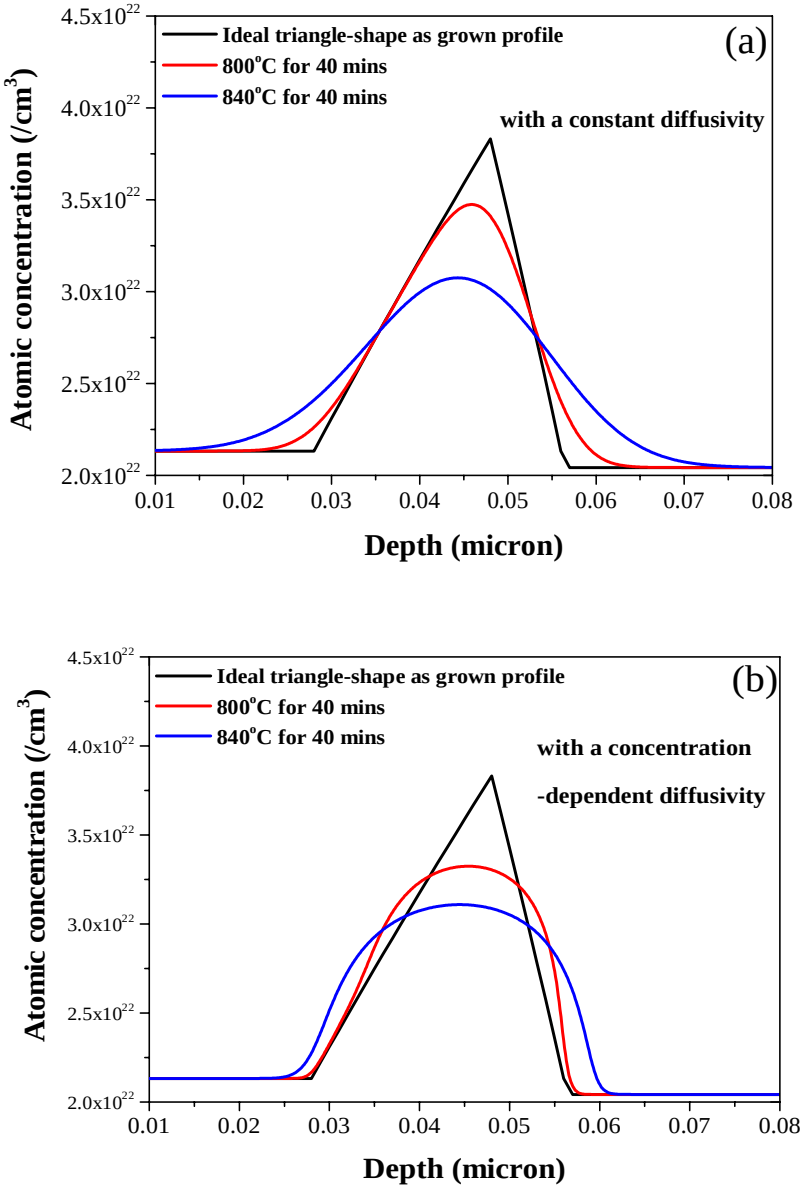

Figure 2.10 (a) the diffusion profiles of the species A after a 40 mins-diffusion at 800 °C and 840 °C with a constant diffusivity, D=500*exp(-4.1/*kT*); (b) the diffusion profiles of the species A after a 40 mins-diffusion at 800 °C and 840 °C with a concentration dependent diffusivity, D=500*exp[-(4.76-1.44x_A)/*kT*], x_A denotes A molar fraction in the matrix.

Chapter 3 Practical Aspects of Experiments

As discussed in Chapter 2, SiGe alloys can be considered as a regular solution. One may ask why the interdiffusion behaviour of Si-Ge is still a topic of active research today. This is a valid question to ask, and there are quite a few reasons to this question.

In terms of the needs and significance, 1) Si had been so successful in the past century, and SiGe with low Ge fractions (≤ 20%) has been used mostly in bipolar junction transistors, where Si-Ge interdiffusion is relatively slow and not significant; 2) starting from this century, SiGe has been widely used in CMOS, and the Ge fraction has been increasing to about 50%, and under compressive stress, both of which increase interdiffusivity exponentially. Meanwhile, the scaling of the devices has made the device dimensions so small that the diffusion length is getting comparable to the device dimensions.

The interdiffusion studied here is on the atomic scale, which requires great material quality, a careful experiment design, high accuracy in thermal anneals and characterization tools: 1) this study requires the high quality epitaxial growth of SiGe film stacks in a wide Ge fraction range, and only a few university labs in North America have that capability; 2) stress status needs to be closely monitored such that interdiffusion can happen with full coherent strains. This in turn requires a careful design of the film stacks and thermal budgets; 3) like any other diffusion study, temperature calibration is crucial to the accuracy of data and modeling. A temperature accuracy of a few degrees is required. The advanced anneal techniques, such as different types of rapid thermal anneals (RTAs), work by the thermal absorption of intense light emission. RTA tools are very sensitive to the cleanness inside chambers, and are much harder to calibrate for multi-user cleanrooms, where various materials are used. In this work, we collaborated with Matson Technology, who is a major RTA tool manufacturer with the R&D department in Canada before the fall of 2012; 4) Accurate measurements of the atomic scale Si and Ge profiles are normally

done by SIMS. Although SIMS tools are available in multiple universities in Canada and US, we have not found any SIMS tool in a university that is calibrated enough to cover the full Ge fraction ranges for the atomic scale depth profiling. For this work, SIMS measurements are performed by Evans Analytical Group, which has been proven to be the best in repeatability and accuracy.

Overall, the Si-Ge interdiffusion study on the atomic scale highly depends on material quality, experiment design, anneal and characterization tool accuracy. In the following sessions, we will discuss the practical aspects of this work in details.

3.1 Sample structure design and sample growth

The sample structure design is critical to diffusivity measurements in semiconductors. The "diffusion" discussed in this work is the lattice diffusion through point defects (interstitials and vacancies). For semiconductor devices, especially MOSFETs in logic circuits, other extended defects such as dislocations should be minimized because those defects can influence diffusion and degrade device performance. In this thesis, after a unified interdiffusivity model without strain is built theoretically, the study focuses on the Si-Ge interdiffusion under strain through point defects. The strained samples used in this work mimic the device structure of a dual channel strained SiGe MOSFET grown on virtual substrates. In order to avoid mismatch strain relaxation during thermal anneals, the issue of the critical thickness for epitaxial layer growth should be considered in the first place.

3.1.1 Critical thickness of SiGe epitaxial structures

Due to the lattice mismatch (4.18%) between Si and Ge, there are commonly strain fields in SiGe heterostructures. If the strain energy is too high in these epitaxial layers, plastic strain relaxation will happen by the nucleation and movement of dislocations during growth or post-

growth anneals. For epitaxial thin films, the pioneering work of Merwe [61] and Matthews and Blakeslee [62] proved that under thermal equilibrium, the epitaxial film grows pseudomorphically up to a limited thickness, namely the critical thickness, which depends on the mismatch level. Above this critical thickness, the epitaxial layer is metastable and strain relaxation occurs by the introduction of misfit dislocation segments lying at the SiGe/SiGe interfaces. Based on a simplified Matthews-Blakeslee model [63], the equilibrium critical thickness t_{cm} can be written as

$$\left(\frac{t_{cm}}{b}\right) f = 5.78\times10^{-2} \ln\left(\frac{4t_{cm}}{b}\right) \qquad 3.1$$

where t_{cm} is the equilibrium critical thickness, and b is the Burger's vector length (0.38 nm). f is the lattice mismatch, $f = \frac{a_{Si_{1-x}Ge_x} - a_{Si}}{a_{Si}} = 0.0418x_{Ge}$ for $Si_{1-x}Ge_x$ grown in Si.

From Equation 3.1, for a $Si_{0.6}Ge_{0.4}$/Si heterostructure, the critical thickness is about 5 nm. Later, with the growth technique of Molecular Beam Epitaxy (MBE), Bean and his coworkers demonstrated that at rather low growth temperatures (550°C), the experimentally obtained values of the critical thickness are far larger than the equilibrium ones [64]. It was explained that at lower temperatures the onset of plastic deformation shifts to a higher thickness because of kinetic limitations to dislocation nucleation and dislocation movements. Based on the fittings of experimental data, an upper boundary of the metastable regime was obtained as [63]

$$t_{cp} f^2 = 2.34\times10^{-3} \ln\left(\frac{t_{cp}}{b}\right) \qquad 3.2$$

The equilibrium and metastable boundaries divide the thickness-x_{Ge} region into three regimes: stable, metastable and relaxed with defects, as shown in Figure 3.1.

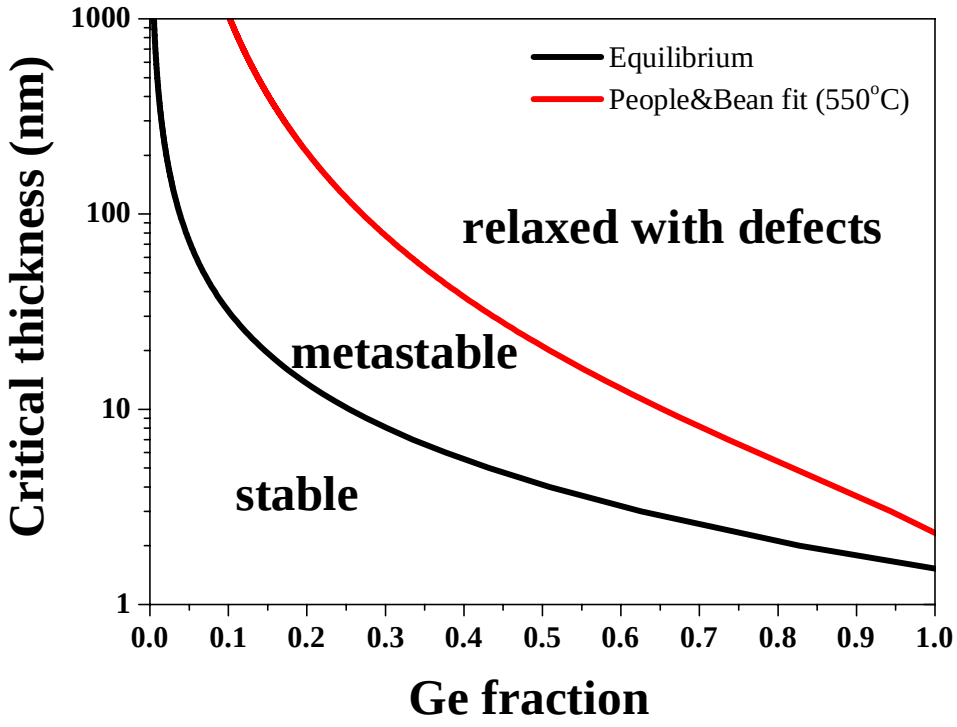

Figure 3.1 Critical thickness vs Ge fraction x_{Ge}. Two boundaries divide the critical thickness map into three regimes: Stable, Metastable and Relaxation with defects. The solid line is the equilibrium line and the dash line is the metastable upper limit done by People and Bean based on energy balance [64].

3.1.2 Biaxial strain in SiGe heterostructures

As discussed in Chapter 1, for SiGe based devices, strain has been employed to enhance carrier mobilities in MOSFETs or to engineer the band structures of HBTs and quantum wells. Strain can also influence Si-Ge interdiffusion [10, 16]. In heterostructure semiconductor devices, between the neighbouring layers, biaxial strain due to lattice mismatch usually exists. In Figure 3.2(a), biaxial strain exists between two SiGe layers with different Ge fractions. When $y > x$, the top $Si_{1-y}Ge_y$ layer is compressively strained, while the bottom $Si_{1-x}Ge_x$ layer tensilely strained. If the bottom $Si_{1-x}Ge_x$ layer is far thicker than the top $Si_{1-y}Ge_y$ one, the tensile strain in the bottom $Si_{1-x}Ge_x$ layer is small and is normally ignored. Figure 3.2(b) shows a top-down view of

the top $Si_{1-y}Ge_y$ layer, which is under the biaxial compressive strain. Conventionally, the biaxial compressive strain can be expressed as $\varepsilon = -\eta(y - x)$, where η is the linear expansion per unit composition change. At room temperature, η=0.0418.

On the other hand, due to the different thermal expansion coefficients of Si and Ge, thermal stresses during thermal anneals may influence the biaxial compressive strain in SiGe heterostructures. In addition, the thermal expansion coefficients of Si and Ge have a temperature dependence themselves. Based on the experimental measurements and mathematical fittings [65, 66], the linear thermal expansion coefficients of Si and Ge can be expressed as

$$\alpha_{Si}(T) = 3.725 \times (1 - \exp[-5.88 \times 10^{-3}(T - 124)]) + 5.548 \times 10^{-4}T \ (10^{-6}/K) \quad 3.3$$

$$\alpha_{Ge}(T) = 5.231 \times (1 - \exp[-9.60 \times 10^{-3}(T - 14.9)]) + 3.300 \times 10^{-3}T \ (10^{-6}/K) \quad 3.4$$

Then the lattice parameter $a(T)$ for Si and Ge at temperature T is calculated by the integration equation:

$$a(T) = a_0(300K) \times \left[1 + \int_{300}^{T} \alpha(T')dT'\right] \quad 3.5$$

Combining Equation 3.3~3.5, at temperature T, $\eta(T)$ can be estimated by

$$\eta(T) = \frac{a_{Ge}(T) - a_{Si}(T)}{a_{Si}(T)} \quad 3.6$$

For the temperature range (720 °C~880 °C) used in the studies on the impact of the compressive strain in Chapter 5 and 6, the change of η caused by thermal stress, $\frac{\eta(T)-\eta_0}{\eta_0}$ is around 5%~7% (η_0 is the value at room temperature). Therefore, in this study, the impact of thermal stress is ignored as in previous studies on the strain's impact on Si-Ge interdiffusion [10, 15, 16, 20, 67, 68]

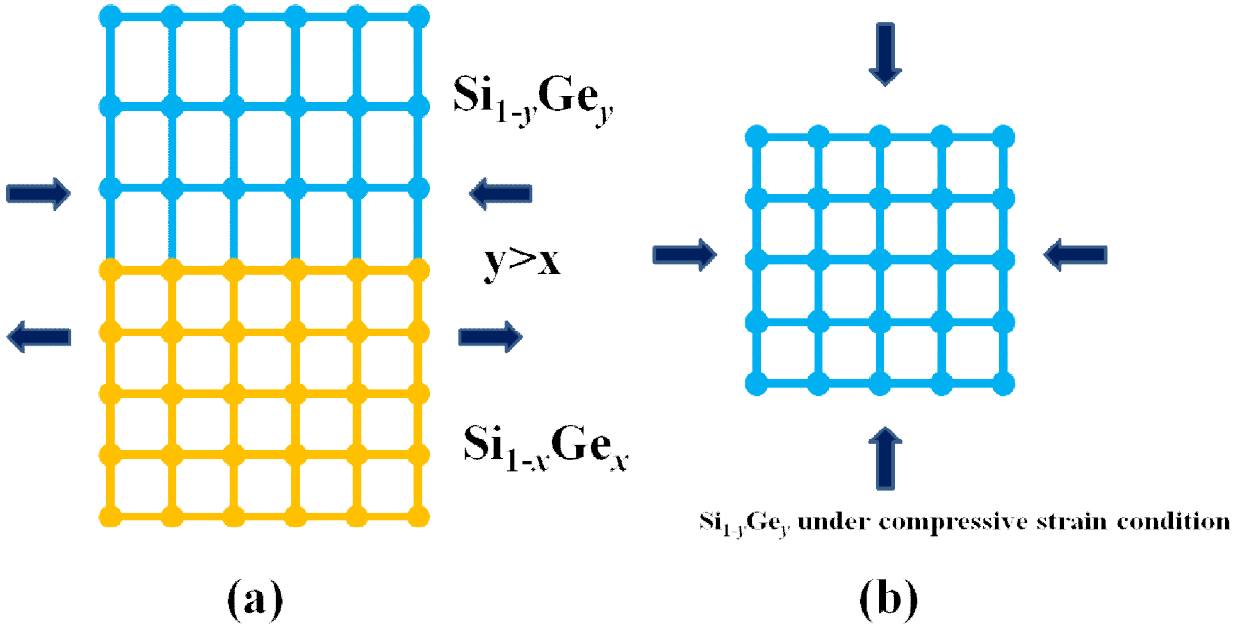

Figure 3.2 (a) Schematic graph of a SiGe heterostructure with different Ge fractions ($y > x$); (b) top-view of the top $Si_{1-y}Ge_y$ layer under biaxial compressive strain.

3.1.3 Sample structure and growth

Two types of diffusion structures are used in this work. The first structure type is called "step structure" with a $strained\ Si/relaxed\ Si_{1-x}Ge_x$ heterostructure. The wafers were originally designed for Xia et al's work in [10], and the remaining wafer pieces are used in the study discussed in Chapter 4. The details of the step structure were described in Xia's thesis [10]. The other structure has a $Si_{1-x}Ge_x/Si_{1-y}Ge_y/Si_{1-x}Ge_x$ ($y > x$) film stack as the key interdiffusion structure in this work, and is employed for the interdiffusion study discussed in Chapter 5 and 6. The design and growth details of the latter structure are shown in this section.

1) **Pseudomorphic structure design for the study of strain impact on Si-Ge interdiffusion**

A multi-layered pseudomorphic structure is used in this study: $Si_{1-x}Ge_x/Si_{1-y}Ge_y/Si_{1-x}Ge_x$ ($y > x$), as shown in Figure 3.3. From our knowledge of literature, the best definition of "pseudomorphic" was given by E. Kasper and S. Heim [69], where it was said "the film structure is pseudomorphic with the in-plane lattice constant of the film fitted to the substrate by a biaxial film stress which results in a tetragonal distortion of the cubic lattice cell of the film. Pseudomorphic films are also called strained films or coherent films". Pseudomorphic SiGe films were illustrated in Figure 3.2.

Strictly, only the stable regime in Figure 3.1 can be described as "pseudomorphic". The thickness of the strained films should not exceed the Matthews-Blakeslee limit. So, the key constraints of a structure design are the critical thickness, growth temperature and the anneal thermal budget. Strained thin films above the critical thickness are metastable and would be relaxed by misfit dislocations during growth or post anneals if the thermal budget is high enough [70, 71]. Therefore, in the first place the thickness of the strained layers should not exceed the Matthews-Blakeslee limit. The second constraint is the thermal budget during epitaxial growth. The growth temperature and time are required as low as possible such that the SiGe intermixing at the interfaces in the as-grown structures can be minimized.

On the other hand, the pipe effect of threading dislocations in epitaxial layers should be considered. If there is a high density of threading dislocations (TD), it would complicate the analysis of the interdiffusion. To suppress the TDD and its impact on the interdiffusion, three special considerations are included in the sample structure:

a) A 5 micron-thick graded SiGe buffer layer was grown as the virtual substrate. The TDD at the surface of the graded SiGe layer can be reduced greatly to the order of magnitude,

10^7/cm^2. In Ref. [72], with a 1.5 micron thick SiGe layer graded linearly from 5 to 30% and a 0.25 micron-thick $Si_{0.7}Ge_{0.3}$ cap, the TDD at the surface was successfully reduced to 10^7/cm^2.

b) A 1 micron-thick $Si_{1-x}Ge_x$ layer (labeled as bottom $Si_{1-x}Ge_x$ in Figure 3.3) was grown on top of the thick graded SiGe buffer layer to separate the region of interest from the defected graded buffer layer. The growth temperature of the bottom $Si_{1-x}Ge_x$ layer is as high as 900 °C to further reduce the TDD by dislocation glide. The TDD can be reduced to the order of magnitude, 10^5/cm^2 [73].

c) The thickness of the compressively strained $Si_{1-y}Ge_y$ layer does not exceed the Matthews-Blakeslee limit to make sure the layer is pseudomorphically grown. An exception is sample S4585 (see in Table 3.1), which is designed to fall into the metastable regime to investigate interdiffusion behaviours under partial strain.

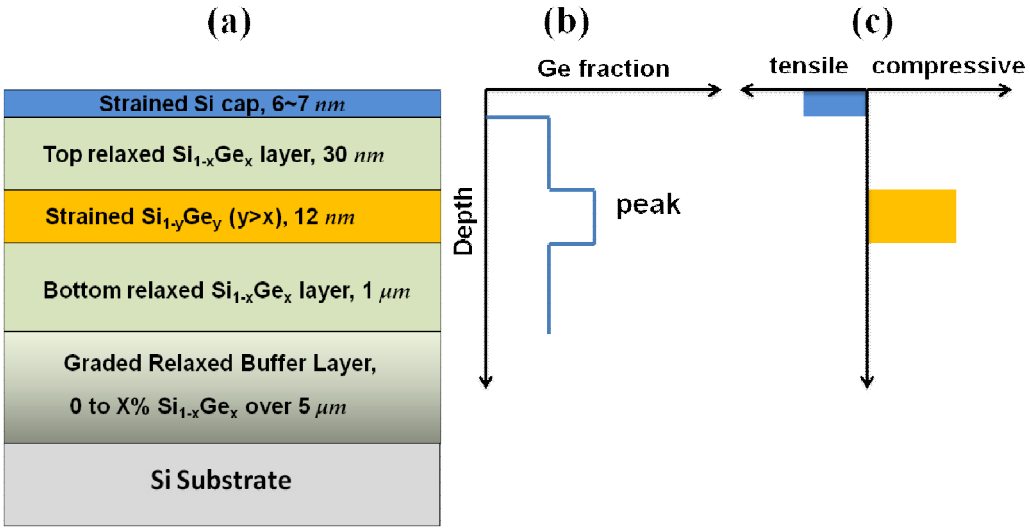

Figure 3.3 (a) Schematic diagram of the tri-layered SiGe stack with a thin Si film on top as the protection cap where $y > x$. The middle $Si_{1-y}Ge_y$ layer is compressively strained while the neighbouring layers $Si_{1-x}Ge_x$ are relaxed. (b) is the depth profile of the Ge fraction, and (c) is the schematic depth profile of the strain.

2) **Sample growth**

A multi-layered pseudomorphic structure was grown for this study: $Si_{1-x}Ge_x/Si_{1-y}Ge_y/Si_{1-x}Ge_x$ ($y > x$), as is shown in Figure 3.3(a). The $Si_{1-y}Ge_y$ layer is under biaxial compressive strain. Three sets of (x, y) were designed: (0.40, 0.65), (0.50, 0.75) and (0.45, 0.85), labeled as S4065, S5075 and S4585. S4065 and S5075 were employed for studying the strain impact on Si-Ge interdiffusion where the thickness of the compressive $Si_{1-y}Ge_y$ layer is under the Matthews-Blakeslee equilibrium limit. S4585 was designed for the study of Si-Ge interdiffusion under partial strain.

All the samples were grown on 6 inch (100) Czochralski (CZ) p-type Si wafers in an Applied Materials "Epi Centura" system (reduced pressure chemical vapor deposition) at MIT. A 1 *μm* relaxed $Si_{1-x}Ge_x$ layer was grown on a graded buffer layer at 900 °C, next a thin compressively strained $Si_{1-y}Ge_y$ layer was grown. For y =0.65, the growth temperature was 525°C; for y = 0.75, the growth temperature was 450°C; and for y = 0.85, the growth temperature was 365°C. On top of the compressively strained layer, another relaxed $Si_{1-x}Ge_x$ layer was grown at 525 °C. Finally, a thin silicon cap was grown on top at 600 °C. The nominal thicknesses of the top strained Si, relaxed $Si_{1-x}Ge_x$ and compressive $Si_{1-y}Ge_y$ layers in S4065 and S5075 are 6 nm, 30 nm and 12 nm separately. The sample structure and schematic profile of Ge fraction and the strain distribution are shown in Figure 3.3 (a), (b) and (c).

Table 3.1 Growth conditions for the top four layers in the three structures. T_g and h denote the growth temperature and the thickness respectively.

Sample	Bottom $Si_{1-x}Ge_x$	Strained $Si_{1-y}Ge_y$	Top $Si_{1-x}Ge_x$	Top Si
S4065	x = 0.40 h = 1 μm T_g = 900°C	y = 0.65 h = 12 nm T_g = 525°C	x = 0.40 h = 30 nm T_g = 525°C	h = 6 nm T_g = 600°C
S5075	x = 0.50 h = 1 μm T_g = 900°C	y = 0.75 h = 12 nm T_g = 450°C	x = 0.50 h = 30 nm T_g = 525°C	h = 6 nm T_g = 600°C
S4585	x = 0.45 h = 1 μm T_g = 900°C	y = 0.85 h = 9 nm T_g = 365°C	x = 0.45 h = 30 nm T_g = 525°C	h = 5 nm T_g = 600°C

3.2 Thermal annealing

Thermal anneals are commonly used to accelerate atom movements in various diffusion studies. On the other hand, in the modern manufacturing of semiconductor devices such as metal oxide semiconductor field effect transistors (MOSFETs), anneals with different thermal budgets are necessary in both the front end of line (FEOL) and back end of line (BEOL) processes.

3.2.1 Trend of thermal budgets for MOSFETs

Up to now, the dominant approach to fabricate MOSFETs in the semiconductor industry is through a top-down approach. SiGe heterostructures are often grown in the early stages of SiGe device fabrication. Therefore, they will go through all the thermal budgets of the following

process steps. The main process steps requiring thermal budgets for the sub-45 nm node were summarized by MacKnight *et al* [74], as shown in Figure 3.4. As the characteristic dimension of advanced MOSFETs scales down to nanometer scales, rapid thermal processing (RTP) has emerged as the key anneal technique for satisfying new requirements of low thermal budgets for shallow junctions. A low thermal budget is critical to dopant profile engineering, because the concentration of electrical active dopants should be maximized to reduce contact resistances without inducing excessive diffusion. The trade-off between dopant activation and diffusion can be optimized with RTP innovations, as MacKnight *et al* stated. On the other hand, higher Ge-fraction SiGe alloys have been exploited and employed for channel materials and for strain engineering to enhance mobilities in dual channel MOSFETs [2, 75, 76] and FinFET [77]. Since the melting point of SiGe alloy decreases as Ge fraction increases, lower thermal budgets are required for SiGe (or Ge) than for Si.

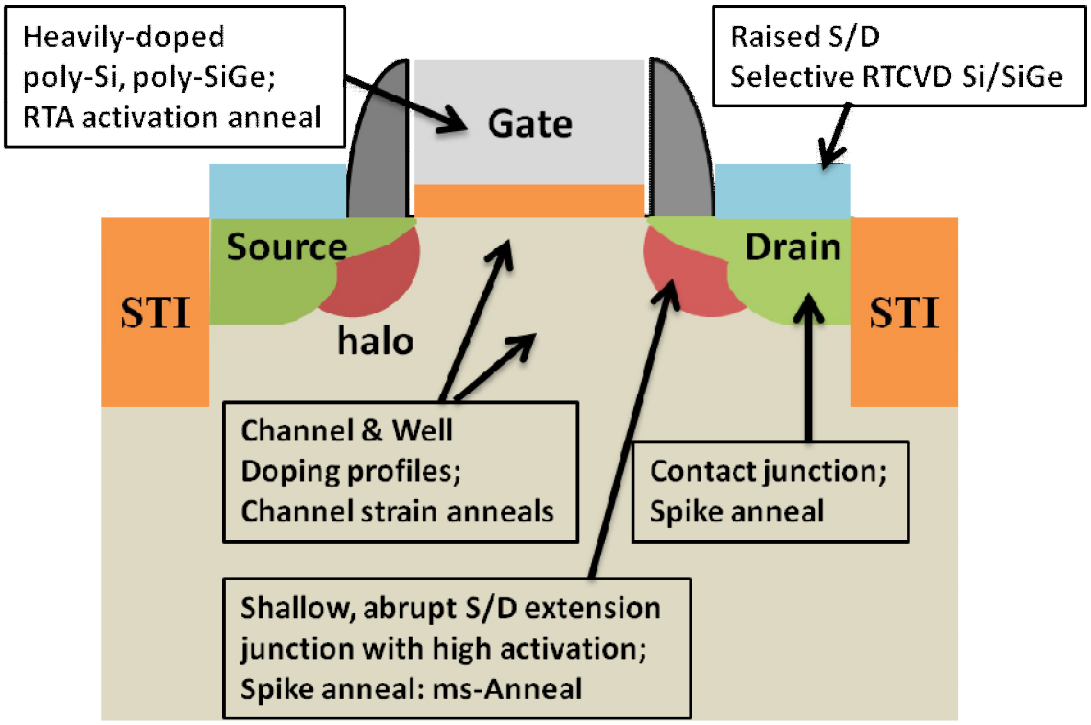

Figure 3.4 Schematic diagram of a typical MOSFET structure and its fabrication processes which require thermal anneals, redrawn from Ref.[74] with permission. Copyright © 2004 IEEE

The reduction of RTP thermal budgets can be achieved by reducing process times or process temperatures or both. The trend of the thermal budgets for typical processes is shown in Figure 3.5. For BEOL processes, the processing temperature is normally below 600 ºC. For FEOL processes, a relatively high temperature is required for implant post-anneals and oxidation etc. with a time range of 10~100 seconds, and the common temperature range is above 800 ºC. More advanced tools of rapid thermal anneals (RTA) have been developed such as soak and spike RTAs to optimize device performance. Moreover, driven by the ultra-shallow junction (USJ) formation, a specific window at a high temperature for a very short anneal time has been developed to optimize the activation and diffusion trade-off for USJs. In flash and laser anneals where the anneal time is in the millisecond scale, the temperature can go as high as 1400 ºC.

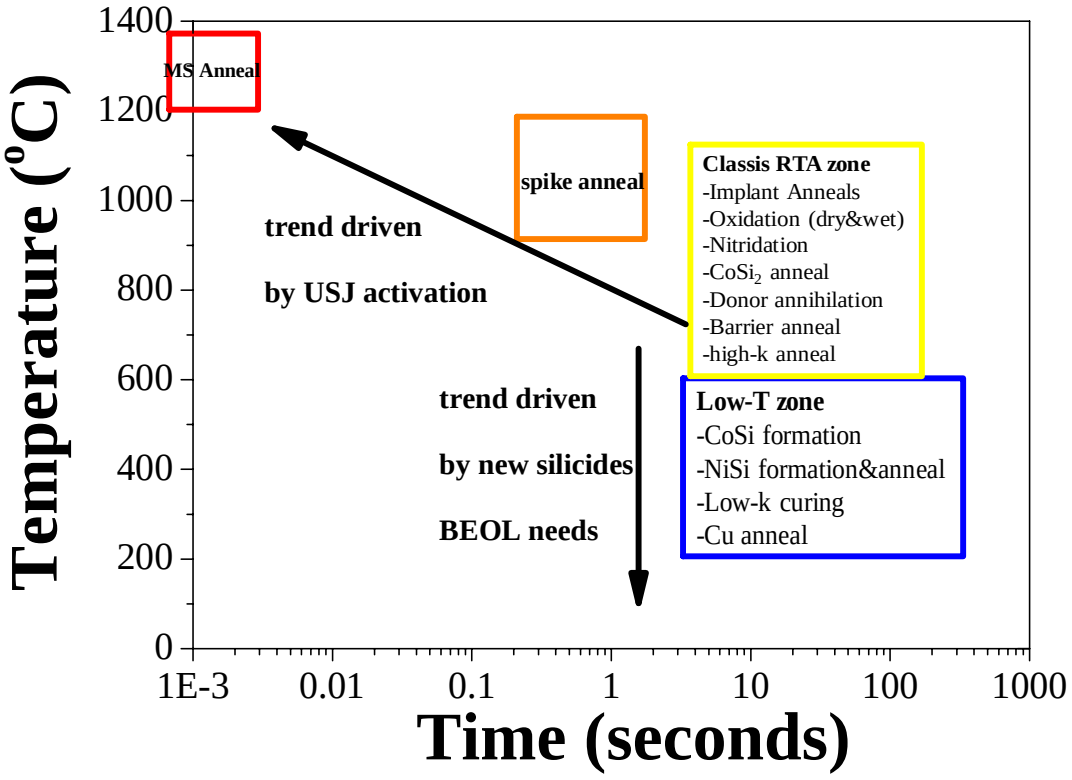

Figure 3.5 The trend and temperature-time window of the thermal budgets for FEOL and BEOL processing, redrawn with permission.[74] **Copyright © 2004 IEEE**

3.2.2 Three types of thermal anneals used in this work: furnace, soak RTA and spike RTA

Furnace anneals are traditionally employed in the semiconductor device manufacturing. It is also widely used in diffusion studies to conduct isothermal anneal experiments. Furnace anneals have long time durations from 30 minutes to several days with slow ramp-up and ramp-down rates (tens of degrees per minute) [10]. As modern semiconductor devices scale down, furnace anneals are no longer the mainstream high-temperature anneal technique for advanced devices, and have been replaced by rapid thermal anneals (RTA) with much faster heating rates and thus smaller thermal budgets. “Soak RTAs” normally have anneal times from a few to tens of seconds at the peak temperature, while “spike RTAs” have minimized dwelling times at the peak temperature [78]. Both of these RTAs are commonly used in the current industry practice. The typical temperature profiles of these three types of thermal anneals are shown in Figure 3.6. Si-Ge interdiffusion studies under RTA conditions are of great significance for the current SiGe based technology, but it was rarely reported before this work.

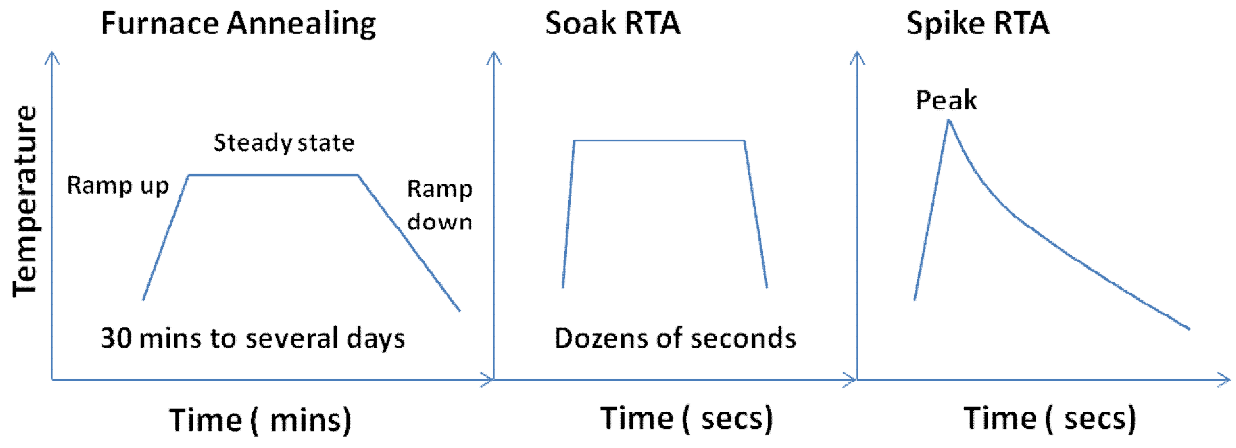

Figure 3.6 The schematic temperature profiles of furnace anneal, soak RTA and spike RTA.

3.2.3 Annealing tool information

As discussed at the beginning of Chapter 3, the temperature calibration is crucial to diffusion studies. A temperature accuracy of a few degrees is required. We spent lots of efforts in finding the right annealing tool across the North American universities and industry for this work. The factor that we use wafer pieces instead of full SiGe wafers makes it much harder as most of Si processing tools handle whole wafers only, only some specific research tools can handle Si wafer pieces. However, we didn't have the luxury to use one full wafer for each anneal condition we have.

At the beginning of this work, we were lucky to have a close-by RTA tool manufacturer, Mattson Technology Canada located in Vancouver to offer the help in this research. They had a R&D RTA tool called K1 tool, which was calibrated using the Si melting point in every run, and was believed to have the temperature accuracy and repeatability within several degrees. After Mattson closed down the Vancouver site, we were not able to find an alternative industry RTA tool, so we turned to furnace anneals. We used MIT's tube furnace for that. To have our own annealing capability, we installed a high temperature stage system TS1200 by Linkam Scientific Instruments. The information of these tools is shown as follows.

1) High Temperature Stage

High Temperature Stage system, TS1200, by Linkam Scientific Instruments, was employed for thermal anneals in this work. The temperature range of TS1200 is from ambient to 1200°C with a maximum heating rate of 150°C/min. The temperature of the sapphire sample plate is measured with a S-type thermocouple and has an accuracy of ±1°C. Water cooling is supplied to keep the stage body cool. Nitrogen gas purge is also equipped, and is used during anneals. In this work, the temperature ramp-up and ramp-down rates are 40 °C/min and 100°C/min respectively.

2) Tube furnace anneal

Tube furnace anneals were done in Exploratory Materials Laboratory (EML) at MIT. Samples were loaded and unloaded in a boat at 400°C. The ramp-up and ramp-down rates were 40~50°C/min and 5°C/min respectively. All the anneals were done in an inert ambient (100% N_2 gas flow).

3) Rapid thermal processing (RTP) tool in Mattson Technology

Soak and spike rapid thermal anneals were carried out on the K1 tool in Mattson Technology. The K1 tool heats the samples up with a high power DC arc lamp. The ramp-up rate can reach 560°C/second. Calibration anneals are done to obtain the reference currents of the arc lamp and the reference radiation intensity at the melting point of Si before the real RTP runs. As it was shown that, the oxygen ambient has a negligible impact on Si-Ge interdiffusion compared with that under an inert atmosphere [79], all the soak and spike RTPs were done in ambient air.

3.3 Secondary ion mass spectrometry

It is critical to determine the Ge concentration precisely for Si-Ge interdiffusion studies. Secondary ion mass spectrometry (SIMS) is the most appropriate analytical technique for this study, because it has the highest detection sensitivity (~subparts per billion) for measuring elemental concentrations, and is able to profile in the depth dimension.

The principle of SIMS is shown in Figure 3.7. A primary ion beam strikes the sample surface, and slowly sputters atoms away, producing monatomic and polyatomic particles of the sample materials. Those secondary ions are then differentiated by a mass analyzer, which produces mass spectra indicating the elemental composition in the sample material. For diffusion studies, the depth profiling of an element of interest is crucial. Depth profiles in SIMS analysis can be

obtained by monitoring the secondary ion count rates of selected elements as a function of time. To convert the time axis into a depth one, SIMS analysts use a profilometer to measure the sputter crater depth simultaneously. A profilometer is a separate instrument that determines the depth position by dragging a stylus across the crater and noting vertical deflections. At last, the depth profiling is obtained. The average sputter rate is the total crater depth divided by the total sputter time. Depth resolution highly depends on the flatness of the bottom craters [80].

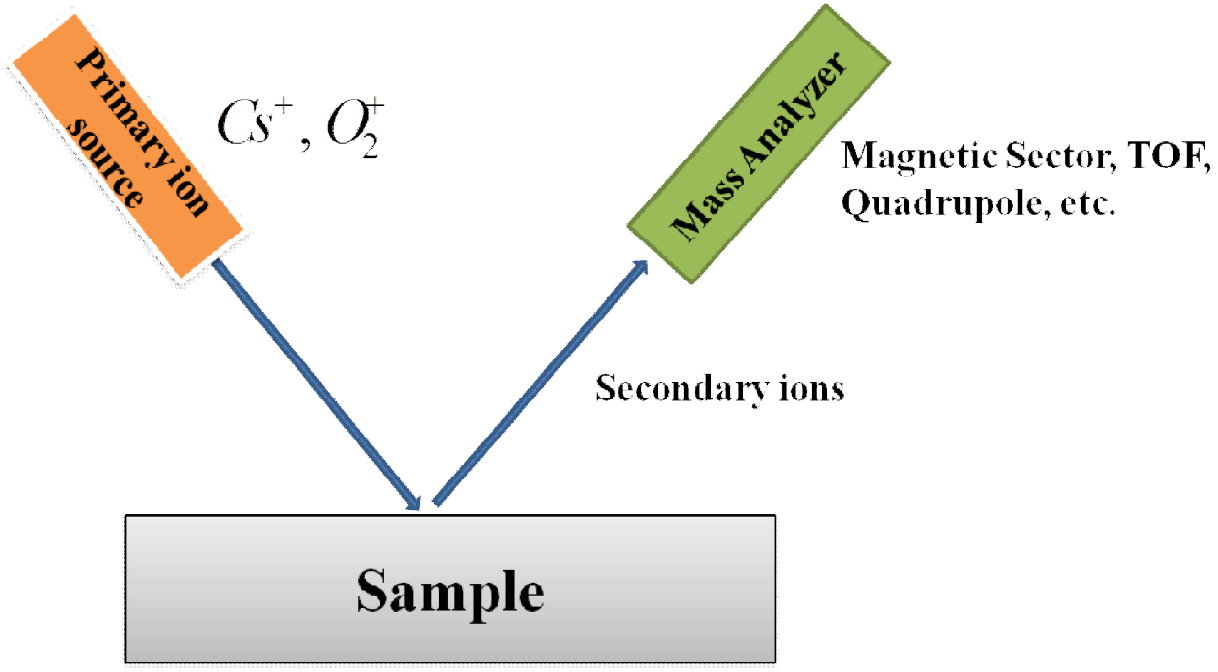

Figure 3.7 Schematic diagram of the principle of SIMS.

For SiGe system, a couple of effects in SIMS analysis influence the accuracy of the final depth profiles. First, there is a knock-on effect caused by the primary beam-induced redistribution of the target atoms and by surface roughening during prolonged sputtering. The implanted primary ions “knock” the near-surface atoms into deeper layers. This effect as well as the atomic mixing induced by a collisional cascade causes a broadening effect to the depth profile [81, 82]. This effect is directly dependent on the energy of the primary ions and their mass ratios with the

different species in the sample. The use of low primary ion beam energy can therefore minimize the “knock-on’ effect and improve the depth resolution.

On the other hand, the secondary ion intensity of a particular species varies by orders of magnitude due to a small variation in composition. This phenomenon is known as the “matrix effect” in SIMS [83-85]. Matrix effects may degrade the reliability of the measured SIMS profiles strongly. Moreover, these effects increase with Ge atomic fraction. However, they were reported to be small for Ge concentrations lower than 30 at.% [84, 85]. Many solutions have been proposed to reduce or suppress those effects, such as the use of an O_2^+ primary ion beam at the normal incidence with an impact energy lower than 3 KeV [86, 87].

The general solution to achieving accurate depth profiles with the lowest knock-on and mixing effects is by a combination of low primary ion beam energy and roughness suppression techniques [83]. Quantification of the depth scale not only requires one point of the sputtering time in the measured profile to be attributed to a certain depth (e.g. by a stylus measuring the depth of the crater after profiling), but generally has to consider non-linear time/depth dependences in the case of a composition-dependent sputtering rate.

In this thesis, all the SIMS measurements were performed by highly qualified scientists at Evans Analytical Group (EAG), which is the industry leader for commercial SIMS analysis, offering the low detection limits along with accurate concentrations and layer structure identification. Our samples were sputtered with 1 KeV Cs^+ primary ion beam obliquely incident on the samples at 60° off the sample surface normal. The secondary ions were analyzed with a quadrupole mass analyzer. The sputter rate was calibrated using a stylus profilometer measurement of the total sputtered crater depth, and corrected on a point-by-point basis with the known sputter rate variation with SiGe compositions. Eventually the measurement uncertainty in Ge atomic fraction and thickness can reach ±1 at.% and 2 nm respectively.

3.4 Raman spectroscopy

The industrial and research developments require metrology solutions for the characterization and subsequent control of several key parameters in Si/SiGe heterostructures such as Ge fraction and the type and magnitude of strain in a SiGe layer. Raman spectroscopy and XRD are the only two techniques which can obtain Ge fraction and strain status simultaneously [88]. There are other techniques to determine Ge fraction such as Rutherford backscattering spectrometry (RBS) [89] and SIMS [10, 79]. However, RBS is not that accurate for measurements of the thin films with a complicated structure, while SIMS is a destructive technique. Raman spectroscopy and XRD have their own advantages: Raman spectroscopy can characterize very thin films near the sample surface and its scan time is faster than XRD; XRD has a larger penetration depth, so it can detect material information from embedded layers in a complicated structure. Combining these two techniques, the Ge fraction and strain information of each layer can be obtained in a multiple layered structure. This section discusses the fundamental knowledge of Raman spectroscopy first.

Raman spectroscopy measures the frequency difference between an incident laser beam and the scattered light that experience Raman scattering by the matrix material. It is widely applied to the investigation of Ge composition and strain in SiGe structures such as SiGe epitaxial layers [90, 91], superlattices [92, 93], quantum wells [94] and quantum dots [95]. The Raman peak positions of the Si-Si (around 500 cm^{-1}), Si-Ge (around 400 cm^{-1}) and Ge-Ge (around 300 cm^{-1}) LO (longitudinal optical phonon) modes are measured. The positions of those characteristic Raman peaks depend on both Ge fraction and strain status, and have been quantized by certain empirical equations [96, 97].

Si has three optical phonon modes: one longitudinal optical (LO) phonon mode and two transverse optical (TO) phonon modes. In the absence of strain, the corresponding three optical

Raman modes of Silicon have the same frequency of ω_{j0} = 520.7 cm^{-1} [97]. Mechanical strain affects the frequencies of the Raman modes, and lifts their degeneracy. The frequencies of the three optical modes in the presence of strain depends on strain, and can be obtained by solving the secular equation [98].

$$\begin{vmatrix} p\varepsilon_{11}+q(\varepsilon_{22}+\varepsilon_{33})-\lambda_1 & 2r\varepsilon_{12} & 2r\varepsilon_{13} \\ 2r\varepsilon_{21} & p\varepsilon_{22}+q(\varepsilon_{11}+\varepsilon_{33})-\lambda_2 & 2r\varepsilon_{23} \\ 2r\varepsilon_{31} & 2r\varepsilon_{32} & p\varepsilon_{33}+q(\varepsilon_{11}+\varepsilon_{22})-\lambda_3 \end{vmatrix} = 0 \qquad 3.7$$

where p, q and r are material constants of the sample, the so-called phonon deformation potentials and ε_{ij} are the strain tensor components. λ_j (j=1, 2, 3) are the eigenvalues of the secular equation.

Then the difference between the Raman frequency ω_j (j=1, 2, 3) of each mode in the presence of strain, and the frequency ω_{j0} without strain can be expressed with the eigenvalues λ_j (j=1, 2, 3):

$$\lambda_j = \omega_j^2 - \omega_{j0}^2 = (\omega_j + \omega_{j0})(\omega_j - \omega_{j0}) \approx 2\omega_{j0}(\omega_j - \omega_{j0}) \ , \qquad 3.8$$

$$\text{then } \Delta\omega_j = \omega_j - \omega_{j0} = \frac{\lambda_j}{2\omega_{j0}} \ . \qquad 3.9$$

The relation between the strain tensor ε_{ij} and the stress tensor σ_{ij} is given by Hooke's law:

$$\begin{bmatrix} \varepsilon_{11} \\ \varepsilon_{22} \\ \varepsilon_{33} \\ 2\varepsilon_{23} \\ 2\varepsilon_{13} \\ 2\varepsilon_{12} \end{bmatrix} = \begin{bmatrix} s_{11} & s_{12} & s_{12} & 0 & 0 & 0 \\ s_{12} & s_{11} & s_{12} & 0 & 0 & 0 \\ s_{12} & s_{12} & s_{11} & 0 & 0 & 0 \\ 0 & 0 & 0 & s_{44} & 0 & 0 \\ 0 & 0 & 0 & 0 & s_{44} & 0 \\ 0 & 0 & 0 & 0 & 0 & s_{44} \end{bmatrix} \begin{bmatrix} \sigma_{11} \\ \sigma_{22} \\ \sigma_{33} \\ \sigma_{23} \\ \sigma_{13} \\ \sigma_{12} \end{bmatrix} \qquad 3.10$$

where s_{11}, s_{12}, and s_{44} are components of the elastic compliance tensor.

Under the (100) Si backscattering configuration, the TO phonon modes are not excited because the component of z polarization of the incident light is reduced to almost zero. Thus only the LO phonon mode is Raman active, Combining the three equations above, for biaxial strain such as in SiGe heterostructures, the Raman shift of the LO phonon mode caused by stress (strain) can be expressed as [97]

$$\Delta\omega_3 = \frac{\lambda_3}{2\omega_{30}} = \frac{1}{2\omega_{30}}\left[ps_{12} + q(s_{11} + s_{12})\right](\sigma_{xx} + \sigma_{yy}) \qquad 3.11$$

For symmetric biaxial strain $\varepsilon_{biaxial}$, $\sigma_{xx} = \sigma_{yy} = (s_{11} + s_{12})\varepsilon_{biaxial}$, then

$$\Delta\omega_3 = \frac{\lambda_3}{2\omega_{30}} = \frac{1}{\omega_{30}}\left[\frac{s_{12}}{s_{11} + s_{12}}\, p + q \right]\varepsilon_{biaxial} = b\varepsilon_{biaxial} \qquad 3.12$$

where b is the so-called phonon strain shift coefficient, which is used for the evaluation of isotropic biaxial strain in semiconductor heterostructures.

For strained SiGe thin films, similar relations between $\boldsymbol{\varepsilon_{biaxial}}$ and Raman shift of LO phonon mode can be obtained theoretically for all the three characteristic peaks (Si-Si and Si-Ge and Ge-Ge). In reality, however, the empirical equations connecting the Raman shifts and Ge fraction and strain are summarized from experimental data. The phonon strain shift coefficient $\boldsymbol{b}$ values reported by many groups are scattered, but have the same order of magnitude. The coefficient $\boldsymbol{b}$ for Si-Si LO phonon is summarized in Table 3.2.

Table 3.2 Phonon strain shift coefficient *b* reported in literature.

Authors (year)	sample	b (cm^{-1})
Anastassakis *et al* (1970)[99]	Si bar	-721
Chandrasekhar *et al* (1978)[100]	Si bar	-696
Anastassakis *et al* (1990)[101]	Si bar	-830
Nakashima *et al* (2006)[102]	Strained Si substrate	-723
Pezzoli *et al* (2008)[91]	SiGe/Si heterostructure	-730
Perova *et al* (2011)[88]	SiGe/Si heterostructure	-830

Most of the studies on strain analysis with Raman spectroscopy focused on strained Si and SiGe with low Ge fraction. The latest comprehensive study on this issue was done by Perova *et al*.[88] They investigated numerous SiGe samples with Ge fraction and the degree of relaxation R varying from 0.1~0.5 and 20%~100% respectively with micro-Raman spectroscopy and XRD. The peak position, peak intensity and the line-width of the phonon modes were accurately determined to estimate the equations describing Si-Si, Si-Ge and Ge-Ge Raman modes from previous studies and to give more accurate ones for the application to thin SiGe layers. The set of equations they obtained are shown as follows:

$$\omega_{Si-Si} = 520 - 70.5x_{Ge} - 830\varepsilon \quad (3.13)$$

$$\omega_{Si-Ge} = 400.5 + 16x_{Ge} - 575\varepsilon \quad (3.14)$$

$$\omega_{Ge-Ge} = 282.5 + 16x_{Ge} - 384\varepsilon \quad (3.15)$$

In this thesis, Raman spectroscopy was employed to obtain the information of Ge fraction and strain in the top two layers of the samples. Raman measurements were performed with a high resolution Raman microscopy system LabRam HR by HORIBA Scientific. The excitation light for

Raman scatting is from a He-Cd laser, which has a wavelength of 442 nm (visible). The probing depth of this wavelength without filters is around 150 nm for SiGe films with medium Ge fraction. The power of the laser beam on the sample surface without filters is around 2 mW, which can be attenuated below 0.2 mW with different filters. In this study, the beam power is attenuated below 1 mW to avoid the shifts caused by laser heating during measurements. Commonly a D0.6 filter is selected to obtain a beam power of 0.5 mW for better Raman signals. Correspondingly, the probing depth is smaller than expected. With a 2400g/mm grating, the spectral resolution is 0.03 cm^{-1} after peak fitting. Finally Raman signals are collected by a thermo-electric cooled CCD (charge coupled device) detector. The schematic configuration of the setup is shown in Figure 3.8.

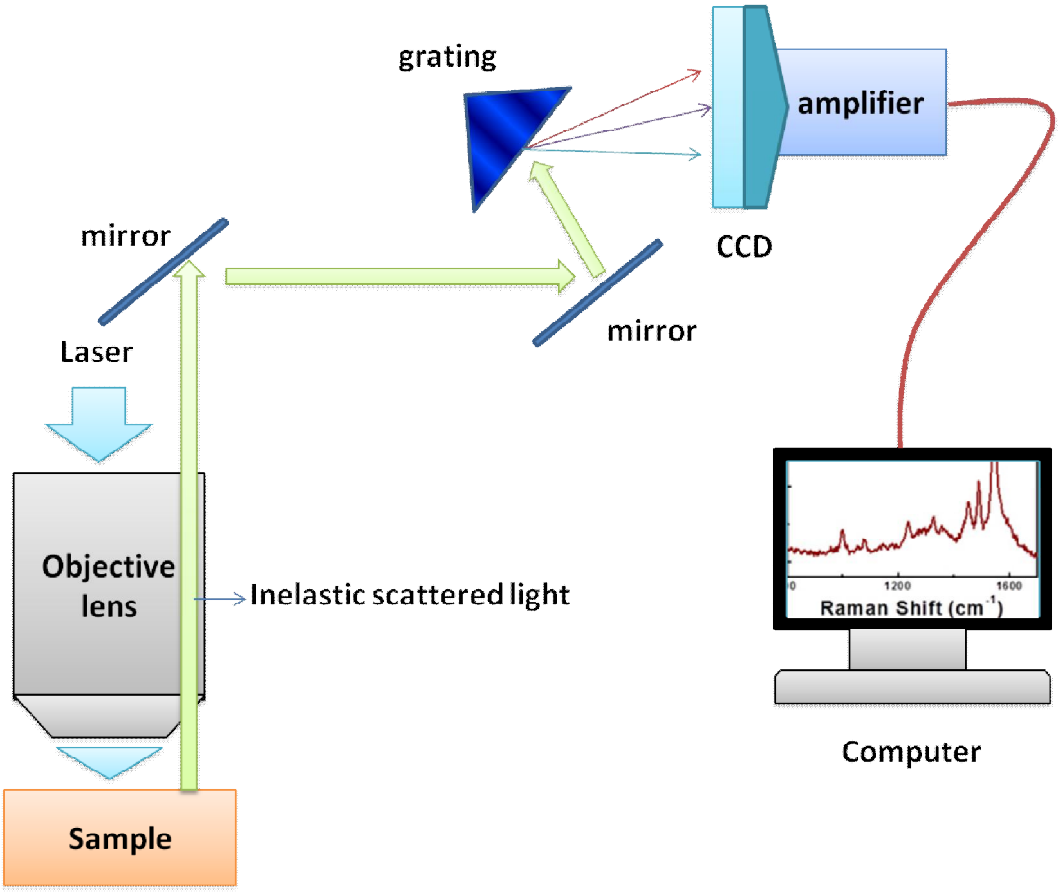

Figure 3.8 Schematic setup for micro-Raman spectroscopy.

3.5 High resolution X-ray diffraction (HRXRD)

HRXRD has been used for decades to investigate semiconductor structures. It has some unique features, including its non-destructive character, a good match of X-ray wavelength to the atomic scale of modern semiconductor devices and the rapid collection of statistically significant data [103]. X-ray diffraction is one of the two techniques to obtain Ge fraction and strain in SiGe layers simultaneously, which is important for the embedded SiGe layers in complicated structures like the samples used in this thesis.

3.5.1 Kinematical theory underlying XRD

The interaction of X-rays with matter happens through the scattering by the electrons of the atomic constituents. Scattering is most easily understood by thinking of a plane wave. When such a plane wave strikes a three dimensional atomic lattice, each scattering point (electron or nuclear particle) acts as a source of spherical waves, whose wavefronts lie on spheres centred on the scattering points [104]. The simplest and most useful description of crystal diffraction is still that obtained by Bragg. Strong diffraction occurs when all the wavelets add up in phase. By considering an entire crystal plane as the scattering entity, rather than each individual electron, it is easily seen that the strong diffraction results happen when

$$n\lambda = 2d\sin\theta \qquad 3.16$$

where n is an integer, λ is the wavelength of the incident wave, d is the spacing between the planes in the atomic lattice and θ is the angle between the incident ray and the scattering planes. A small number of crystal planes give a broad peak, and a large number of planes a narrow peak, converging to a value characteristic of a thick crystal.

The intensities of the diffracted beams depend upon the strength of the scattering that the material inflicts on the radiation. The basis scattering unit of a crystal is its unit cell and we may calculate the scattering at any angle multiplying the scattering strength of one electron or nucleus, then that of an atom, next that of a unit cell and finally that of the total number of unit cells. The amplitude of the wave scattered by a crystal can be expressed as [105]

$$A_{cryst} = A_0 \frac{e^2}{mc^2} \frac{1}{R_0} F(q) \sum_{n_1=0}^{N_1-1} \sum_{n_2=0}^{N_2-1} \sum_{n_3=0}^{N_3-1} \exp(i\vec{q}\bullet(n_1\vec{a}_1 + n_2\vec{a}_2 + n_3\vec{a}_3)) \quad 3.17$$

Where A_0 is the amplitude of the incident wave, e, m, c are the charge of an electron, mass of an electron and the light speed in vacuum, $\frac{e^2}{mc^2}$ is called Thomson scattering length; R_0 is the observation distance. N_1, N_2, N_3 are the numbers of unit cell along the vector directions $\overrightarrow{a_1}$, $\overrightarrow{a_2}$, $\overrightarrow{a_3}$. $\vec{q} = \overrightarrow{k_f} - \overrightarrow{k_\iota}$ is the momentum transfer and in the case of elastic scattering $|\overrightarrow{k_f}| = |\overrightarrow{k_\iota}| = 2\pi/\lambda$, and $F(q) = \sum_{j=1}^{N_c} f_j(q) \exp(i\vec{q}\bullet\vec{r}_j) d^3r$ is the structure factor of the unit cell and N_c is the number of atoms in the unit cell, defined by the vectors $\overrightarrow{a_1}$, $\overrightarrow{a_2}$, $\overrightarrow{a_3}$. $\vec{r_j}$ is the position vector of an atom in the unit cell. All the atoms of the unit cell have their own atomic scattering factors $f_j(q)$.

The structure factor $F(q)$ is a fundamental quantity, which appears in all the expressions for diffracted intensity, penetration depth and rocking curve width. This factor is calculated under some ideal assumptions: the scattered intensity is very small (indicating the loss of intensity due to re-scattering is negligible); R_0 is large compared with the dimensions of any coherently illuminated scattering volume; and scatted waves from different atoms are nearly parallel [104]. The atomic scattering factors $f_j(q)$ are usually calculated in terms of scattering of an individual free electron. This is calculated as if the electron were a classical oscillator since the assumption is that the electron is a free charged particle. It is set into a forced oscillation by the

radiation field of an incident X-ray and then re-radiates in all directions at the same frequency as the incident wave frequency, which is called elastic or Thompson scattering.

3.5.2 Typical diffraction geometry in XRD tools

The schematic figure of the typical diffraction is shown in Figure 3.9. An X-ray beam shines on a sample surface, and the diffracted beam comes out. The angle between the incident X-ray beam and the sample surface is called Omega (ω) while the angle between the incident and diffracted beams called the Bragg angle, 2-theta (2θ). Both ω and 2θ lie in the same plane. Phi (φ) is the angle of rotation of the sample about its surface normal, which is the key parameter to obtain the miscut and tilt angles for epitaxial structures on substrate (defined in Section 3.5.3). Psi (ψ) is the angle of rotation of the plane normal to that containing omega and 2-theta, which is very important during the initial alignment for XRD measurements. From the intensity collected with HRXRD, one can gain valuable information of the epitaxial structures such as the periodicity in artificial superlattices, the quality of the interfacial region, composition, and degree of mosaicity [106, 107].

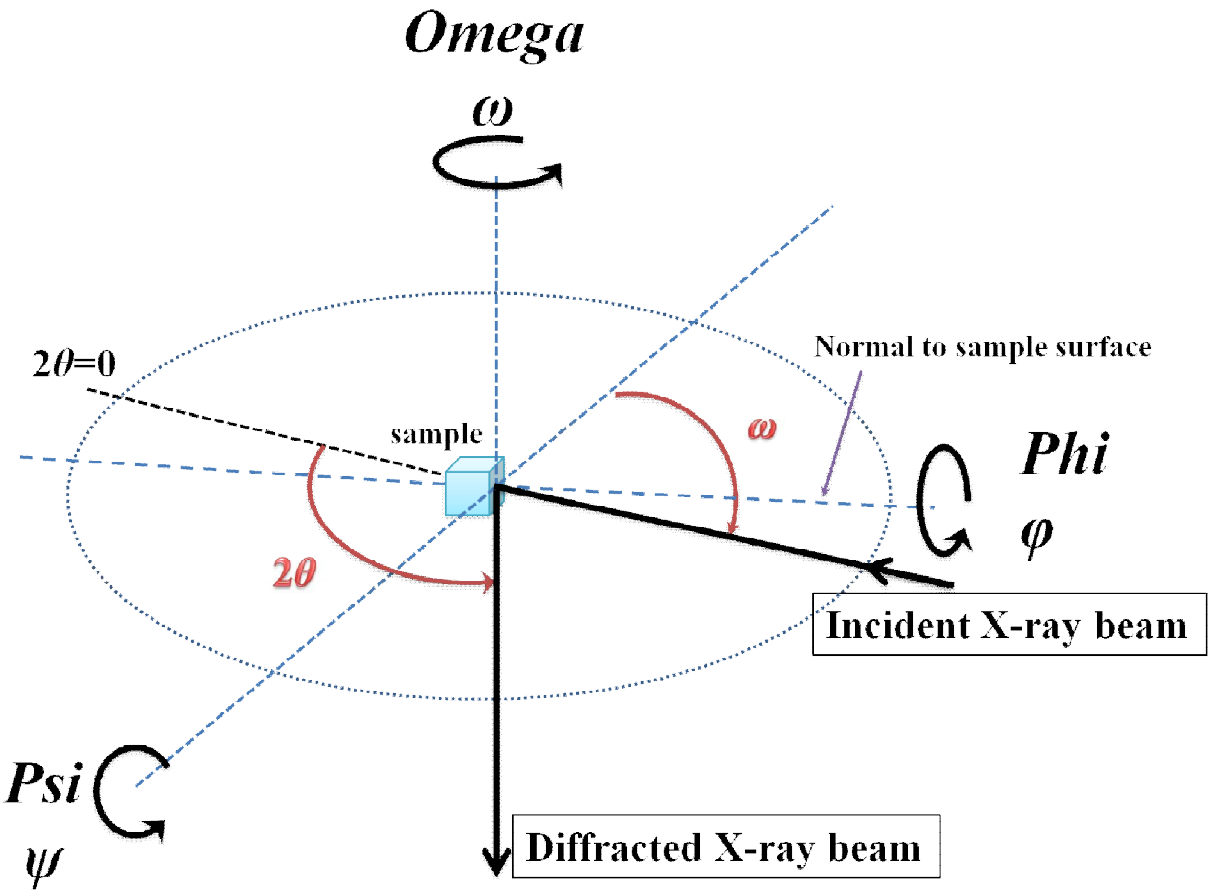

Figure 3.9 Schematic diagram of the typical diffracted geometry of HRXRD tools.

3.5.3 Miscut and tilt

For a (100) wafer, its surface is a (100) plane with [001] direction as the surface normal vector, and wafers are usually sliced, ground and polished after Si ingot growth as precisely as possible. However, in reality, there is a slight miscut (normally is negligible) compared to the target wafer surface orientation [108]. Sometimes, wafers are intentionally miscut, for example by 5° for special purpose like GaAs growth on miscut (100) Ge wafers [109]. If an epitaxial layer is grown on a miscut substrate, a crystallographic tilt is observed between the (100) planes of the epitaxial layer and those of the substrate. This tilt arises because the miscut increases the angle between the Burgers vector and the surface normal for some dislocations while decreasing it for

others. Through dislocations, tilt angles can indirectly impact relaxation mechanisms (dislocation nucleation limited or dislocation glide limited) [110]. In Figure 3.10, the miscut and tilt angles are shown for an epitaxial SiGe layer grown on graded relaxed buffer on a (100) Si substrate. The miscut of the substrate and the tilt of the epitaxial layer with respect to the substrate can easily be measured using diffraction by lattice planes which are nearly parallel to the sample surface. To obtain the exact XRD peak positions of the epitaxial layers of interest, the impact of the tilt and miscut should be taken into account. Based on Mooney *et al*'s work [110, 111], the apparent tilt and miscut angles can be measured by $\omega/2\theta$ scans taken with the same sample at two different positions, one rotated in the plane of the wafer by 180° with respect to the other. The apparent miscut (denoted by symbol M) of the substrate and the tilt (denoted by symbol T) of the layer with respect to the substrate are given by

$$M = \frac{\omega_0 - \omega_{180}}{2} \tag{3.18}$$

$$T = \frac{\Delta\omega_0 - \Delta\omega_{180}}{2} \tag{3.19}$$

where ω_0, ω_{180} are the angular positions of the substrate peak at phi=0° and 180°, and $\Delta\omega_0$, $\Delta\omega_{180}$ are the separation between the substrate peaks and alloy layer peaks.

Then we can obtain the accurate peak positions (denoted by symbol P) without tilt impact as

$$P = \frac{\Delta\omega_0 + \Delta\omega_{180}}{2} \tag{3.20}$$

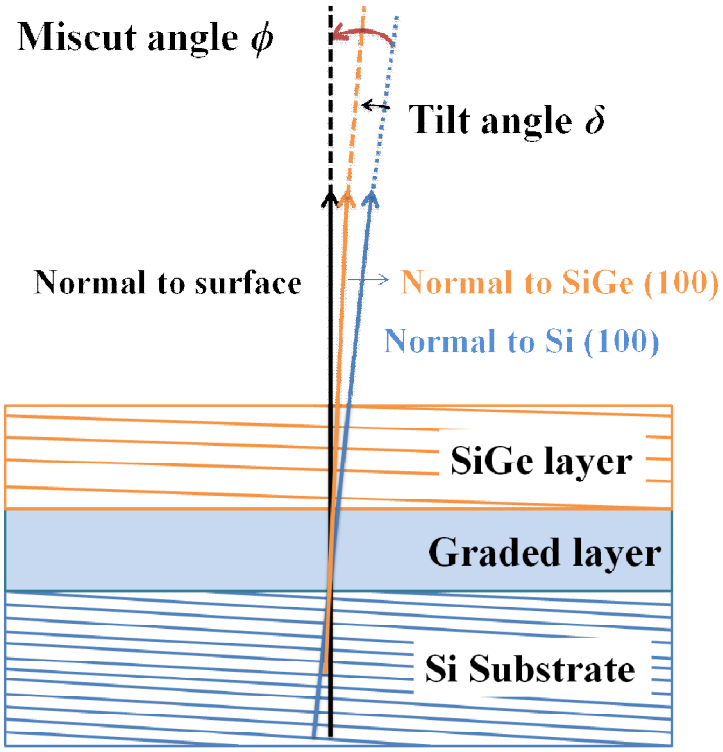

Figure 3.10 Schematic diagram of miscut and tilt angles for an epitaxial SiGe layer grown on graded relaxed buffer on (100) Si substrate.

3.5.4 Reciprocal space mapping

Reciprocal space is a significant concept in solid state physics, and is very useful in the interpretation of the XRD diffraction theory. For the lattice axes $(\vec{a_1}, \vec{a_2}, \vec{a_2})$ of the unit cell of the real lattice, the reciprocal lattice axes $(\vec{b_1}, \vec{b_2}, \vec{b_2})$ can be defined as [112]

$$\vec{b}_1 = \frac{\vec{a}_2 \times \vec{a}_3}{\vec{a}_1 \bullet (\vec{a}_2 \times \vec{a}_3)}; \ \vec{b}_2 = \frac{\vec{a}_3 \times \vec{a}_1}{\vec{a}_2 \bullet (\vec{a}_3 \times \vec{a}_1)}; \ \vec{b}_3 = \frac{\vec{a}_1 \times \vec{a}_2}{\vec{a}_3 \bullet (\vec{a}_1 \times \vec{a}_2)} \qquad 3.21$$

Sometimes, there is a 2π scale factor for mathematical convenience in treatments of quantum physics. In general, in crystallography, this factor is not used [104]. From the equations above, we can see the direction of the vector is normal to the corresponding planes in real space, and the magnitude of the vector is the inverse of the inter-planar spacing in the real space. For cubic

crystal lattice, the reciprocal lattice axes are parallel to the [100], [010] and [001] directions, and Equation 3.21 can be simplified as

$$b_1 = \frac{1}{a_1};\ b_2 = \frac{1}{a_2};\ b_3 = \frac{1}{a_3} \qquad 3.22$$

In the reciprocal lattice, each point represents a vector which, in turn, represents a set of Bragg planes in the real lattice space. Combined with the Ewald sphere construction in the reciprocal space [113], Bragg's law can be presented vividly, shown in Figure 3.11. Under the assumption of elastic scattering, it is always true that the magnitude of K_i and K_f are both $1/\lambda$. A sphere of radius $1/\lambda$ can therefore define all possible incident and scattered beam vectors. The incident beam enters the sphere along a radius. Strong diffraction will occur when a reciprocal lattice point lies on the circumference of the circle. The wave vectors of the incident wave and diffracted wave meet the equation:

$$\vec{K}_f - \vec{K}_i = \vec{Q} \qquad 3.23$$

where Q is defined as the scattering vector.

And this equation is equivalent to the Bragg's law:

$sin\theta = \frac{|Q|}{2/\lambda}$ where $|Q| = 1/d_{hkl}$, then $\lambda = 2d_{hkl}\sin\theta$. 3.24

With Ewald sphere construction in mind, characteristic peaks in the reciprocal space mapping (RSM) can be identified as the corresponding reciprocal lattice points for certain crystal planes. In order to obtain a RSM from epitaxial thin films on Si substrate, an alignment should be done to find the peak from Si substrate in the first place. Then, a couple of rocking curves need to be done around the Si peak to locate the peak positions from the epitaxial thin films and decide the Omega ranges for RSM. After that, the mapping is done by transforming a series of rocking

curves over a range of angles for Omega. By combining these scan curves and recording the scattered intensity as a function of Omega and 2-Theta, a two dimensional map of the spanned reciprocal space can be produced. The transformation from the recorded angles (Omega and 2-Theta) to $Q_{\perp}$ and $Q_{\parallel}$ can be done using the following simple transformation equations [114]:

$$Q_{\perp} = R[\cos\omega - \cos(2\theta - \omega)]$$
$$Q_{\parallel} = R[\sin\omega - \sin(2\theta - \omega)] \qquad 3.25$$

where R is the radius of the Ewald sphere, $1/\lambda$.

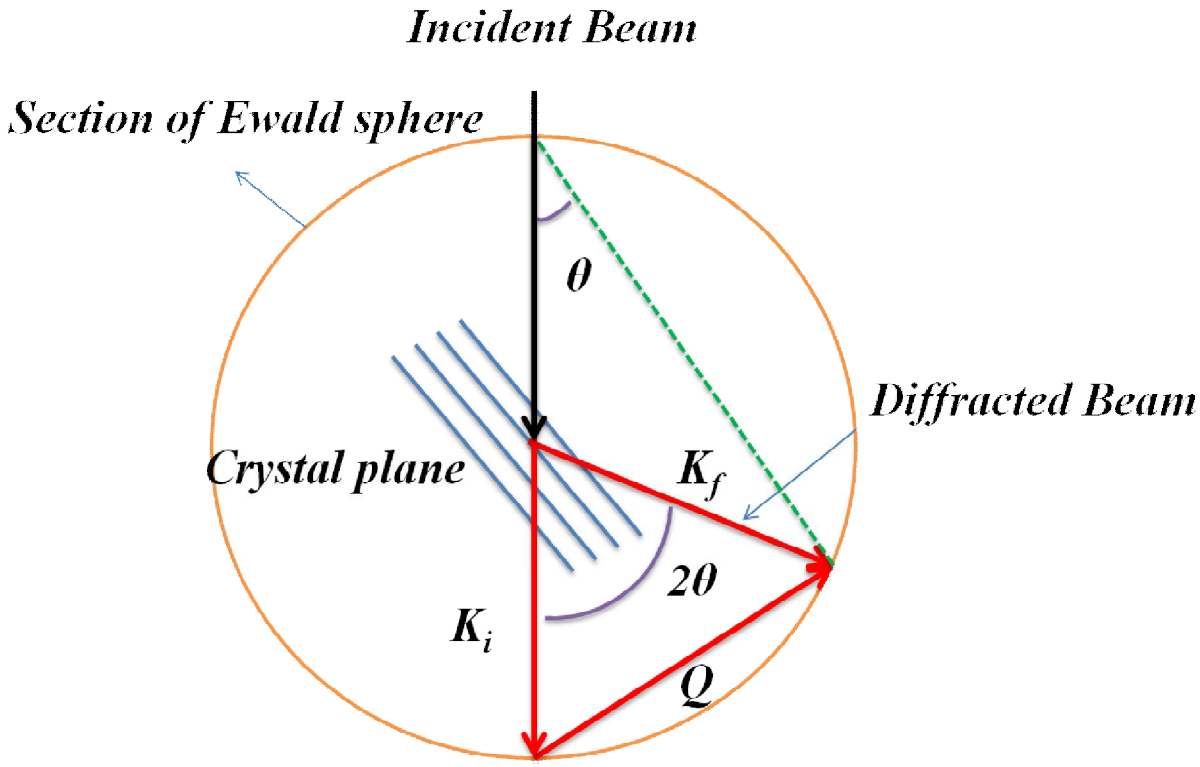

Figure 3.11 Two dimensional section of Ewald sphere construction.

From the peak patterns in asymmetric RSM from epitaxial structures on a substrate, the strain status of the epitaxial layer is readily differentiated. Some typical patterns of RSM from epitaxial structures like Ge on Si substrate are shown in Figure 3.12. If the epitaxial layer is coherent with

the substrate, the peaks from the epitaxial layer and the substrate are lined-up in the asymmetric RSM, called the coherent line as the dash line shown in Figure 3.12. If the epitaxial layer is fully relaxed, the two peaks and the origin point fall in the same line (as the green dot line shows). If there is partial strain relaxation, the peak from the epitaxial layer is in between the coherent line and the full relaxation line. However, tilt will impact the strain calculation [115, 116]. In order to rule out the impact of tilt, a symmetric RSM should be done. The combination of symmetric and asymmetric RSMs can also allow a quantitative strain analysis, but sometimes, the epitaxial layers are too thin to obtain noticeable peaks in RSM.

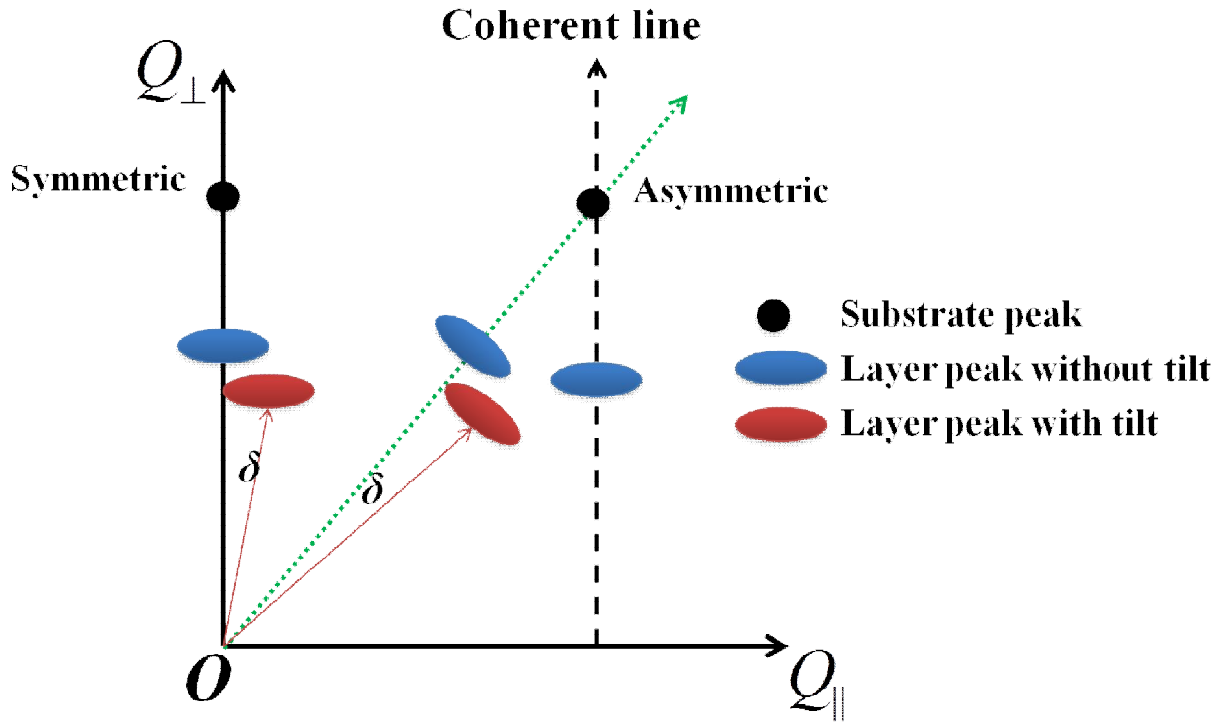

Figure 3.12 Typical patterns of RSM peaks for epitaxial layers on a substrate.

In this work, all XRD measurements were performed using a PANalytical X'Pert PRO MRD with a triple axis configuration in Semiconductor Defect Spectroscopy Laboratory at Simon Fraser University. The X-ray tube was operated at 45 kV and 40 mA in the line focus mode. The $Cu - K\alpha_1$ wavelength (λ = 1.5406 Å) was selected by a hybrid 2 bounce monochromator, giving

a collaminated, monochromatic beam. A proportional detector is used to count the number of photons at a certain detector angle (2-Theta). The detector has a 99% linearity range of 0~500, 000 counts/second and an 84 % efficiency for Cu radiation. The analyzer was activated when doing reciprocal space mappings.

3.6 Measurement techniques for threading dislocation density (TDD)

Many characterization techniques have been employed to measure the TDD and study threading dislocation movements in semiconductor thin films such as transmission electron microscopy (TEM) [117, 118], atomic force microscopy (AFM) [119, 120], diffuse XRD [103] and etch pit density (EPD) measurement [121]. Top-view TEM is used to image dislocations directly at a low magnification with a correct contrast condition. However, due to the small sampling area, in practice top-view TEM is suitable in detecting the threading dislocation density higher than roughly 10^6 cm^{-2} [122]. In general, TEM measurements of TDDs in low defect density materials should always be confirmed with wide area techniques. Moreover, TEM requires extensive and skillful sample preparations. On the other hand, a conventional alternative method for measuring TDDs is the EPD technique with selective etching. The EPD method is suitable for samples with low TDDs ($<10^6$ cm^{-2}) since a large surface area can be imaged under an optical microscope. The EPD method is not applicable for the samples with high TDDs and will underestimate the value of TDD because multiple dislocations may overlap in one etch pit. In Ref.[123], it was pointed out that there is a disagreement between EPD and plan-view TEM counted TDDs. The TDD from the EPD method is often half of that from TEM measurement [123, 124].

In 1986, based on the EPD results of GaAs thin films on Si substrate, Stirland and his coworkers built a statistical model including all the overlapping probabilities of etch pit [125, 126]. They found that the apparent TDD can be expressed as

$$\rho_{EPD} = \frac{1-\exp(-\pi\rho r^2)}{\pi r^2} \qquad 3.26$$

where ρ_{EPD} is the TDD measured by the EPD technique with the pit overlapping impact, and ρ is the TDD without the overlapping issue, and r is the etching resolution parameter defined as the closest distance at which two similar etch-pits can be distinguished.

With TEM measurements, the overlapping issue can be eliminated. The TDD from TEM measurements can be regarded as ρ. Therefore, the TDD ratio between EPD and TEM can be quantitatively estimated by the equation as follows:

$$\frac{\rho_{EPD}}{\rho_{TEM}} = \frac{1-\exp(-\pi\rho_{TEM} r^2)}{\pi\rho_{TEM} r^2} \qquad 3.27$$

For a Ge etch solution, the typical r value is approximately 1 micron. For the TDD of 10^6 ~ 10^7 cm^{-2}, the ratio of ρ_{EPD}/ρ_{TEM} varies from 0.98 to 0.85 based on the equation above [121].

For SiGe epitaxial structures in this work, the chromium-based etching solution was used. A modified Schimmel solution was employed, which consisted of 55 Vol% CrO_3 (0.40M) and 45 Vol% HF (49%).[127] The etch rate is approximately 60 nm/min for Si, 400 nm/min for $Si_{0.75}Ge_{0.25}$, less than 200 nm/min for $Si_{0.50}Ge_{0.50}$, and less than 100 nm/min for pure Ge. After selective etching, the sample surfaces were imaged by an optical microscope with bright/dark field modes, and the images were captured via a CCD camera.

3.7 Chapter summary

Multi-layer epitaxial samples were designed and grown for this study with $Si_{1-x}Ge_x/Si_{1-y}Ge_y/Si_{1-x}Ge_x$ ($y > x$) film stacks as the key interdiffusion structure. Based on the Matthews Blakeslee equilibrium limit, the three sets are divided into two types: the compressive $Si_{1-y}Ge_y$ layers of S4065 and S5075 are in the stable regime; that of S4585 is metastable. Three characterization techniques (SIMS, Raman and XRD) were introduced and discussed in details for the measurements of Ge fraction and strain in each layer of the samples. In order to estimate the impact of threading dislocations, the etch pit density technique was selected to characterize the TDD in those epitaxial structures.

Chapter 4 A Unified Interdiffusivity Model and its Verification for Si-Ge Interdiffusion without Strain over the Full Germanium Fraction Range

4.1 Introduction and literature review of Si-Ge interdiffusion

Major effort in Si-Ge interdiffusion research started in the 1990's. Several groups measured the interdiffusion at the Si/SiGe interfaces with various techniques such as secondary ion mass spectrometry (SIMS) [67, 68, 128], Rutherford backscattering spectrometry [89, 129], X-ray diffraction (XRD) [130-133], Raman spectroscopy [134] and photoluminescence [135]. Typical interdiffusion structures studied in the 90's were $Si/Si_{1-x}Ge_x$ (x_{Ge} < 0.3) superlattices with thicknesses from 30 nm to a few microns. Due to the scaling of electronic and optoelectronic devices and the changes in structures and fabrication techniques, the typical diffusion lengths of Si-Ge interdiffusion during thermal anneals are comparable to the thickness (1 to 100 nm) of SiGe thin films in the devices. x_{Ge} employed in current devices was also much higher than in previous studies. Therefore, in the last decade, Si-Ge interdiffusion has been revisited by many research groups. Experimentally, there are two popular approaches to study Si-Ge interdiffusivity. One is using high resolution X-ray diffraction (HRXRD) to measure interdiffusivities in a multiple layered superlattice structure, as demonstrated by Aubertine, Meduna, Ozguven and Liu *et al*. [16-20].

The fundamental physics underlying this approach is the correlation between Si-Ge interdiffusivity and the Bragg reflection superlattice satellite decay rate in a superlattice structure. The correlation can be expressed as

$$\frac{d}{dt}\left[\frac{I(t)}{I(0)}\right] = -\frac{8\pi^2}{\lambda^2}\widetilde{D}, \qquad 4.1$$

where $I(t)$ is the superlattice satellite intensity measured by XRD as a function of the anneal time t, λ is the spatial period of the superlattice, and $\widetilde{D}$ is the interdiffusivity.

This technique utilized the ultrahigh sensitivity of X-ray diffraction from concentration modulated films such as $Si_{1-x}Ge_x/Si_{1-y}Ge_y$ superlattices, where the Ge fraction changes with depth in a pattern similar to a square wave. However, as Aubertine *et al.* pointed out [16], when it is applied to concentration dependent interdiffusion like Si-Ge interdiffusion, a postulate must be made such that the interdiffusivity is effectively constant over the range of concentrations present in a $Si_{1-x}Ge_x/Si_{1-y}Ge_y$ superlattice with a low concentration modulation amplitude. Correspondingly, the Ge fraction used in the final $\widetilde{D}$ expression is a thickness-weighted average Ge fraction ($x_{Ge,average}$) of the whole superlattice structure. Aubertine *et al.*'s work focused on the interdiffusion in multiple quantum wells (MQW) with x_{Ge} below 0.2 in the temperature range from 770 to 880 °C, and modeled the interdiffusivity with a concentration-dependent diffusivity pre-factor D_0 and activation energy E_a [16]. With the similar structures and technique to those in Aubertine *et al*.'s study, Ozguven *et al*. measured the interdiffusivity at $x_{Ge,average}$ =0.91. To obtain a relatively accurate interdiffusivity, the x_{Ge} modulation amplitude in one period of the MQWs is 0.05 in both Aubertine *et al's* and Ozguven *et al*'s work.

With much larger x_{Ge} modulation amplitudes of 0.30, 0.80, 0.45 and 0.15 in one period of the MQWs, Meduna *et al*. investigated Si-Ge interdiffusion at four $x_{Ge,average}$ values (0.25, 0.50, 0.70 and 0.90) and obtained similar interdiffusivity formulas to Aubertine's. Liu *et al*. measured the interdiffusivity at $x_{Ge,average}$ =0.85 with a x_{Ge} modulation amplitude of 0.35 in their MQWs. There is a significant issue with large x_{Ge} modulation amplitudes in MQWs. First, the Ge fraction corresponding to the interdiffusivity is taken as the $x_{Ge,average}$ of MQWs or measured by Rutherford backscattering spectrometry. This may not be a valid method to obtain the nominal Ge value used in the $\widetilde{D}$ models as the interdiffusion depends on x_{Ge} exponentially instead of linearly. For one period of a MQW ($Si_{0.45}Ge_{0.55}$/Ge), the interdiffusivity in the Ge layer is almost 1000 times larger than that in the $Si_{0.45}Ge_{0.55}$ layer according to the model in Ref. [21]. Once the interdiffusion starts, Ge atoms diffuse out to the lower Ge fraction layer, which reduces the interdiffusivity difference between the two layers. However, interdiffusion still depends on Ge fraction exponentially instead of linearly. Obviously the interdiffusivity $\widetilde{D}$ derived from this process is not exactly the $\widetilde{D}(x_{Ge,average})$.

The other technique employs secondary ion mass spectrometry (SIMS) [10, 21]. Based on the SIMS data (Ge fraction versus depth) obtained from device-relevant structures, the Boltzmann-Matano method was used to extract interdiffusivity as a function of Ge fraction from the diffused Ge profiles. Then based on the extracted interdiffusivities and the linear fittings to those data, Xia *et al*. built a $D_R D_C$ model (D_R denotes interdiffusivity under full relaxation while D_C under full compressive strain) to describe the Si-Ge interdiffusivities under relaxed, tensile and compressive stress [10]. With an abrupt step structure Si/Ge, Gavelle *et al*. concluded the interdiffusivity with a two-term formula, one term for the dislocation assisted interdiffusion at low Ge fraction, and the other for the concentration dependent interdiffusion at high Ge fraction [21]. Due to the high dislocation density (10^{10} cm^{-2}) in their structure, Gavelle's conclusion is of less relevance to the current SiGe devices with dislocation densities normally under 10^6 cm^{-2}. We

summarized the temperature and Ge fraction ranges in the interdiffusion studies cited above in Figure 4.1. Clearly, the temperature and Ge fraction ranges used in previous studies are scattered and no unified Si-Ge interdiffusion model over the full Ge fraction range has been established, which is addressed in this chapter. On the other hand, self-diffusion of Si and Ge in a SiGe homogeneous system has been investigated experimentally and theoretically, but until now, no quantitative correlation between Si-Ge interdiffusivity and Si and Ge self-diffusivities has been established.

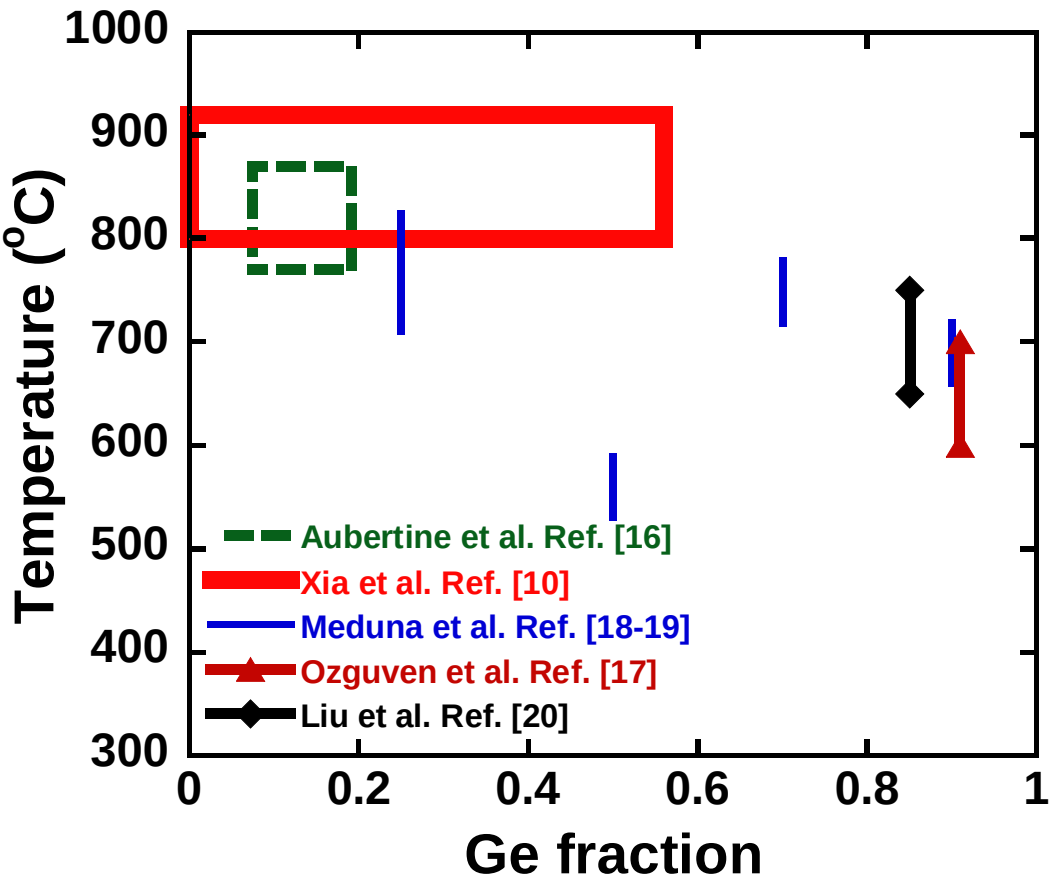

Figure 4.1 Summary of the temperature and Ge fraction ranges studied in the selected literature on Si-Ge interdiffusion.

4.2 A new approach of interdiffusivity modeling based on self-diffusivity

In this chapter, a Si-Ge interdiffusivity model is established by a new approach, which is based on the correlation between Si and Ge self-diffusivities and Si-Ge interdiffusivity over the full Ge fraction range. Before going into the details of the derivation, let's first clarify the difference and correlation between self-diffusion, intrinsic diffusion, interdiffusion and their corresponding diffusivities.

4.2.1 Clarification of the difference and correlation between self-diffusion, intrinsic diffusion and interdiffusion

For solid state materials, generally diffusion indicates the atom movement driven by a chemical potential gradient, and the mass flux of atoms can be expressed as

$$J = C \cdot \vec{V} = C \cdot \left(M \cdot \vec{F}\right), \tag{4.2}$$

where C, $\vec{V}$, M and $\vec{F}$ denote the concentration, velocity, mobility and the driving force [42].

For the one-dimension case along i axis (i stands for $x, y,$ or z), the driving force is opposite to the chemical potential gradient,

$$\vec{F} \cdot e_i = -\frac{\partial \mu}{\partial i}, \tag{4.3}$$

where μ is the chemical potential and e_i is the unit vector of i axis.

Based on classic thermodynamics, at fixed pressure and temperature, the chemical potential for component A is

$$\mu(C_A) = \mu_0 + R_g T \ln a \text{ , and } a = x_A \gamma, \; x_A = C_A / C_{total} \quad 4.4$$

where C_A, μ_0, R_g, T, a , x_A, γ and C_{total} denote the concentration of component A, the reference chemical potential, the ideal gas constant, the absolute temperature, the chemical activity, the mole fraction, the chemical coefficient of component A, and the total concentration of all components [39].

Then the chemical potential gradient at pressure P, temperature T and time t can be expressed as

$$\left(\frac{\partial \mu}{\partial i}\right)_{P,T,t} = R_g T \left(\frac{\partial \ln a}{\partial i}\right) \quad 4.5$$

Combining Equations 4.2-4.5, we can obtain Fick's first law

$J_i = -MR_gT\left(\frac{\partial C}{\partial i}\right)\left(\frac{\partial \ln a}{\partial \ln x_A}\right) = -D\left(\frac{\partial C}{\partial i}\right)$, where the intrinsic diffusivity D can be expressed as:

$$D = MR_gT\left(\frac{\partial \ln a}{\partial \ln x_A}\right) \quad 4.6$$

The term $\frac{\partial lna}{\partial lnx_A}$ counts for the chemical mixing effect. For ideal solutions, such as a mixture of different isotopes of one element, $\frac{\partial lna}{\partial lnx_A}$ = 1. The diffusivity of one isotope in these chemically homogenous solutions is called self-diffusivity D^*, macroscopically expressed as $D^* = MR_gT$. In reality, solutions in Raoultian and Henrian limits, such as low to medium doping in

semiconductors, are very close to ideal solutions, where the chemical mixing effect can be ignored.

For non-ideal solutions, $\frac{\partial lna}{\partial lnx_A} \neq 1$, and the influence from chemical mixing cannot be ignored. In these cases, the diffusivity D is intrinsic diffusivity. The relation of self-diffusivity and intrinsic diffusivity can be expressed as

$$D_A = D_A^*(\frac{\partial \ln a_A}{\partial \ln x_A}) = D_A^*(1+\frac{\partial \ln \gamma_A}{\partial \ln x_A}) \ , \qquad 4.7$$

where A stands for a species in a solid solution and x_A stands for A's atomic fraction.

In a binary solid solution with element A and B, such as SiGe alloys, the interdiffusion process in the laboratory frame can be described completely by the interdiffusivity $\tilde{D}$ in Darken's second equation shown in Chapter 2.

$$\tilde{D} = D_A x_B + D_B(1-x_A) \qquad 4.8$$

4.2.2 Literature review of Si and Ge self-diffusivities

After the clarification of the concepts above, let's review the literature in Si and Ge self-diffusivities. The studies of Si and Ge self-diffusivities (D_{Si}^* and D_{Ge}^*) based on the Si and Ge isotope diffusion under zero Ge concentration gradient have been reported since 1970's [136], especially, the self-diffusivity of Ge in $Si_{1-x}Ge_x$ alloys has been widely studied with different Ge isotopes [24-28]. Due to the short lifetime of Si isotopes, however, there were few systematic studies of Si self-diffusivity in $Si_{1-x}Ge_x$ alloys until the recent work by Kube *et al* [29, 30]. In their work, the impact of $\left(1+\frac{\partial ln\gamma}{\partial lnx}\right)$ was ruled out by a sophisticatedly designed sample structure, where Si and Ge isotopes diffuse in a multi-layered structure with a uniform

distribution of the total Ge concentration. There is no chemical energy gradient, but only the concentration gradient of the isotopes themselves. Then they used time of flight secondary ion mass spectrometry (ToF-SIMS) to measure the isotope's profiles and extracted the self-diffusivities of Si and Ge precisely [29, 30]. Based on those experimental data summarized in Ref. [29, 30], D_{Si}^{*} and D_{Ge}^{*} were first obtained simultaneously at six x_{Ge} values up to 100% Ge. However, as discussed above, no quantitative correlation between Si and Ge self-diffusivities and Si-Ge interdiffusivity has been established.

4.2.3 Derivation of the new model based on Si and Ge self-diffusivities

For SiGe system, based on Darken's second equation, the interdiffusivity can be expressed as

$$\tilde{D} = D_{Si}x_{Ge} + D_{Ge}(1-x_{Ge}) \qquad 4.9$$

The combination of Equation 4.7 and 4.9 gives the relation in Equation 4.10, which is the basis of the modeling in this work.

$$\tilde{D} = D_{Si}^{*}(1+\frac{\partial \ln \gamma_{Si}}{\partial \ln x_{Si}})x_{Ge} + D_{Ge}^{*}(1+\frac{\partial \ln \gamma_{Ge}}{\partial \ln x_{Ge}})(1-x_{Ge}) \qquad 4.10$$

In the following, we will discuss how the parameters in Equation 4.10, such as D_{Si}^{*}, D_{Ge}^{*}, γ_{Si} and γ_{Ge} are modeled and calculated.

D_{Si}^{*} and D_{Ge}^{*} measured in Ref. [29, 30] make it possible to establish a quantitative relation between D_{Si}^{*} , D_{Ge}^{*} and $\widetilde{D}$. Kube *et al*.' work only measured D_{Si}^{*} and D_{Ge}^{*} at six x_{Ge} values in the 0% to 100% Ge fraction range, and the interpolation of these data was made using Arrhenius relation in Equation 4.11, where $D_{Si,0}^{*}$ and $D_{Ge,0}^{*}$ are the prefactors and E_a is the activation energy. $D_{Si,0}^{*}$, $D_{Ge,0}^{*}$ and E_a are all Ge concentration dependent.

$$D_j^*(x_{Ge}) = D_{j,0}^*(x_{Ge})e^{\frac{-E_a(x_{Ge})}{kT}}, \ j = Si \ or \ Ge \qquad 4.11$$

The values of prefactor $D_{Si,0}^*$ and $D_{Ge,0}^*$ over the full x_{Ge} range were obtained by fitting the experimental data at multiple temperatures using Arrhenius law in Ref. [27, 28] and [29, 30]. $D_{Si,0}^*$ and $D_{Ge,0}^*$, these two prefactors strongly depend on the formation and migration entropy of the defects (mostly interstitials and vacancies) [137], but they are complicated and difficult to model theoretically [16]. Hence, to extract the continuous values of practical $D_{Si,0}^*$ and $D_{Ge,0}^*$ over the full Ge fraction range, we used a second order polynomial fitting to interpolate Kube's data, shown in Figure 4.2. $D_{Si,0}^*$ and $D_{Ge,0}^*$ can be expressed as, $D_{Si,0}^*(x_{Ge})$ = exp ($a_0 + a_1 x_{Ge} - a_2 x_{Ge}^2$)and $D_{Ge,0}^*(x_{Ge})$ = exp ($b_0 + b_1 x_{Ge} - b_2 x_{Ge}^2$), where a_0= 6.489±0.250, a_1= 4.964±1.357, a_2= 7.829±1.346; b_0 = 6.636±0.241, b_1 = 8.028±1.311, b_2 = 11.318±1.300. All the extracted parameters are dimensionless.

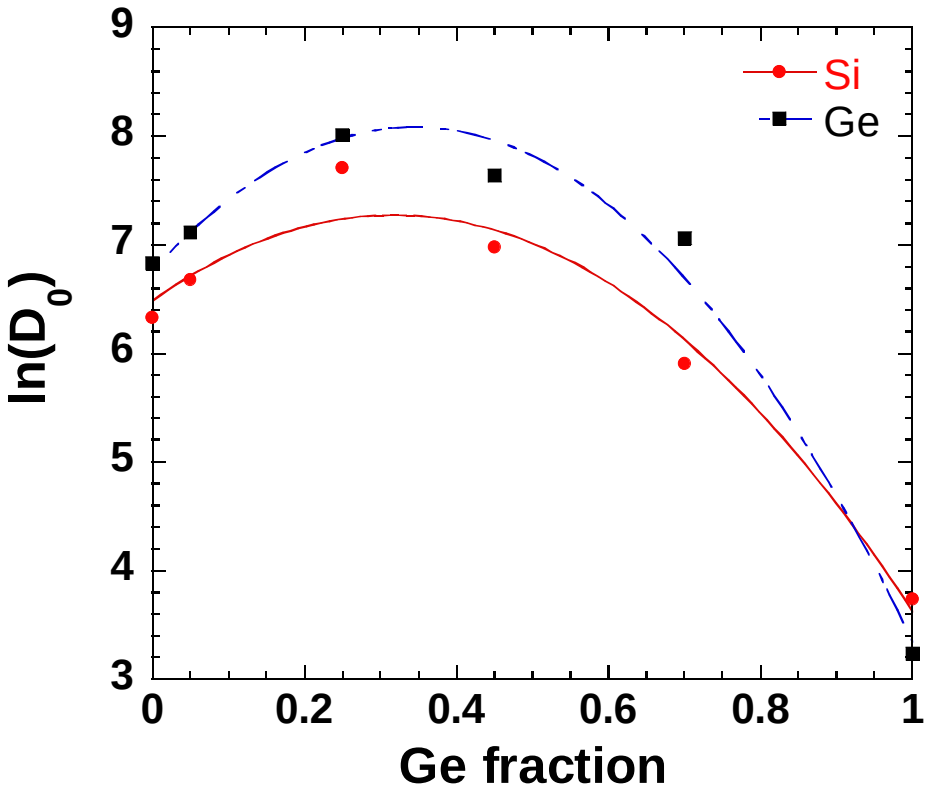

Figure 4.2 The second order polynomial fitting to interpolate Kube's data of prefactors of Si and Ge self diffusivities over the full Ge fraction range.

The activation energy E_a of Si and Ge self-diffusivities follows a modified Vegard's law as in Equation 4.12 [30]. To maintain the data's consistency, the parameters $E_a(0)$, $E_a(1)$ and Θ are all taken from Ref. [30]. For Si self-diffusivity in SiGe alloys, the parameters $E_a(0)$, $E_a(1)$ and Θ are 4.76 eV, 3.32 eV and 1.54 eV respectively; while for Ge self-diffusivity, 3.83 eV, 3.13 eV and 1.63 eV.

$$E_a(x_{Ge}) = (1-x_{Ge})E_a(0) + x_{Ge}E_a(1) + x_{Ge}(1-x_{Ge})\Theta \qquad 4.12$$

where $E_a(0)$ is the activation energy in pure Si, $E_a(1)$ is the activation energy in pure Ge, and Θ is the bowing parameter.

After having $D^*_{Si,0}$, $D^*_{Ge,0}$ and E_a modeled, the self-diffusivities of Si and Ge are calculated over the full Ge fraction range based on Equation 4.11. The calculated self-diffusivities of Si and Ge are plotted in Figure 4.3 (a) and (b) respectively, in comparison with the experimentally measured self-diffusivity data at 900°C in Ref. [26-30]. The self-diffusivity models agree with Kube's and Strohm's data, as seen in Figure 4.3, which confirms the effectiveness of the interpolation method for $D^*_{Si,0}$ and $D^*_{Ge,0}$.

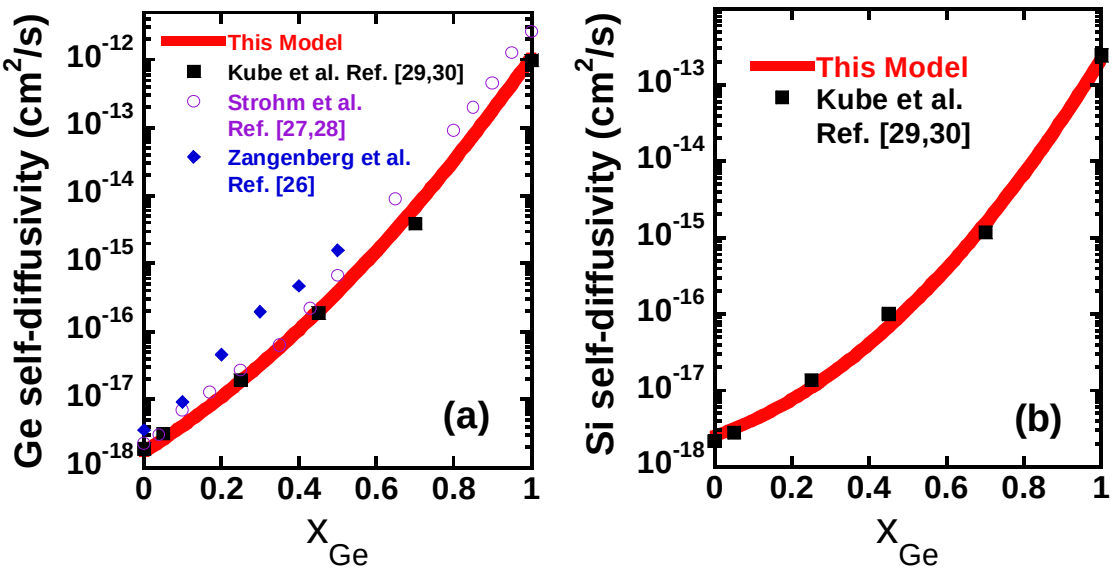

Figure 4.3 Comparison between the model calculation using Equation 4.11 and 4.12 and experimental data of (a) Ge self-diffusivities and (b) Si self-diffusivities at 900 °C.

After the self-diffusivities D^*_{Si} and D^*_{Ge} over the full Ge fraction range were calculated, the factor $(1 + \frac{\partial ln\gamma}{\partial lnx})$ in Equation 4.10 is still unknown over the full Ge fraction range. For this purpose, it is assumed that the SiGe solid solution is a regular solution, where the entropy of mixing is the same as that for an ideal solution. The partial molal enthalpy $\Delta\overline{H}$ of Si and Ge in a SiGe solid solution can be expressed as in Equation 4.13 [39], where α is the interaction parameter. According to the measurements by V. T. Bublik *et al.*, α is linear with x_{Ge} as shown in Equation

4.14 [138]. Then the $\partial ln\gamma / \partial lnx$ terms for Si and Ge can be calculated with Equation 4.15. Theoretically the $\partial ln\gamma / \partial lnx$ term should be identical for Si and Ge, and the calculated results based on the experimental interaction parameter α are indeed very close. The subtle difference between $\partial ln\gamma_{Si} / \partial lnx_{Si}$ and $\partial ln\gamma_{Ge} / \partial lnx_{Ge}$ is caused by the asymmetry of the interaction parameter α over Ge fraction. Based on Equation 4.15, we can see $\partial ln\gamma / \partial lnx$ is negative and its absolute value decreases as the temperature increases, shown in Figure 4.4. For the low (x_{Ge} < 0.05) and high (x_{Ge} < 0.95) Ge fraction ends, the absolute value of $\partial ln\gamma / \partial lnx$ is less than 0.10, so the difference between self-diffusivity and intrinsic diffusivity is less than 10%. However, for a medium Ge fraction range, the absolute value of $\partial ln\gamma / \partial lnx$ is around 0.30~0.50 in the common temperature range (800 °C~1200 °C) used for anneals. We can see a regular solution model gives a more accurate description of Si-Ge interdiffusion than an ideal solution where $\frac{\partial ln\gamma}{\partial lnx}$ = 0. Finally, the Si-Ge interdiffusivity is calculated by using Equation 4.10 and 4.15, which completes the modeling of Si-Ge interdiffusivity. In figure 4.4 (b), the impact of the term $(1 + \frac{\partial ln\gamma}{\partial lnx})$ on the simulated profiles is shown for Sample BM60 with a thermal budget of 1015 °C for 30 seconds. If the term $\left(1 + \frac{\partial ln\gamma}{\partial lnx}\right)$ is not there in Darken's equation (equivalently for an ideal solution), there is more interdiffusion compared with the accurate interdiffusivity equation.

$$\begin{aligned} \Delta\overline{H}_{Si} &= R_g T \ln\gamma_{Si} = \alpha x_{Ge}^2 \\ \Delta\overline{H}_{Ge} &= R_g T \ln\gamma_{Ge} = \alpha(1-x_{Ge})^2 \end{aligned} \qquad 4.13$$

$$\alpha = 8787 - 1339 x_{Ge} (J/mol) \qquad 4.14$$

$$\begin{aligned} \frac{\partial \ln\gamma_{Si}}{\partial \ln x_{Si}} &= \frac{(1-x_{Ge})x_{Ge}(4017x_{Ge} - 17574)}{R_g T} \\ \frac{\partial \ln\gamma_{Ge}}{\partial \ln x_{Ge}} &= \frac{(1-x_{Ge})x_{Ge}(4017x_{Ge} - 18913)}{R_g T} \end{aligned} \qquad 4.15$$

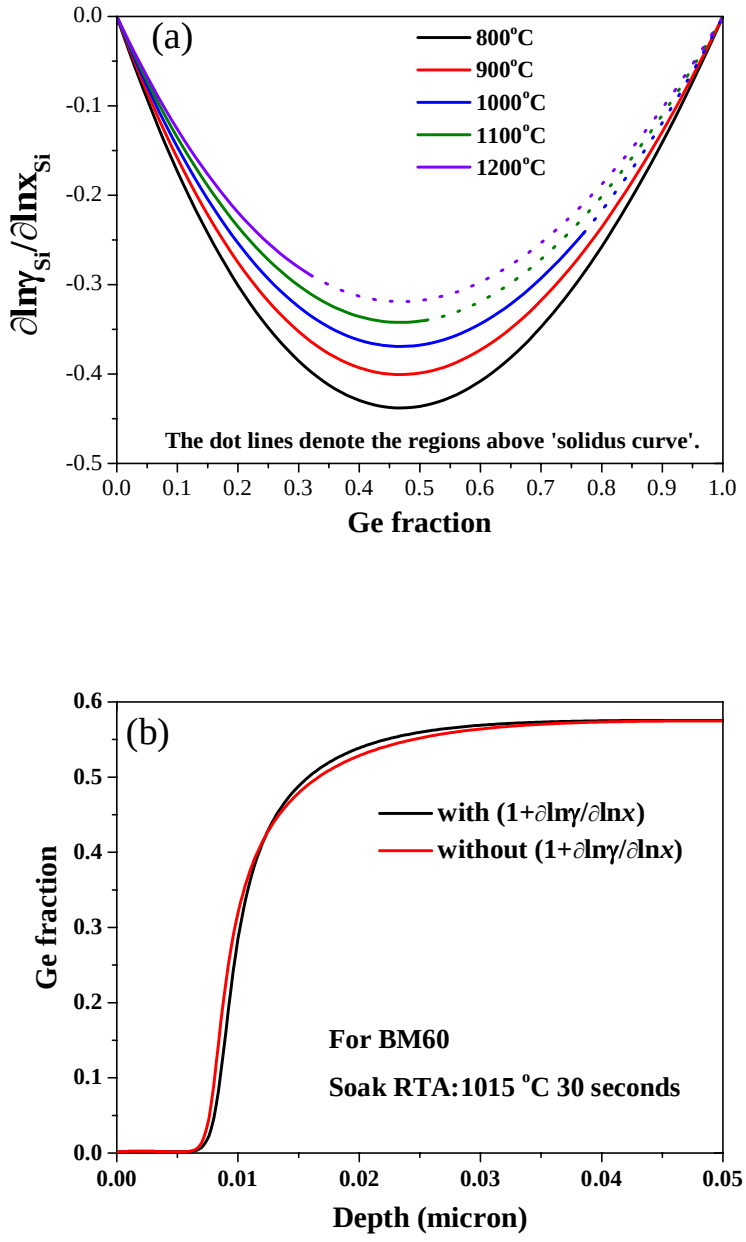

Figure 4.4 (a) Temperature dependence of $\partial ln\gamma_{Si}/\partial lnx_{Si}$ over the full Ge fraction range, which shows the difference between regular solution models and ideal solution models. For 1000 °C, 1100 °C and 1200 °C, over some x_{Ge} point, SiGe alloys are above the 'solidus curve', which are denoted with dot lines; (b) Impact of $(1+\frac{\partial ln\gamma_{Si}}{\partial lnx_{Si}})$ on the simulated profiles for BM60 annealed at 1015 °C for 30 seconds.

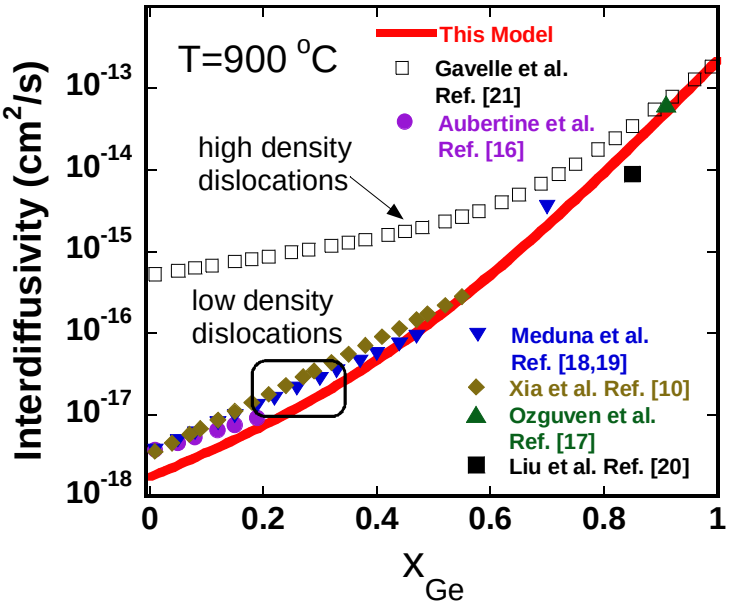

Figure 4.5 Si-Ge interdiffusivity calculated using this model in comparison with literature models at 900°C.

The interdiffusivity at T= 900 °C calculated with this model is shown in Figure 4.5 in comparison with the literature models. This interdiffusivity model shows a good consistency with the results in Ref. [10, 16, 18, 19] in the low x_{Ge} range. At the high x_{Ge} end, Ozguven *et al*.'s experimental $\tilde{D}$ at $x_{Ge,average}$ =0.91 and Liu *et al*.'s $\tilde{D}$ result at $x_{Ge,average}$ =0.85 showed good agreement with our model. During the long-time anneals (several days) in the studies using HRXRD technique (described in Section 4.1), the interdiffusivity has a strong time dependence [16-20]. So the interdiffusivity obtained by Equation 4.1 is an effective interdiffusivity over the whole annealing time. Although there is certain strain field in their as-grown samples, the strain's impact was suppressed during the long-time anneals. That is why their models are close to our model. Our model also matched Gavelle's results well for x_{Ge} ≥0.85. Due to the high dislocation density (10^{10} cm^{-2}) in the structures studied in Gavelle *et al*.'s work (samples in other work have dislocation densities in the 10^5 to 10^6 cm^{-2} range), Si-Ge interdiffusion in their work has a large

through-dislocation-diffusion component that dominates in the x_{Ge} <0.50 range, which results in a much faster interdiffusion in that range.

Since the model in this work is based on the self-diffusivity data in Ref. [29, 30] with a temperature range from 880 to 1270 °C at x_{Ge} =0 end, and from 550 to 900 °C at x_{Ge} =1 end, correspondingly, the new model is valid in this temperature range. At the high x_{Ge} end, the interdiffusivity exhibits good accuracy at 900 °C (shown in Figure 4.5), which is already close to the melting point of Ge.

4.3 Model verification for Si-Ge interdiffusion under three types of anneal conditions

As discussed above, this model was based on self-diffusion experiments under furnace anneal conditions using SiGe alloys with no chemical concentration gradient. In terms of strain, the structures studied in self-diffusion experiments were free of strain. As it was shown that tensile strain has a negligible impact on the interdiffusivity in Ref. [10], our interdiffusivity model can then be employed to the interdiffusion under tensile strain as well as under zero strain. It is also important to investigate whether this model works for other types of anneal conditions, such as soak RTAs and spike RTAs. RTAs have much higher temperature ramp rates than furnace anneals, and are the mainstream anneal technique in the semiconductor industry, which bears more technological significance.

To verify the new interdiffusivity model, it was implemented in a major semiconductor process simulator, TSUPREM-4^{TM} (see Appendix A), which is the industry-standard 1D/2D process simulation tool that is widely used by semiconductor companies to optimize IC fabrication processes [139]. First, simulation results using our model were compared with previously published experimental results under furnace anneal conditions in Ref. [10]. Then, interdiffusion

experiments were designed and conducted under soak RTA and spike RTA conditions at Mattson Technology, Canada. As-grown and annealed Ge profiles were measured by SIMS. Finally, the model predictions calculated by the simulation tools were compared with the experimental Ge profiles under soak RTA and spike RTA anneals. The details of the model verifications are discussed below.

4.3.1 Model verification for interdiffusion under furnace anneal conditions

Furnace anneals are traditionally employed in the semiconductor device manufacturing. They are also widely used in diffusion studies to conduct isothermal anneal experiments. In Ref. [10], furnace anneals were employed for time durations from 30 minutes to 80 hours. In order to prove the validity of our interdiffusivity model, comparisons were made with the literature experiment data obtained from two structures: BM20 and BM60. BM20 and BM60 are tensile-strained-Si/relaxed $Si_{1-x}Ge_x$ structures with x = 0.20 and 0.55 respectively (BM60 was designed to have x = 0.60, but the measured value was 0.55).

The structure of BM20 and BM60 is shown in Figure 4.6. The details of the experiments were described in Ref. [10]. The anneal conditions of the three samples are shown below:

1) BM20-I furnace annealed at 800 °C for 80 hours.
2) BM20-II furnace annealed at 920 °C for 60 minutes.
3) BM60 furnace annealed at 880 °C for 90 minutes.

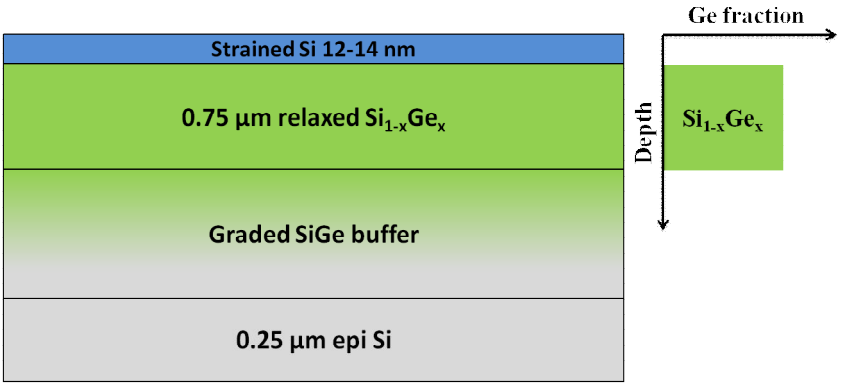

Figure 4.6 Tensile-strained Si/relaxed Si1-xGex structures used in Ref. [10] with x=0.20 and 0.60 respectively.

As shown in Figure 4.7 and Figure 4.8, the Ge profiles predicted by the new model in TSUPREM-4^{TM} present a great consistency to the measured Ge SIMS data of the BM20 samples annealed at two different conditions.

After verifying our model with the BM20 experimental data, another comparison was done with the Ge SIMS profile of the BM60 sample annealed at 880 °C for 90 minutes. The new model agrees with the experimental data at the high Ge fraction end. At the low Ge fraction tail, there is a considerable discrepancy caused by dislocations, shown in Figure 4.9. The BM60 sample has a step structure (Si cap on SiGe) described in Ref. [10]. The thickness of the Si cap is 12-14 nm, which is much thicker than the critical thickness of the Matthews- Blakeslee limit for x_{Ge} =0.55 [70]. This means that the dislocation generation during anneals is favored thermodynamically, which provides more fast diffusion paths that mainly impact the interdiffusion in the low Ge fraction range. More discussion on this tail issue is included in Chapter 6. Nevertheless, our model shows good predictions for all the three cases under furnace anneal conditions.

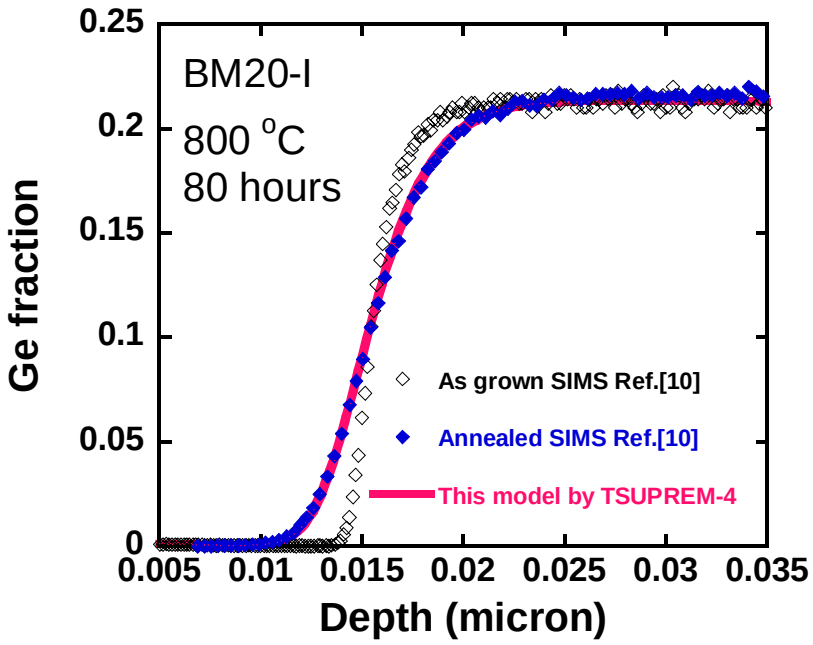

Figure 4.7 As-grown, annealed Ge SIMS profiles of a strained-Si/relaxed $Si_{0.8}Ge_{0.2}$ structure from Ref. [10] and this model prediction simulated by TSUPREM-4™. The anneal was performed at 800 °C for 80 hours in an inert ambient.

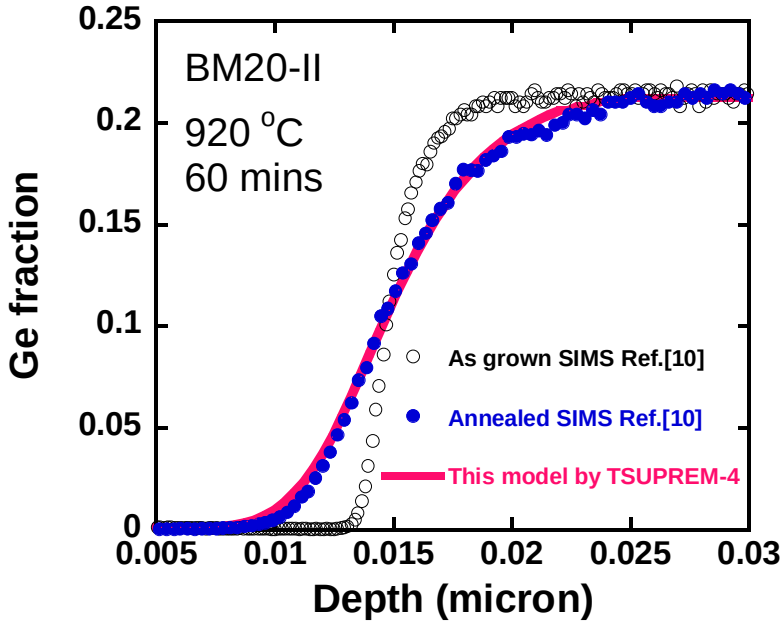

Figure 4.8 As-grown, annealed Ge SIMS profiles of a strained-Si/relaxed $Si_{0.8}Ge_{0.2}$ structure from Ref. [10] and this model prediction simulated by TSUPREM-4™. The anneal was performed at 920 °C for 60 minutes in an inert ambient.

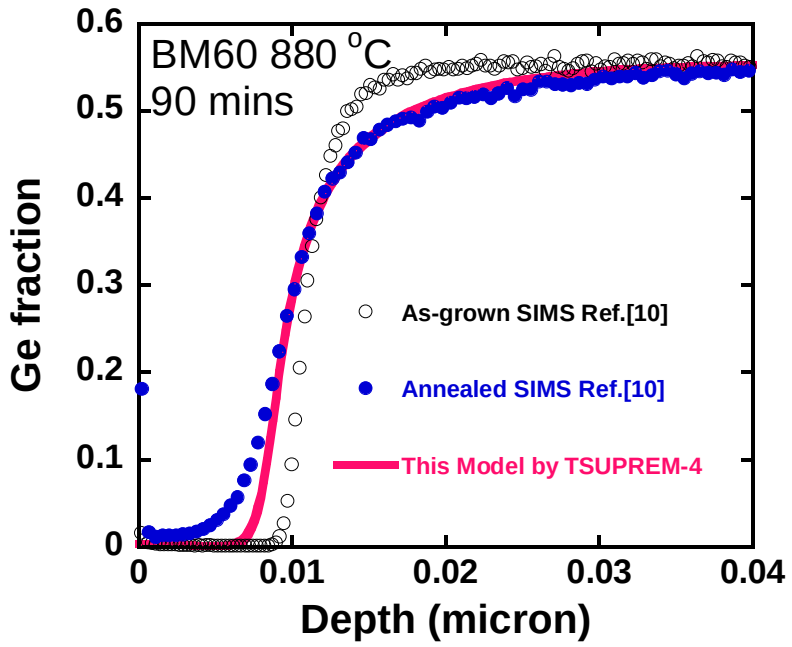

Figure 4.9 As-grown, annealed Ge SIMS profiles of a strained-Si/relaxed $Si_{0.4}Ge_{0.6}$ structure from Ref. [10] and this model prediction simulated by TSUPREM-4™. The anneal was performed at 880 °C for 90 minutes in an inert ambient.

4.3.2 Model verification for Si-Ge interdiffusion under soak and spike RTA conditions

As modern semiconductor devices scale down, furnace anneals are no longer the mainstream high-temperature anneal technique for advanced devices, and have been replaced by the rapid thermal anneals with much faster heating rates and thus smaller thermal budgets. “Soak RTAs” normally have an anneal time from a few to tens of seconds at the peak temperature, while “spike RTAs” have dwelling times at the peak temperature minimized. Si-Ge interdiffusion studies under RTA conditions are still incomplete, but they are of great significance for the SiGe based modern transistors involving RTA processes. Therefore, after our model was verified by comparison with the SIMS data under furnace anneals, the simulations by our new model are compared with the Si-Ge interdiffusion behaviours under soak and spike RTAs. The annealed samples are BM30 and BM60, which were grown for Xia’s work in Ref. [10]. They are tensile-

strained-Si/relaxed $Si_{1-x}Ge_x$ structures with x = 0.30 and 0.55 respectively (BM60 was designed to have x = 0.60, but the measured value was 0.55). The RTA anneals were conducted at Mattson Technology Canada on small wafer pieces in ambient air. As it was shown that the oxidizing ambient has no impact on Si-Ge interdiffusion [79], the interdiffusion in ambient air should be the same as that in an inert ambient. Our interdiffusion model was derived from Si and Ge self-diffusivities in an inert ambient should also work for the interdiffusion in ambient air, which was confirmed by the experimental data shown in Figure 4.10, Figure 4.11, Figure 4.13 and Figure 4.14. The anneal experiments are summarized in Table 4.1 below. Spike RTAs with T_{peak} at 1160 °C and 1180 °C were also tried for structure BM60, surface degradation was observed for these two temperatures. The fact that 1160 °C and 1180 °C are very close to the solidus line in the Si-Ge equilibrium phase diagram suggests that the surface degradation is possibly caused by the melting of $Si_{0.45}Ge_{0.55}$ layer [35].

Table 4.1 Experimental details of soak and spike RTA performed on BM30 and BM60 samples.

RTA type	BM30	BM60
Soak RTA	1040 °C, 30secs	1015 °C, 30secs
Spike RTA	T_{peak}=1200 °C Ramp-up rate=560 °C /sec Ramp-down rate=100 °C /sec	T_{peak}=1140 °C, 1160 °C, 1180 °C Ramp-up rate=560 °C /sec Ramp-down rate=100 °C /sec

After the anneal experiments, the Ge profiles were measured by SIMS. The SIMS data were compared with the model predictions by TSUPREM-4^{TM}. A good consistency with the experimental results is obtained for sample BM30 and BM60 under soak RTAs, as shown in Figure 4.10 and Figure 4.11. It is shown that the new model works very well for soak RTAs with a tens-of-seconds anneal time at peak temperatures.

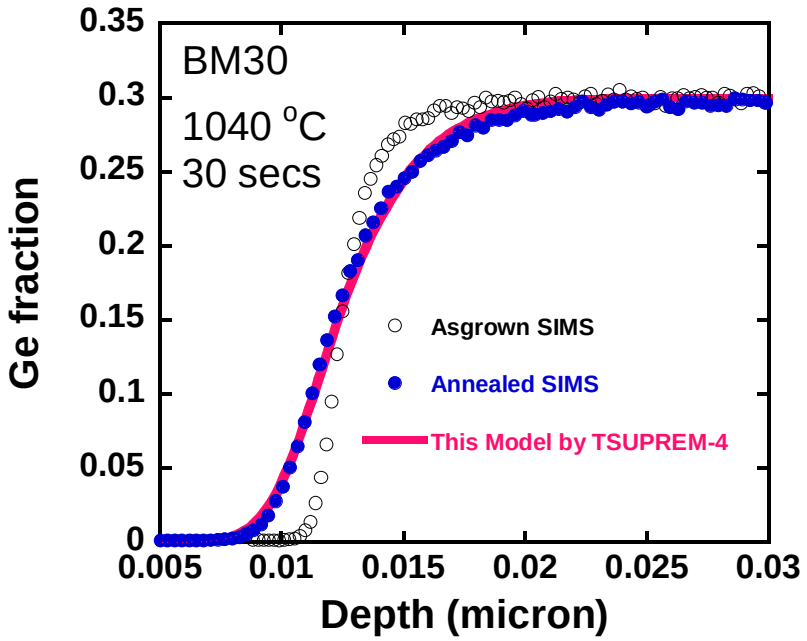

Figure 4.10 As-grown, annealed Ge SIMS profiles of a strained-Si/relaxed $Si_{0.7}Ge_{0.3}$ structure and this model prediction simulated by TSUPREM-4™ . The soak RTA was performed at 1040 °C for 30 seconds.

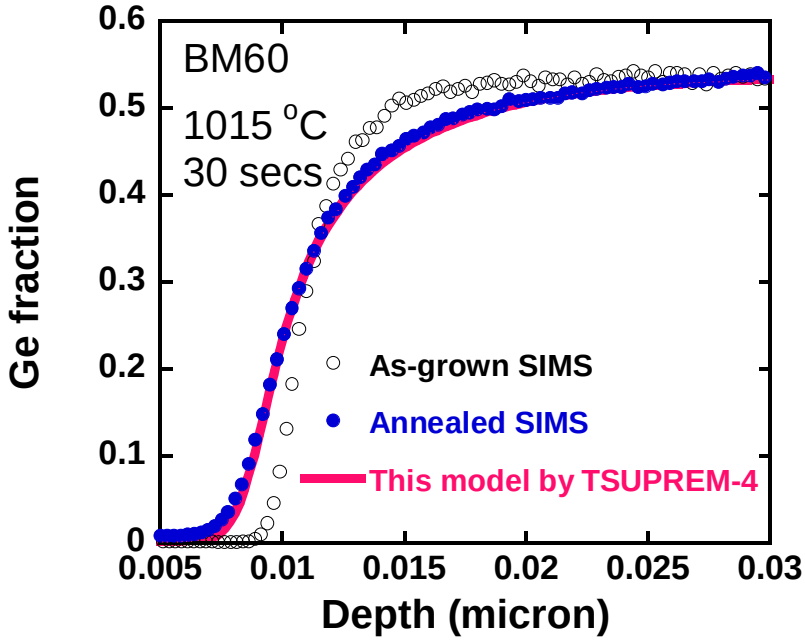

Figure 4.11 As-grown, annealed Ge SIMS profiles of a strained-Si/relaxed $Si_{0.45}Ge_{0.55}$ structure and this model prediction simulated by TSUPREM-4™ . The soak RTA was performed at 1015 °C for 30 seconds.

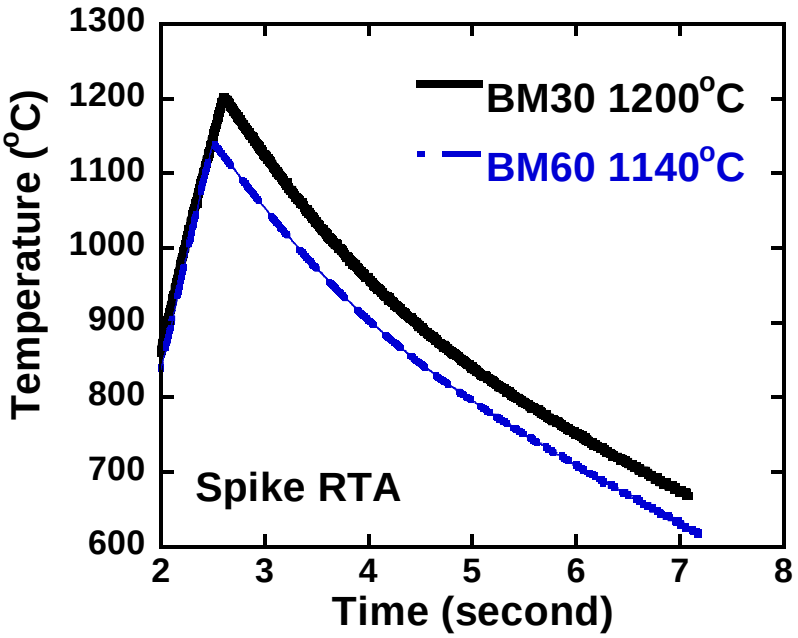

Figure 4.12 Temperature vs. time profiles of the spike RTA experiments of this work.

The temperature profiles of the spike RTAs are shown in Figure 4.12. The RTA temperature ramped up quickly at a rate of 560 °C/second to the set peak temperature, and then ramped down with a rate of 100 °C/second. Unlike isothermal anneals such as furnace anneals and soak RTAs, the temperature profiles of spike RTAs change very rapidly with time. The overall thermal budget cannot be approximated using the peak temperature and the hold time at the peak temperature, which is needed for the HRXRD based interdiffusivity measurement described in Equation 4.1 and the Boltzmann-Matano method. These two methods extract Si-Ge interdiffusivity as a function of Ge fraction at a certain temperature. Based on the derivation in Section 4.2, Si-Ge interdiffusivity strongly depends on both temperature and Ge fraction. It is difficult to measure the diffusivity experimentally for an anneal with changing temperatures such as soak RTAs. When the annealing temperature changes very fast, the extracted interdiffusivity by the two methods above is just an effective interdiffusivity over the large temperature range, which depends on the ramp rates as well.

Our self-diffusivity based model provides a third approach to interdiffusion studies. This approach is also based on the experimental data such as self-diffusivities, whose temperature dependences were well characterized. In the new model, the temperature impacts appear at two places, one is in the well-known Arrhenius expression of self-diffusivities, the other is in the factor$(1 + \partial ln\gamma / \partial lnx)$. Therefore, the new model is more accurate in describing the temperature impacts on Si-Ge interdiffusivity, especially under spike RTAs and other advanced non-isothermal anneal techniques. As seen in Figure 4.13, the prediction by the model shows great agreement with the spike annealed SIMS data for BM30. For BM60 annealed with a spike RTA (shown in Figure 4.14), due to the dislocation mediated interdiffusion, the diffusion at the low Ge fraction tail region is more than the model prediction.

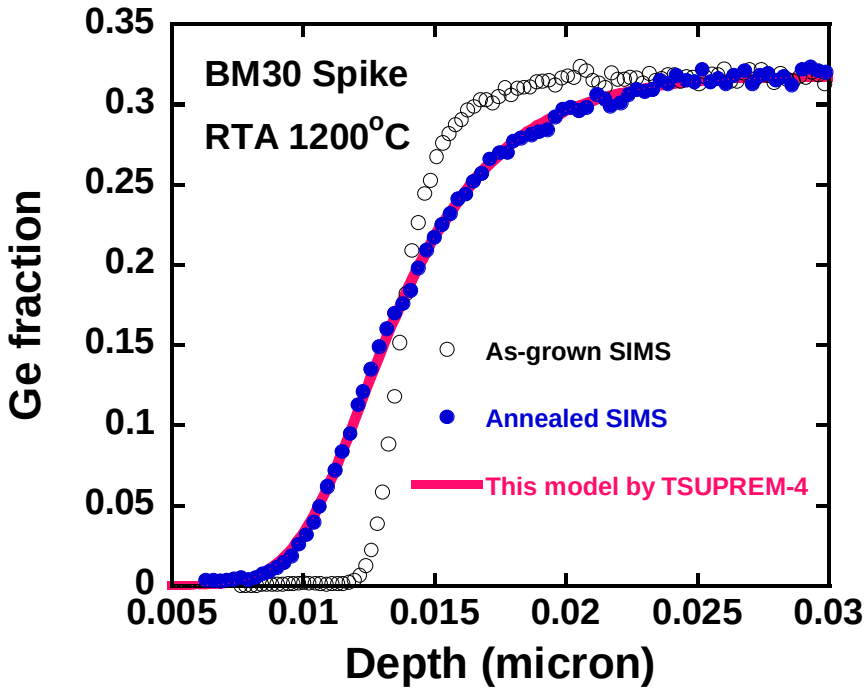

Figure 4.13 As-grown, annealed Ge SIMS profiles of a strained-Si/relaxed $Si_{0.3}Ge_{0.3}$ structure and this model prediction simulated by TSUPREM-4™. The spike RTA has a peak temperature of 1200 °C.

Overall, by comparison with the experimental data under furnace anneals, soak RTAs and spike RTAs, the new model demonstrates a good accuracy, wide applicable temperature and Ge fraction ranges. At x_{Ge} = 0 end, the valid temperature range of the model is from as low as 880 °C to as high as 1270 °C. According to the solidus line in SiGe phase diagram [35], as Ge fraction increases, the melting point of $Si_{1-x}Ge_x$ decreases, so the maximum of the anneal temperature decreases as well. On the other hand, the new model does not include the dislocation contribution to interdiffusion, because the original data of Si and Ge self-diffusivities were obtained from low dislocation density samples (TDD~10^5 cm^{-2}). At the high Ge fraction end where the through-dislocation diffusion is negligible, the new model agrees with Gavelle's experimental results.

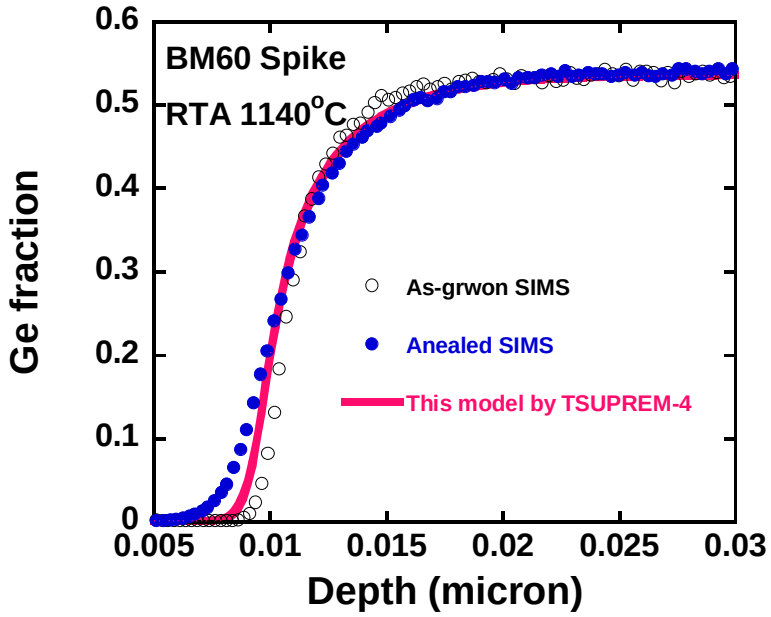

Figure 4.14 As-grown, annealed Ge SIMS profiles of a strained-Si/relaxed $Si_{0.45}Ge_{0.55}$ structure and this model prediction simulated by TSUPREM-4™. The spike RTA has a peak temperature of 1140 °C.

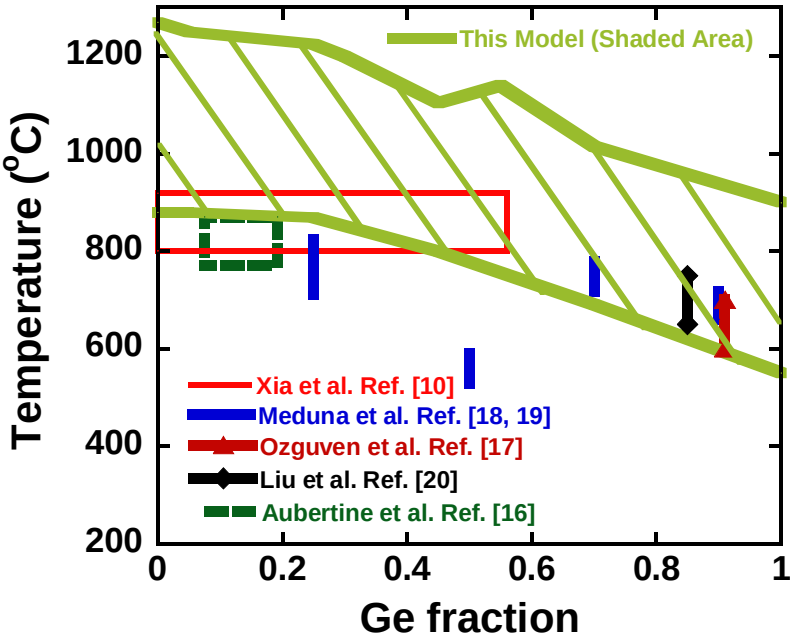

Figure 4.15 Experimental Si-Ge interdiffusion temperature ranges or Si-Ge interdiffusion model applicable ranges in literature work in comparison with that of this work.

4.4 Chapter summary

Based on the correlation between self-diffusivity, intrinsic diffusivity and interdiffusivity in binary alloy systems, an interdiffusivity model was quantitatively derived for Si-Ge interdiffusion with zero strain and tensile strain based on diffusion laws and experimental data. This new model unifies previous interdiffusivity models and shows good accuracy over the full Ge fraction range. To demonstrate its validity for conventional and advanced anneal techniques, interdiffusion experiments were conducted under soak RTAs and spike RTAs. Simulation predictions by the new model were compared with the SIMS data under furnace anneals, soak RTA and spike RTA conditions. The new model presents good agreement with experimental data, and is applicable in a wide temperature range up to 1270 °C at x_{Ge} =0 end and to 900 °C at x_{Ge}= 1 end for all the three anneal types, as shown in Figure 4.15. With wide applicable temperature and Ge fraction ranges, the new model can be applied to the designs of structure, epitaxial growth

and process condition for various SiGe devices. In addition, our interdiffusivity model for Si-Ge interdiffusion provides a zero strain, no dopant effect and low dislocation density reference for the following chapters on the impact of compressive strain on Si-Ge interdiffusion and future studies on doping and dislocation impacts.

Chapter 5 Impact of Compressive Strain on Si-Ge Interdiffusion

5.1 Introduction and background

Previous studies showed that Si-Ge interdiffusivity increases exponentially with Ge fraction and compressive strain, and also increases with certain dopants and implant damages [10, 11, 79]. Based on the model in Chapter 4, the interdiffusivity at the Ge end is at least four orders of magnitude larger than that at the Si end [48]. As higher Ge fraction and larger compressive strain are applied in SiGe heterostructures, interdiffusion becomes more and more problematic. It is expected that the diffusion length $\sqrt{Dt}$ will become comparable to the thickness of SiGe layers in the near future. Therefore, for the design and optimization of SiGe structures and thermal budgets for the future devices, it is very important to get a better understanding of Si-Ge interdiffusion under compressive strain in the higher Ge fraction range.

The impact of compressive strain on Si-Ge interdiffusion is an interesting topic. For epitaxial SiGe heterostructures, significant stress gradients exist on top of the Ge concentration gradients. Is the stress gradient another driving force for interdiffusion? Does the stress influence the activation energy and the pre-factor of interdiffusivity? Is the impact really from stress or from defects? Quantitatively, what is the magnitude of the impact and how can it be modeled?

5.2 Literature review on this topic

Many groups have studied this topic, but have made different observations or conclusions. Iyer and LeGoues (1989) first reported strain enhanced interdiffusion in SiGe system [129]. Prokes *et al* (1992) demonstrated an enhanced interdiffusion in a symmetrically strained $Si_{1-x}Ge_x$/Si superlattice compared with in an asymmetrically strained case [132]. Cowern *et al* (1994)

showed a linear dependence of activation energy on strain, and Si-Ge interdiffusion was enhanced by compressive strain [67]. Theiss *et al* (1995) demonstrated interdiffusion was enhanced in amorphous Si/Ge multi-layers under hydrostatic pressure similar to that under internal mismatch strain [140].

However, there were some studies which suggested that strain has insignificant impact on the intermixing behaviours in these SiGe structures. Holländer *et al* (1992) reported no change in the activation energy for interdiffusion in strained $Si_{1-x}Ge_x$/Si superlattices, and the enhancement of the diffusion coefficient pre-factor was due to the increased Ge fraction, but not strain [89]. Gillin and Dunstan (1994) further showed strain-enhanced diffusion was not expected to be a significant effect in the tetrahedral semiconductors like SiGe and GaAs systems [141]. Furthermore, Baribeau (1998) studied Si-Ge interdiffusion by X-ray reflectivity (XRR) and X-ray diffraction (XRD), and ascribed the diffusion enhancement to grown-in non-equilibrium point defects instead of strain [131]. The inconsistent results can be probably ascribed to the strong concentration dependence of the activation energy, which makes it hard to separate the strain impact from the concentration impact. In the past decade, two important studies done by Aubertine *et al* [15, 16] and Xia *et al* [10, 11] confirmed that strain has a significant impact on Si-Ge interdiffusion. Using Ge self-diffusivity as the reference line, Aubertine *et al* separated strain and Ge concentration effects on Si-Ge interdiffusion by HRXRD measurements. Xia *et al* obtained the Si-Ge interdiffusivity with the Boltzmann-Matano method under a relaxed condition, and then modeled the impact of compressive strain as an exponential factor without temperature dependence.

So far, the questions mentioned above have not been answered well. Also, the available studies on this topic are for Ge molar fraction (x_{Ge}) ranging from 0 to 0.56. There is little information on the role of strain in Si-Ge interdiffusion for x_{Ge} > 0.56. In this chapter, strain enhanced

interdiffusion was investigated in the range 0.36 < x_{Ge}< 0.75 by experiments, thermodynamics and modeling, and some new light was shed on this topic.

5.3 Experiments

5.3.1 Epitaxial structure growth and thermal anneals

A multi-layered pseudomorphic structure was used for this study: $Si_{1-x}Ge_x/Si_{1-y}Ge_y/Si_{1-x}Ge_x$ ($y > x$), as is shown in Figure 5.1. The $Si_{1-y}Ge_y$ layer is under biaxial compressive strain. Two sets of (x, y) were designed: (0.40, 0.65) and (0.50, 0.75), labeled as S4065 and S5075, as described in Chapter 3.

All the samples were grown on 6 inch (100) Czochralski (CZ) p-type Si wafers in an Applied Materials "Epi Centura" system. A 1 μm relaxed $Si_{1-x}Ge_x$ layer was grown on a graded buffer layer at 900 °C. Next a thin compressively strained$Si_{1-y}Ge_y$ layer was grown. For y=0.65, the growth temperature was 525°C; for y=0.75, the growth temperature was 450°C. On top of the compressively strained layer, another relaxed $Si_{1-x}Ge_x$ was grown at 525 °C. Finally, a thin silicon cap was grown on top at 600 °C. The nominal thicknesses of the top strained Si, relaxed $Si_{1-x}Ge_x$ and compressive $Si_{1-y}Ge_y$ layers are 6 nm, 30 nm and 12 nm separately. The sample structure and the schematic profile of Ge fraction are shown in Figure 5.1 (a) and (b).

Inert anneals were performed in nitrogen ambient using a tube furnace and an enclosed Linkam TS1200 high temperature heating stage. The temperature ranged from 720 °C to 880 °C, and the anneal time was 40 minutes for all the anneals. The thermal budgets during the temperature ramp up and ramp down processes were found to be negligible by simulations using the model established in this work (see Appendix B).

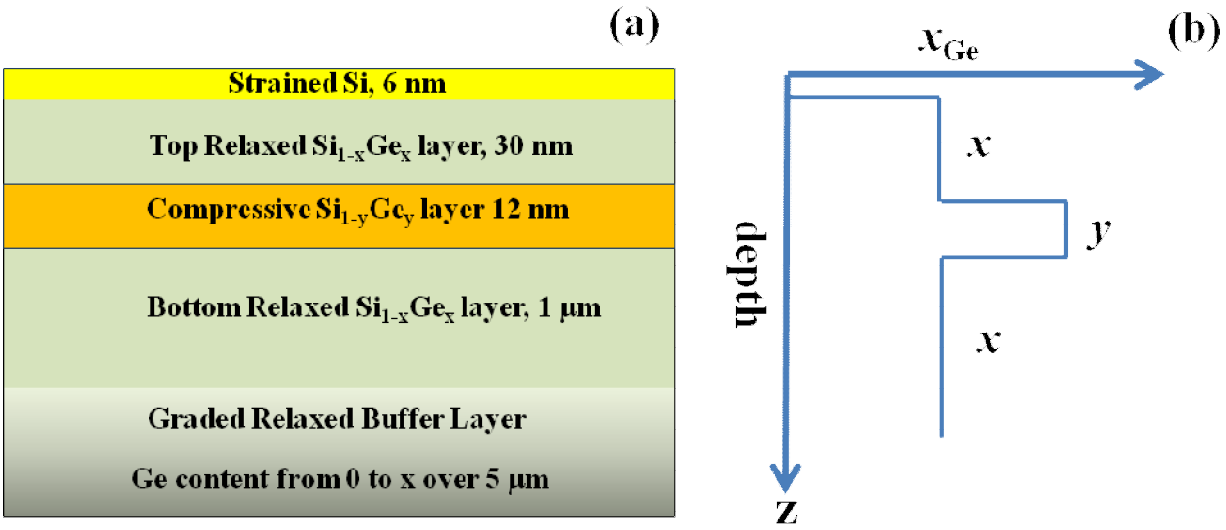

Figure 5.1 (a) Sample structure, and (b) the schematic depth profile of Ge fraction.

5.3.2 Characterization of strain and Ge fraction, and threading dislocation

X-ray diffraction (XRD) measurements were used to measure biaxial compressive strain in the as-grown and annealed samples. All the measurements were performed using a PANalytical X'Pert PRO MRD with a triple axis configuration. Symmetric (004 Bragg reflection) and asymmetric (115 Bragg reflection) scans were performed to obtain both the in-plane and out-of-plane lattice constants of the compressive $Si_{1-y}Ge_y$ and bottom relaxed $Si_{1-x}Ge_x$ layers. This allows us to determine both the Ge fraction and strain in these layers. To eliminate the influence of the substrate wafer miscut and the tilt of the epitaxial films, XRD scans were performed with the wafer oriented at phi=0° and 180° for both symmetric and asymmetric reflections [110, 111], where "phi" denotes the angle rotation of the sample about its surface normal. The Ge fraction and strain of the $Si_{1-y}Ge_y$ and bottom relaxed $Si_{1-x}Ge_x$ layers were extracted by matching the average peak separation between the layer peak and the substrate peak with the peak separation of 004 and 115 scans simulated with the PANalytical Epitaxy software package (see Appendix C). The thickness of the $Si_{1-y}Ge_y$ layer used for those simulations is its FWHM (full width at half maximum) in SIMS profiles. Moreover, 115 reciprocal space mappings were done

to further confirm the strain status for S4065 and S5075 with the highest thermal budgets shown in Figure 5.3.

Raman spectroscopy was employed to obtain the Ge fraction and strain in the top two layers. The setup of Raman measurements was well described in Chapter 3. The Ge profiles of the top four layers were characterized by SIMS measurements.

The etch pit density (EPD) technique was employed to measure the threading dislocation density (TDD) for the as-grown and annealed samples of S4065 and S5075. Each sample was etched with a modified Schimmel solution for 60 seconds. The modified Schimmel solution consisted of 55 Vol% CrO_3 (0.30M) and 45 Vol% HF (49%) [127]. The concentration of CrO_3 used in this work is lower than that (0.40M) in Ref. [127] to obtain a slower etch rate. Based on the etch rates over the full Ge fraction range in Ref. [127], the etch depth for S4065 and S5075 was less than 200 nm. After etching, five different positions on the surface of each sample were checked with an optical microscope in the dark field mode.

5.3.3 Results and discussion of strain, Ge fraction and threading dislocation

It is well known that thermal treatments can cause the misfit dislocation density to increase and relax the compressive strain during anneals. To accurately study the compressive strain impact on interdiffusion, it is very important to monitor the strain status. Our anneal conditions were designed to avoid plastic strain relaxation and the complications in dealing with strain relaxation in this chapter. XRD and Raman spectroscopy were used in this work to measure the strain status before and after the anneals. On the other hand, the TDD was estimated with the EPD technique.

1) Ge fraction and strain analysis by HRXRD

XRD measurements were performed on the as-grown and annealed samples (please see Table 5.1 and Table 5.2 for the anneal conditions) for both S4065 and S5075. The 004 symmetric and 115 asymmetric XRD scans from S4065 are shown in Figure 5.2. The XRD signals from all the layers can be observed. The strongest peak is from Si substrate, and on the right of it, there is a broad bump, which is caused by the thin top Si cap. The second strongest peak is from the thick bottom $Si_{1-x}Ge_x$ layer, and on the left of it, there is a shoulder from the top $Si_{1-x}Ge_x$ layer, which indicates the Ge fraction is slightly different in the top and bottom $Si_{1-x}Ge_x$ layers. The peaks from the $Si_{1-y}Ge_y$ layers are relatively broad due to their small thicknesses. Using the Si substrate peak as a reference, we can see that the peaks from the $Si_{1-y}Ge_y$ layers shift to the right and become more intense and narrower after anneals. This indicates that the layer gets thicker and has a lower Ge fraction and strain after anneals, consistent with Si-Ge interdiffusion having occurred.

Furthermore, based on the accurate peak positions from 004 symmetric and 115 asymmetric scans at phi=0° and 180°, the Ge fraction and strain in the $Si_{1-y}Ge_y$ and bottom $Si_{1-x}Ge_x$ layers are extracted by simulations with the PANalytical Epitaxy software package, which are summarized in Table 5.1 and Table 5.2. From Table 5.1 and Table 5.2, the as-grown Ge fraction in these two layers is smaller than the target values in the design. From their relaxation factors, the bottom $Si_{1-x}Ge_x$ layers were not 100% relaxed, but slightly compressively strained. For a higher thermal budget, the strain in the bottom $Si_{1-x}Ge_x$ layers becomes smaller, indicating the $Si_{1-x}Ge_x$ layers approached full relaxation through dislocations after anneals. Meanwhile the relaxation R just increases slightly, which is caused by dislocation glide for further relaxation in the

GRB layers [73]. The compressive strain in the $Si_{1-y}Ge_y$ layers depends not only on interdiffusion but also on the relaxation in the lower $Si_{1-x}Ge_x$ layers during anneals. The negligible strain relaxation of the $Si_{1-y}Ge_y$ layer demonstrates that this layer remains pseudomorphic (or coherent) with the underlying $Si_{1-x}Ge_x$ layer. In Figure 5.3, based on the peak patterns in the 115 reciprocal space mapping, it is demonstrated that the compressive $Si_{1-y}Ge_y$ layers are still coherent with the bottom $Si_{1-x}Ge_x$ layers for S4065 and S5075 with the highest thermal budgets. Interestingly, the weak diffraction peaks from the top $Si_{1-x}Ge_x$ layers can also be seen, which strongly demonstrates the in-plane lattice constants of the top three layers are well aligned. Compared with the value of the strain calculated by the conventional method assuming a perfect pseudomorphic structure on a fully relaxed virtual substrate, $\varepsilon_{biaxial} \approx -0.0418 * (y - x)$, the measured compressive strain the $Si_{1-y}Ge_y$ layer is 3%~10% larger due to the incompletely relaxed bottom $Si_{1-x}Ge_x$ layers. This factor has been taken into account in the error bar of evaluating the strain impact on interdiffusion in Section 5.4.3.

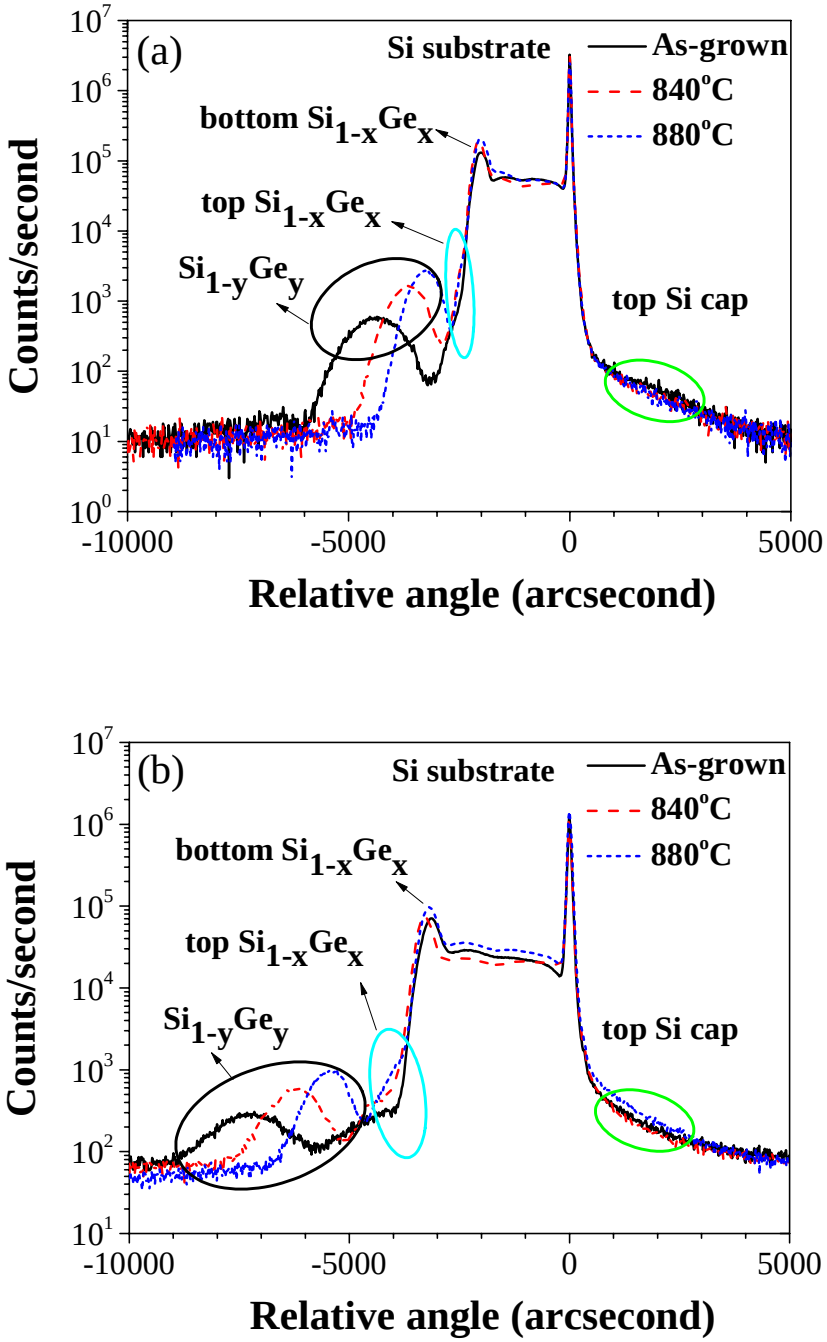

Figure 5.2 (a) 004 symmetric XRD and (b) 115 asymmetric scans at phi=180° from S4065 samples. The most intense narrow peak is from the Si substrate. The second strongest peak is from bottom $Si_{1-x}Ge_x$ layer and on the left of it there is a weak shoulder from the top $Si_{1-x}Ge_x$ layer. The broad peak on the far left is from the thin $Si_{1-y}Ge_y$ layer.

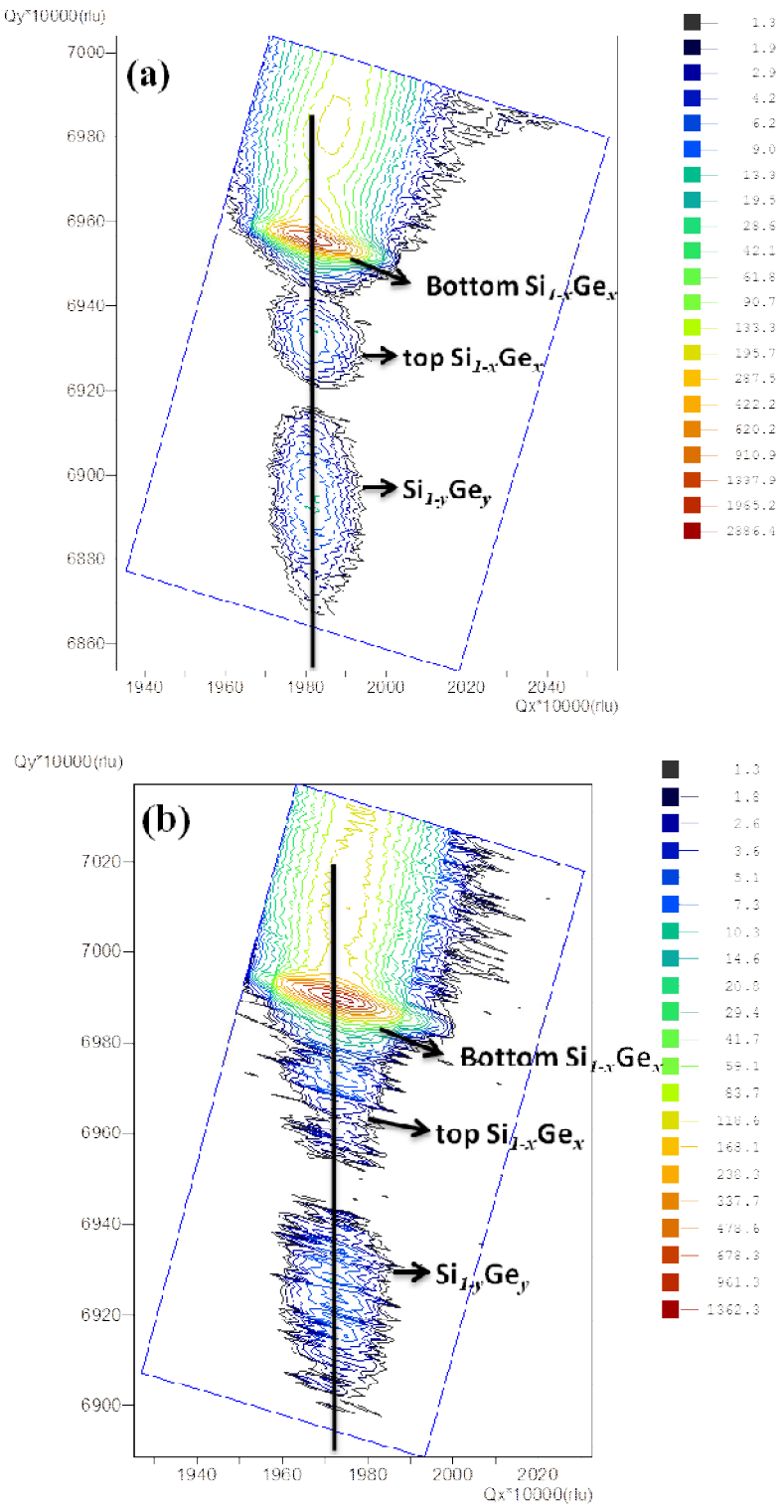

Figure 5.3 115 Reciprocal space mapping: (a) for S5075 annealed at 840 °C for 40 mins, (b) for S4065 annealed at 880 °C for 40 mins. Due to the weak diffraction peaks from the $Si_{1-y}Ge_y$ layers, the strong diffraction peaks from Si substrate were not shown for better color contrast.

Table 5.1 Ge fraction, strain relaxation R and strain ε in the compressive $Si_{1-y}Ge_y$ layers from XRD measurements. $-0.0418(y-x)$ is the empirical formula to calculate strain in pseudomorphic SiGe structures. The error bars of Ge fraction, relaxation R and strain are ±0.01, ±2 and ±0.4×10^{-3} respectively.

Sample	Thermal budget	Compressive $Si_{1-y}Ge_y$ layer			
		y	R (%)	ε	$-0.0418(y-x)$
S5075	As-grown	0.73	0	-12.8×10^{-3}	-11.9×10^{-3}
	760°C	0.65	3	-9.4×10^{-3}	-8.5×10^{-3}
	840°C	0.60	3	-6.0×10^{-3}	-5.6×10^{-3}
S4065	As-grown	0.62	0	-12.0×10^{-3}	-11.0×10^{-3}
	840°C	0.54	2	-7.5×10^{-3}	-7.2×10^{-3}
	880°C	0.52	3	-5.9×10^{-3}	-5.9×10^{-3}

Table 5.2 Ge fraction, strain relaxation R and strain ε in the bottom $Si_{1-x}Ge_x$ layers from XRD measurements. The error bars of Ge fraction, relaxation R and strain are ±0.005, ±0.5 and ±0.1×10^{-3} respectively.

Sample	Thermal budget	Bottom Relaxed $Si_{1-x}Ge_x$ layer		
		x	R (%)	ε
S5075	As-grown	0.445	92.5	-1.3×10^{-3}
	760°C	0.446	92.5	-1.3×10^{-3}
	840°C	0.468	96.4	-0.6×10^{-3}
S4065	As-grown	0.359	90.0	-1.4×10^{-3}
	840°C	0.368	95.0	-0.7×10^{-3}
	880°C	0.373	97.8	-0.3×10^{-3}

2) Ge fraction and strain analysis with Raman spectroscopy

The XRD signals from the top silicon caps and top $Si_{1-x}Ge_x$ layers are not clearly visible in Figure 5.2, so their strain status could not be obtained. Therefore, the top two layers were further characterized by Raman spectroscopy. Raman spectra from the as-grown and annealed samples of S5075 and S4065 are shown in Figure 5.4. There is almost no obvious shift for both S5075 and S4065. The Ge fraction and strain information are quantitatively obtained from the correlation equations between the Raman peak positions and Ge fraction and strain shown in Equation 5.1~5.3 [88]. For Si rich SiGe, the Si-Si and Si-Ge peaks are normally used for calculation with better accuracy. The calculated data are shown in Table 5.3. From Table 5.3, we can see the top silicon layers are still under significant tensile strain after anneals. The top $Si_{1-x}Ge_x$ layers are slightly compressively strained, which can be ascribed to their slightly larger Ge fraction compared with that of the bottom $Si_{1-x}Ge_x$ layers. This is also consistent with the XRD measurements, where there are shoulder peaks at the left side of the peaks from the bottom $Si_{1-x}Ge_x$ layers.

$$\omega_{Si-Si} = 520 - 70.5x_{Ge} - 830\varepsilon \quad (5.1)$$

$$\omega_{Si-Ge} = 400.5 + 16x_{Ge} - 575\varepsilon \quad (5.2)$$

$$\omega_{Ge-Ge} = 282.5 + 16x_{Ge} - 384\varepsilon \quad (5.3)$$

Table 5.3 Ge fraction and strain in the top two layers, Si layer under tensile strain and the compressively strained top $Si_{1-x}Ge_x$ layer, from Raman measurements. The error bars of Ge fraction and strain are ±0.01 and ±1.0×10^{-3} respectively. x' denotes the Ge fraction in the top $Si_{1-x}Ge_x$ layer.

Sample	Anneal conditions	Top $Si_{1-x}Ge_x$ layer		Top Si
		x'	ε	ε
S5075	As-grown	0.45	-0.8×10^{-3}	17.8×10^{-3}
	720°C, 40 mins	0.46	-1.1×10^{-3}	18.1×10^{-3}
	760°C, 40 mins	0.45	-0.8×10^{-3}	17.5×10^{-3}
	800°C, 40 mins	0.45	-1.3×10^{-3}	17.8×10^{-3}
	840°C, 40 mins	0.46	-0.7×10^{-3}	18.4×10^{-3}
S4065	As-grown	0.36	-0.9×10^{-3}	14.5×10^{-3}
	760°C, 40 mins	0.38	-2.0×10^{-3}	14.9×10^{-3}
	800°C, 40 mins	0.37	-1.6×10^{-3}	14.9×10^{-3}
	840°C, 40 mins	0.37	-2.5×10^{-3}	14.9×10^{-3}
	880°C, 40 mins	0.38	-2.9×10^{-3}	15.0×10^{-3}

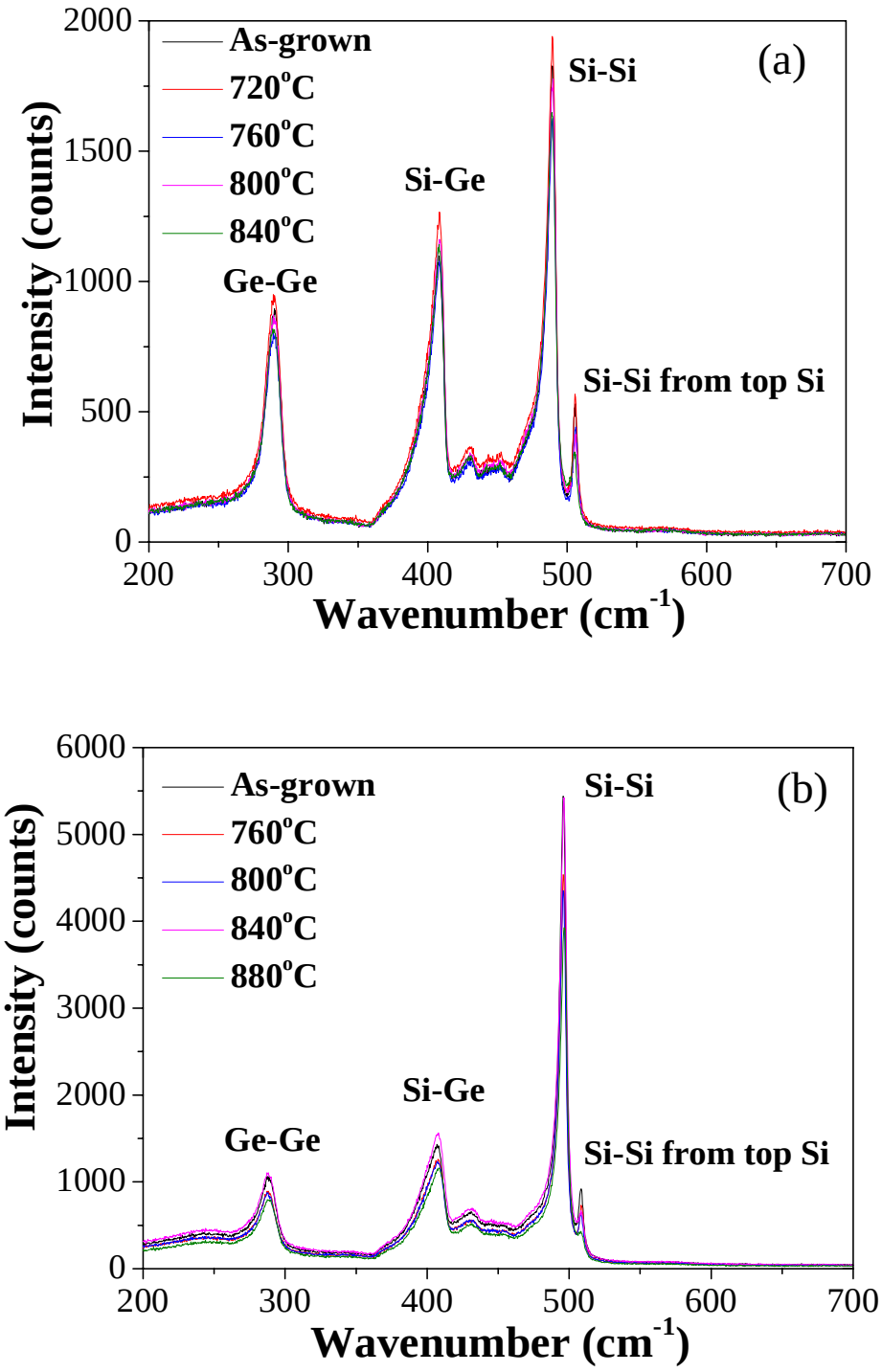

Figure 5.4 Raman spectra: (a) for S5075; (b) for S4065. The three strong peaks are from top $Si_{1-x}Ge_x$ layers. The right small peak is from the top silicon layer, which is under tensile strain.

3) Ge depth profiling from SIMS analysis

The Ge profiles of the $Si_{1-y}Ge_y$ layers in the as-grown and annealed samples of S5075 and S4065 were measured by SIMS, as shown in Figure 5.5. The Ge peak fraction decreases with a higher anneal temperature. The Ge fractions of all the three SiGe layers are consistent with those obtained from the XRD and Raman data within measurement errors. In Figure 5.5, the Ge fraction on the left side of the peak is a little higher than that on the right side by about 1.5 at.%. As mentioned earlier, this explains the small compressive strain in the top $Si_{1-x}Ge_x$ layers measured in the Raman spectra, and the shoulder peak close to the peak from the thick bottom $Si_{1-x}Ge_x$ layers in the XRD measurements.

4) TDD measurements by the EPD technique

Typical dark field images of the preferentially etched surfaces of S4065 and S5075 are shown in Figure 5.6. Based on the EPD measurements, the TDD values in the interested layers of all the four samples are in the order of magnitude of 10^5 cm^{-2} ($1\sim5\times10^5$ cm^{-2}). It was shown that the TDD as high as $10^7/cm^2$ has little impact on the interdiffusion at the higher Ge fraction range in ref. [10]. Therefore, the impact of dislocations on interdiffusion can be reasonably ignored in this study.

In summary, combining the XRD, Raman and SIMS data, it was confirmed that during interdiffusion steps where Ge fraction peaks dropped, the diffused compressive $Si_{1-y}Ge_y$ layers were still pseudomorphic (coherent) with the underlying relaxed $Si_{1-x}Ge_x$ layers. Within experimental accuracy, no plastic strain relaxation in the compressive $Si_{1-y}Ge_y$ layers by misfit dislocations was observed for the thermal budgets used in this work. The measured TDD by the EPD technique was about 10^5 cm^{-2}, so its impact on interdiffusion is negligible.

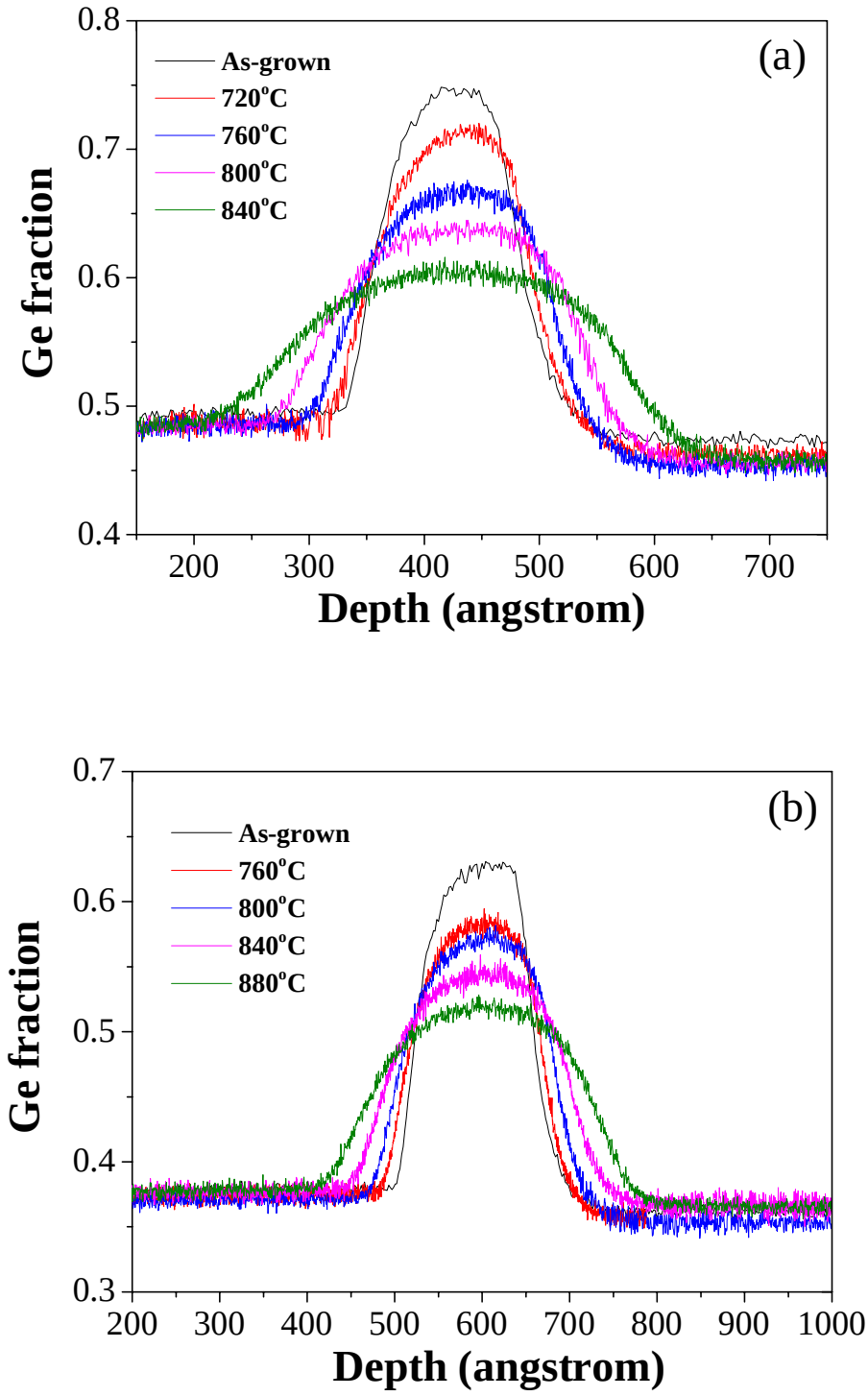

Figure 5.5 Ge profiles measured by SIMS for as-grown and annealed samples: (a) for S5075; (b) for S4065. The anneal time is 40 mins for all anneals.

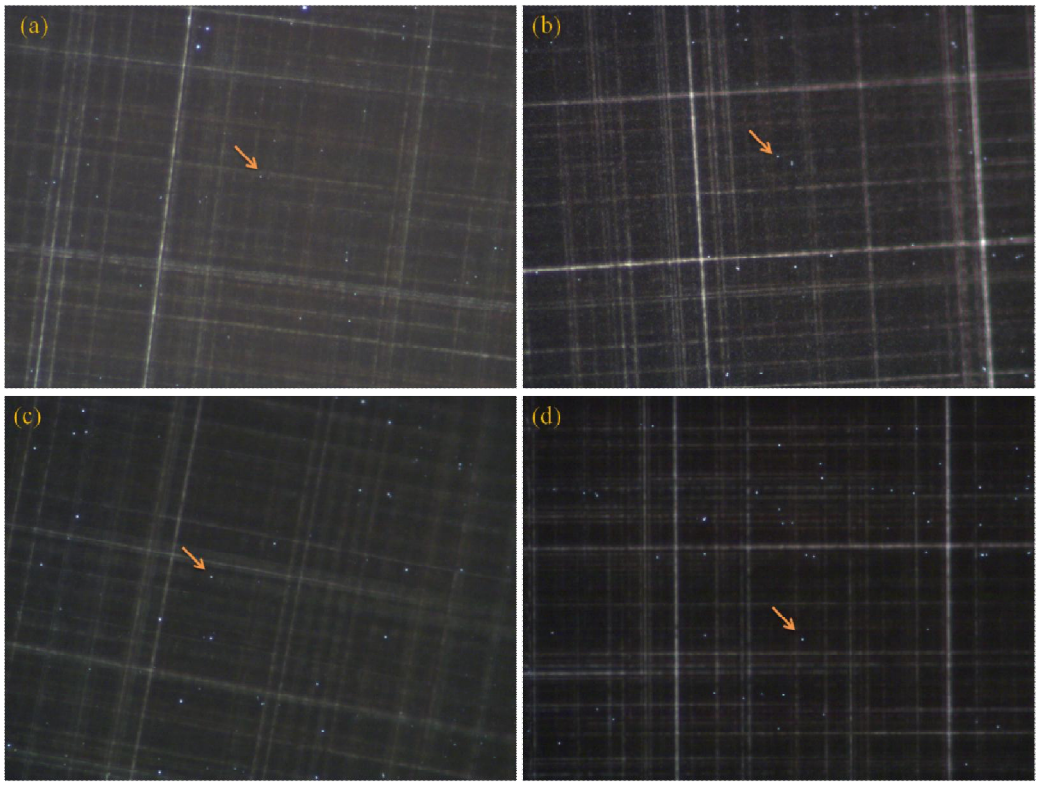

Figure 5.6 Dark field images (140 *μm*×160 *μm* for each image) of preferentially etched surfaces with modified Schimmel solution: (a) As grown sample of S4065; (b) As grown sample of S5075; (c) Annealed sample (880 °C) of S4065; (d) Annealed sample (840 °C) of S5075. The small white spots in the image are the etch pits, as highlighted by the arrows.

5.4 Impact of compressive strain on Si-Ge interdiffusion

5.4.1 The role of strain in Si-Ge interdiffusion

The common uses of SiGe layers are for strain and bandgap engineering. However, strain can also influence many aspects of mass transport behaviours, such as dopant diffusion, self-diffusion, interdiffusion and dopant segregation in SiGe materials. For Si-Ge interdiffusion, strain plays two major roles: (a) thermodynamically, the elastic strain energy contributes to the interdiffusion driving force. With the Cahn-Hilliard approach [43, 142], the contribution of the

strain energy can be modeled as an increase in the prefactor of the apparent diffusivity as discussed below; (b) Microscopically, strain can influence the diffusion kinetics through the energy barrier for atom movements. This strain effect is reflected by the change of the activation energy and pre-factor of Si-Ge interdiffusivity, which can be combined and modeled using one q' factor as discussed below.

According to Fick's first law $J = -D\frac{\partial C}{\partial z}$, diffusion is driven by concentration gradients. However, strictly speaking, diffusion is driven by the chemical potential gradient. In order to estimate the contribution of the strain energy to the driving force in the strained multilayered SiGe structure studied in this chapter, we present here an analysis of the interdiffusion under a steep concentration gradient, following the method that Cahn and Hilliard used in their work [43, 142]. In 1958, Cahn and Hilliard proved that there is an extra free energy term caused by a steep concentration gradient, called the "chemical gradient energy" [142], which contributes to the driving force of interdiffusion [43]. For metal superlattices with short modulation periods, this effect plays a significant role in spinodal decompositions at relatively low temperatures [43]. However, for SiGe system, the contribution of this effect to the interdiffusion is less than 0.1% of that of the common free energy term of chemical mixing [133], so it is negligible for our samples in this work. Furthermore, besides the chemical gradient energy term, there is an "elastic gradient energy G_{eg}" effect pointed out by Cook and de Fontaine in 1971, but this effect is also negligible when the linear expansion coefficient η is less than 0.10 (for Si and Ge, η is 0.0418) [143] and can be ignored for our SiGe samples. Therefore, we just need to consider the common free energy term of chemical mixing and the biaxial strain energy caused by lattice mismatch.

Let's focus attention on the compositional variations in one dimension. It is assumed that the SiGe solid solution is incompressible and of constant molar volume as Cahn did for a binary

solid solution in his work [43]. If the SiGe solution is not homogeneous in the z direction (the direction normal to the wafer surface), the local Helmholtz free energy will be a function of z. As derived by Cahn [43], the total Helmholtz free energy F of the system would be given by

$$F = A \int [f_0(x_{Ge}) + Y_{UVW}\varepsilon^2]\, dz \qquad 5.4$$

where A is the cross-section area normal to the z axis; $f_0(x_{Ge})$ is the Helmholtz free energy per unit volume of the homogeneous solution at the Ge atomic fraction of x_{Ge}; Y_{UVW} is the biaxial modulus, which equals to $E/(1-\upsilon)$, where E is Young's modulus, and υ is Poisson ratio. For our samples, $< UVW >$ is <100>, and ε is the biaxial mismatch strain.

For the epitaxial SiGe structure in this chapter, the biaxial mismatch strain is empirically expressed as

$$\varepsilon = -\eta(x_{Ge} - x_0) \qquad 5.5$$

where η is the linear expansion per unit composition change (for Si and Ge, η is 0.0418), and x_0 is the Ge atomic fraction in the virtual substrate (for S4065 and S5075, x_0 is the Ge fraction of the bottom relaxed $Si_{1-x}Ge_x$ layer).

Combining Equation 5.4 and 5.5, the total free energy F can be expressed as

$$F = A \int [f_0(x_{Ge}) + \eta^2 Y_{UVW}(x_{Ge} - x_0)^2]\, dz \qquad 5.6$$

In the presence of a concentration gradient, if there is a local change in composition, the Helmholtz free energy F will also change, correspondingly, the local energy gradient will change. The derivative of F with respect to x_{Ge} is $\partial f_0/\partial x_{Ge}$ and it is proportional to the difference of the chemical potentials of Si and Ge in the solution. So for a variation in composition δx_{Ge},

$$\delta F = A \int [f_0' + 2\eta^2 Y_{UVW}(x_{Ge} - x_0)]\delta x_{Ge}\, dz \qquad 5.7$$

where $f_0' = \partial f_0/\partial x_{Ge}$.

The term in the square bracket is the change in free energy due to a local change in composition δx_{Ge}. Based on the conventional equation of flux, $flux = mobility * force = -mobility * energy\ gradient$, the diffusion of Ge atoms is given by

$$J = -M\frac{d}{dz}[f_0' + 2\eta^2 Y_{UVW}(x_{Ge} - x_0)] \quad 5.8$$

Then this equation can be expressed as

$$J = -Mf_0''\left(1 + \frac{2\eta^2 Y_{UVW}}{f_0''}\right)\frac{dx_{Ge}}{dz} = -\widetilde{D}^{strained}\left(1 + \frac{2\eta^2 Y_{UVW}}{f_0''}\right)\frac{dx_{Ge}}{dz} \quad 5.9$$

where M is the mobility and $f_0'' = \frac{\partial^2 f_0}{\partial x_{Ge}^2}$; $\widetilde{D}^{strained} = Mf_0''$, which is the interdiffusivity under biaxial strain and only reflects the impact of the biaxial strain on the interdiffusivity itself without the driving force impact.

In the right parentheses of Equation 5.9, "1" reflects the contribution from chemical mixing, and the second term $\frac{2\eta^2 Y_{UVW}}{f_0''}$ reflects the magnitude of the biaxial strain energy contribution to the driving force, which is dependent on x_{Ge} and temperature. If $\frac{2\eta^2 Y_{UVW}}{f_0''}$ equals to zero, Equation 5.9 is back to the conventional Fick's first law for chemical diffusion.

Next, to calculate the value of $\frac{2\eta^2 Y_{UVW}}{f_0''}$, we need to know the expression of f_0. For better accuracy, instead of the simplest ideal solution model, we employ the regular solution model to calculate f_0 as Greer and Spaepen did [144]. In a SiGe binary solution, each atom has z (z = 4) nearest neighbors. The bond energy between two Si atoms is e_{SS}, between two Ge atoms e_{GG}, and between a Si and a Ge atom e_{SG}. Then given a random distribution of atoms on the lattice sites, the internal energy of a system of N lattice sites is $\frac{1}{2}Nz[x_{Ge}^2 e_{GG} + (1 - x_{Ge})^2 e_{SS} + 2x_{Ge}(1 - x_{Ge})e_{SG}]$. The internal energy of the pure components is $\frac{1}{2}Nz[x_{Ge}e_{GG} + (1 - x_{Ge})e_{SS}]$, so that the change in internal energy (≈enthalpy, for an incompressible condensed system) on mixing is given by

$$\Delta U = Nzx_{Ge}(1 - x_{Ge})\Delta e \quad (5.10)$$

where $\Delta e = e_{SG} - \frac{1}{2}(e_{GG} + e_{SS})$. For a regular solution, Δe can be calculated by $\Delta e = \frac{\alpha}{zN_a}$, where α is the interaction factor for the SiGe system and N_a is Avogadro constant [39].

The configurational entropy of mixing in a system of N atoms is

$$\Delta S = -kN[x_{Ge} ln x_{Ge} + (1 - x_{Ge}) ln(1 - x_{Ge})] \quad (5.11)$$

where k is Boltzmann's constant.

The change in Helmholtz free energy is given by

$$\Delta F = \Delta U - T\Delta S \quad (5.12)$$

Then

$$f_0 = \frac{\Delta F}{V} \quad (5.13)$$

where V is the volume of the system of N atoms.

Combining Equation 5.11-5.13, f_0'' can be expressed as

$$f_0'' = \frac{kT - 2zx_{Ge}(1 - x_{Ge})\Delta e}{x_{Ge}(1 - x_{Ge})\Omega} \quad (5.14)$$

where Ω is the atomic volume of $Si_{1-x}Ge_x$ alloys.

With Equation 5.9 and 5.14, we can estimate the term $\frac{2\eta^2 Y_{UVW}}{f_0''}$, the ratio of the contributions from the chemical mixing and strain energy. The Ge concentration dependence of this term is shown in Figure 5.7. For x_{Ge} = 0.5 at 1200 K, this term is as large as 0.3, so the strain contribution to the driving force should not be neglected. When x_{Ge} is close to 0 or 1 at high temperatures, this factor is smaller and can be ignored. For the ease of modeling, comparing Equation 5.9 to the classic expression of Fick's first law, we define an apparent diffusivity to include the biaxial strain energy contribution to the driving force.

The apparent interdiffusivity is defined as:

$$\widetilde{D}_{apparent} = \widetilde{D}^{strained}\left(1 + \frac{2\eta^2 Y_{UVW}}{f_0''}\right) \quad (5.15)$$

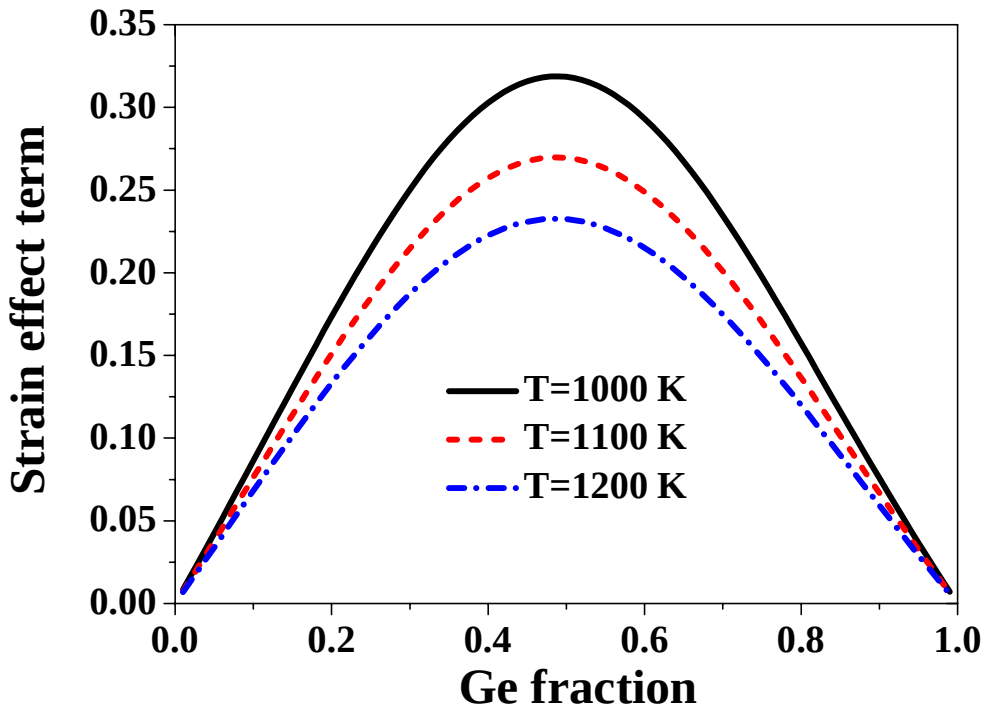

Figure 5.7 Ge concentration dependence of the strain effect term $\frac{2\eta^2 Y_{UVW}}{f_0''}$ at different temperatures: 1000 K, 1100 K and 1200 K.

On the other hand, strain can change $\widetilde{D}^{strained}$ itself. Conventionally, diffusivity is described by Arrhenius Equation as $D = D_0 e^{-E_a/kT}$, where D_0, E_a, k and T denote the prefactor, the activation energy, Boltzmann constant and the absolute temperature respectively. As is known, when strain is applied, the energy barriers of diffusion via point defects will change [145]. Accordingly, the prefactor D_0 and especially the activation energy E_a will change. Thus, $\widetilde{D}^{strained}$ reflects the changes in point defect kinetics caused by strain. The physical parameter that describes the effect of strain on the activation energy E_a is denoted as $Q' = \partial E_a / \partial \varepsilon$, the strain derivative of the activation energy E_a.

To the first order, the activation energy of diffusion in a biaxially strained media should be linearly proportional to the biaxial strain [15, 145]:

$$E_a^{strained} \infty Q^{'} \varepsilon_{biaxial} \quad 5.16$$

where $E_a^{strained}$ and $\varepsilon_{biaxial}$ denote the activation energy of interdiffusion with strain and the biaxial strain respectively.

5.4.2 Definition of the strain derivative $q^{'}$

As pointed out by Caliste *et al* in 2011, there are two main approaches to experimentally obtain $Q^{'}$ [146]. The first approach followed the definition of $Q^{'}$.

$$Q^{'} = \frac{\partial E_a}{\partial \varepsilon} = -\frac{\partial^2 lnD}{\partial \varepsilon \partial \beta} \quad 5.17$$

where $\beta = 1/kT$, assuming E_a independent of temperature.

To extract $Q^{'}$ from experimental data, this approach requires very accurate activation energies by fitting the diffusivity values in a constant strain field at different temperatures. The experimental setup of this approach is not readily available. Thus, in order to obtain the strain impact on diffusivity from experimental data, Cowern *et al* [67, 68] proposed to use a simplified version of Equation 5.17, called q', which is based on the measurements of diffusivities at a fixed temperature. For a given strained ($\varepsilon \neq 0$) condition and the relaxed ($\varepsilon = 0$) reference, q' can be expressed as Equation 5.18. Comparing these two approaches, Caliste *et al* found $Q^{'}$ and q' are connected with each other, $q^{'}(T) = Q^{'} - k\frac{\partial lnD_0}{\partial \varepsilon}T$ for small ε variations. This linear relationship indicates that q' includes both the effects of strain on the prefactor and activation energy of diffusivity.

$$q'(T) = -\left(\frac{kT}{\varepsilon}\right) \ln\left(\frac{\tilde{D}^{strained}}{\tilde{D}^{relax}}\right) \quad 5.18$$

Then $D^{strained}$ can be expressed as

$$\widetilde{D}^{strained} = \widetilde{D}^{relax} e^{\frac{-q'\varepsilon}{kT}} \quad 5.19$$

In previous studies, to our knowledge, only three groups gave the q' value of the compressive strain impact on Si-Ge interdiffusion. These q' values are summarized in Table 5.4. We can see that all the three previous studies focused on the range x_{Ge}< 0.56, and our work is the first one to extend this range to 0.75.

Table 5.4 Experimental values of the q' parameter in Si-Ge interdiffusion.

Reference	x_{Ge}	Maximum ε	Temp range (°C)	q' *(eV/unit strain)*
Cowern *et al*. [67]	0.25	-1.05%	900~1050	40±5
Cowern *et al*. [68]	0.3	-1.26%	875	17.8±4.3
Aubertine *et al*. [15]	0.17	-0.71%	795~895	19
Aubertine *et al*. [16]	0.075~0.192	-0.81%	770~870	10
Xia *et al*. [10]	0.30~0.56	-1.05%	770~920	27.6~36.3
This work	0.36~0.75	-1.20%	720~880	$-0.081T + 110$ (T in Kelvin)

5.4.3 Extraction and analysis of q' in this work

Following the approach proposed by Cowern *et al* [67, 68], we extracted q' from the SIMS profiles of our samples. First, combining Equation 5.15 and 5.19, the apparent interdiffusivity can be expressed as Equation 5.20. The interdiffusivity $\widetilde{D}^{relax}$ under full relaxation (no strain) acts as the reference, which plays a key role in determination of $'$. In Chapter 4, $\widetilde{D}^{relax}$ has been well established based on Si and Ge self diffusivities over the full Ge fraction range. Moreover, the dependence of the biaxial modulus Y_{UVW} on temperature and Ge concentration is also considered (see Appendix D). Y_{UVW} was calculated with the method used by Aziz *et al* [37]. Then the q' values were extracted by simulations with TSUPREM-4™ to solve Equation 5.21 of Fick's second law until a match was achieved with SIMS profiles after anneals. Small correction factors for the depth and concentration scales (mainly caused by the depth measurement uncertainty in SIMS analysis) were also included as parameters in the fitting process. The matched curves are shown in Figure 5.8.

$$\widetilde{D}_{apparent} = \left(1 + \frac{2\eta^2 Y_{UVW}}{f_0''}\right) \widetilde{D}^{relax} e^{\frac{-q'\varepsilon}{kT}} \qquad 5.20$$

$$\frac{\partial C_{Ge}}{\partial t} = \frac{\partial}{\partial z}\left(\widetilde{D}_{apparent} \frac{\partial C_{Ge}}{\partial z}\right) \qquad 5.21$$

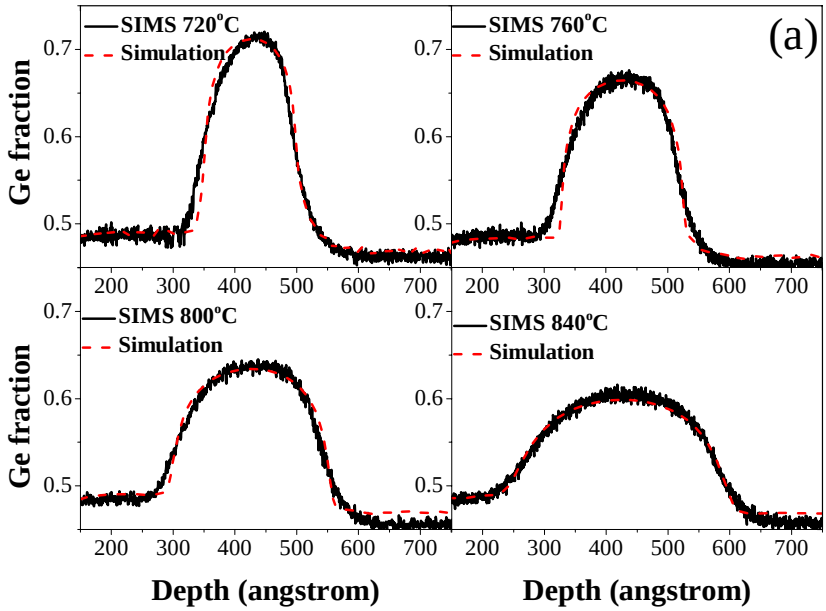

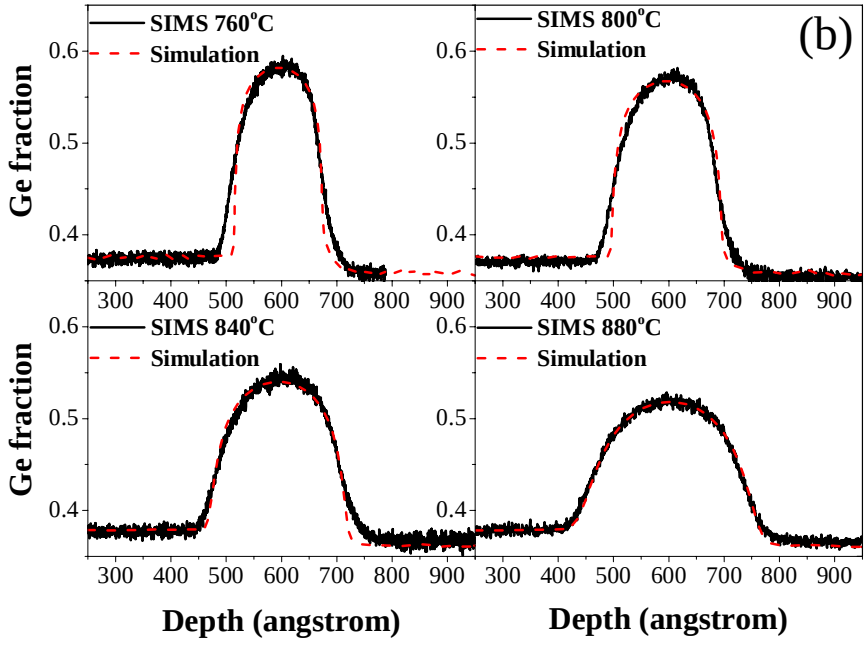

Figure 5.8 Simulation fitting to extract q' with TSUPREM-4™: (a) for S5075; (b) for S4065.

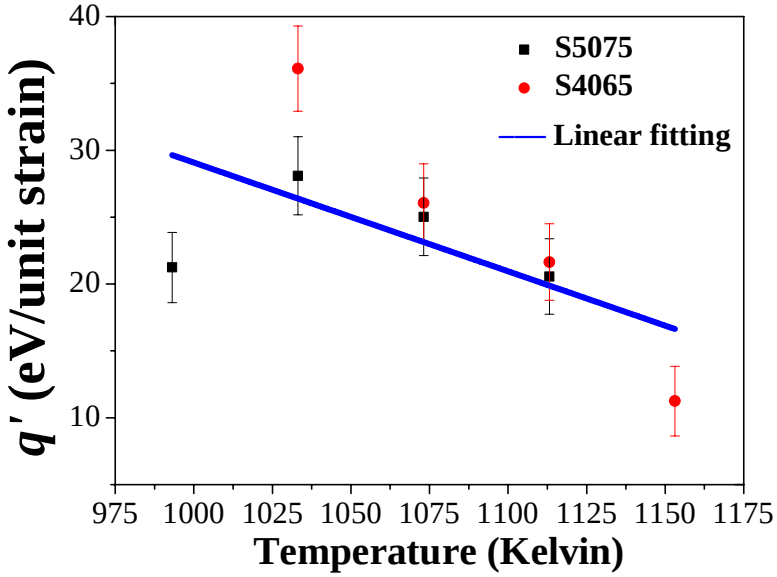

Figure 5.9 Extracted q' values and the linear fitting to q'.

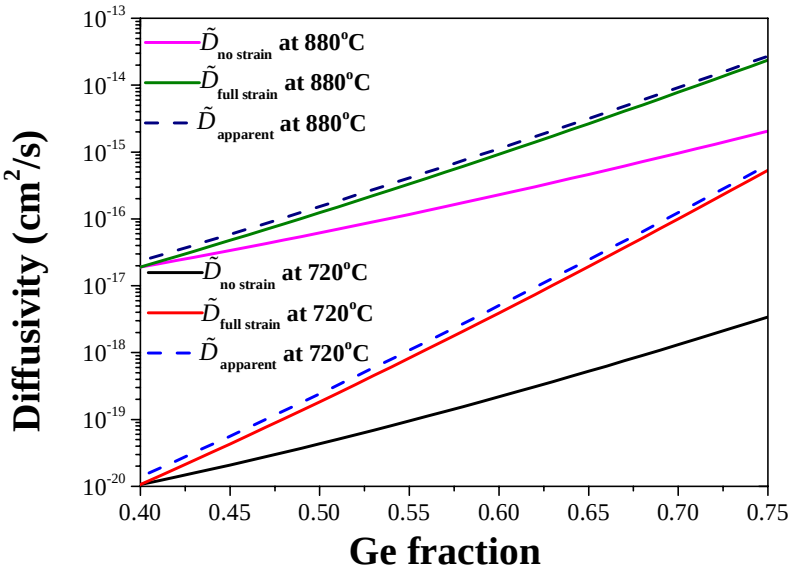

Figure 5.10 Comparison between the interdiffusivity ($\tilde{D}_{relax}$) without the strain impact, interdiffusivity ($\tilde{D}_{strained}$) only with the strain derivative q' impact and the apparent interdiffusivity ($\tilde{D}_{apparent}$) including both the impacts on the interdiffusivity and on the driving force for SiGe on a $Si_{0.60}Ge_{0.40}$ virtual substrate at 720 °C and 880 °C.

In Figure 5.9, all the extracted q' values are shown versus temperature. We can find that q' is in the range of tens of eV/unit strain. Interestingly, q' shows a certain temperature dependence in the temperature window (720 °C to 880 °C) that we used. As the temperature increases, q' shows a decreasing tendency for both S4065 and S5075. For S5075, the data point at 720 °C is lower than expected. In order to balance the measurement uncertainty in the experiments, a linear fit was done over all the data points, expressed as $q'(T) = (-aT + b)$ eV/unit strain, where a = 0.081 ± 0.041 eV/unit strain-K, b = 110 ± 44 eV/unit strain, and T is the absolute temperature in Kelvin. The fitting line reasonably falls in between the experimental data points. At the same anneal temperatures (760 °C, 800 °C and 840 °C), the q' values from S4065 and S5075 are very close, especially at 800 °C and 840 °C, which indicates a weaker dependence of q' on Ge concentration than on temperature. The q' obtained in this work is comparable to other q' values reported at the lower Ge fraction ranges in Table 5.4, and the order of magnitude of q' is same, tens of eV/unit strain. More q' data at different Ge fraction and temperature ranges are required to get a better understanding on the concentration dependence of q' over the full Ge fraction range.

In Figure 5.10, the interdiffusivity ($\widetilde{D}_{relax}$) without any strain impact, the interdiffusivity ($\widetilde{D}_{strained}$) only with the strain derivative q' and the apparent interdiffusivity ($\widetilde{D}_{apparent}$) including both the impacts on the interdiffusivity and on the driving force are compared for SiGe heterostructures on a $Si_{0.60}Ge_{0.40}$ virtual substrate such as a $Si_{0.25}Ge_{0.75}/Si_{0.60}Ge_{0.40}$ structure. We can see the interdiffusivity is enhanced by the biaxial compressive strain greatly, and the enhancement is dominated by the term $e^{\frac{-q'\varepsilon}{kT}}$. At x_{Ge}=0.75, where the maximum compressive strain exists, the enhancement factor is between one to two orders of magnitude. Compared with the impact of q', the enhancement factor from the strain-energy related driving force is around 0.3 for the medium Ge fraction range, as shown in Figure 5.7, which has a much smaller impact on Si-Ge

interdiffusivity. In addition, the enhancement caused by the biaxial compressive strain gets smaller at higher temperatures due to the decrease of 1/kT and a smaller q' at higher temperatures.

Based on the relationship of $Q^{'}$ and q', $q^{'}(T) = Q^{'} - k\frac{\partial lnD_0}{\partial \varepsilon}T$, q' is indeed dependent on temperature. When the temperature reaches 0 K, q' equals to $Q^{'}$. Based on the work of Zanzenberg *et al* [26], Caliste *et al* got a linear relationship $q^{'}(T) = -0.110T + 164$ for Ge self-diffusion in $Si_{0.9}Ge_{0.1}$ under biaxial compressive strain, which is very close to the Si-Ge interdiffusivity at this Ge fraction (x_{Ge} = 0.1). Compared with this linear relationship, our results show a smaller q' and a weaker temperature dependence. Before the physical definitions of $Q^{'}$ and q' were clarified by Caliste *et al*, q' for Si-Ge interdiffusion was regarded as $Q^{'}$ in previous studies. Therefore, there was no temperature dependence of q' reported for Si-Ge interdiffusion in previous studies. In 2002, using Ge self-diffusivity as the reference measured by Zangenberg *et al* [26], Aubertine *et al* extracted a constant q' value (19 eV/unit strain) by fitting scaled XRD satellite decay curves from SiGe superlattices [15]. The constant q' matched the XRD satellite decay curves well, which can probably be ascribed to the narrow temperature range they used. Later in 2005, Aubertine *et al* obtained a smaller q' (10 eV/unit strain) calculated from literature data under some ideal assumptions, which ignored the strain impact on diffusion prefactors [16]. In 2007, Xia *et al* studied the impact of compressive strain on Si-Ge interdiffusion based on SIMS analysis [10]. First, an interdiffusivity model was built for the fully relaxed condition (no strain) with the Boltzmann-Matano method as a reference. Then the impact of compressive strain on interdiffusivity was extracted as an exponential factor, $e^{14.9*\frac{|\varepsilon|}{0.042}}$. Compared with the accurate expression $e^{\frac{-q^{'}\varepsilon}{kT}}$, we can see the factor $\frac{1}{kT}$ and the temperature dependence of q' are missing in the exponential factor in ref. [10].

In reality, q' is an effective strain derivative of interdiffusivity, which includes the impact of strain on both Ge diffusion and Si diffusion. Based on Darken's law, $\widetilde{D} = D_{Si}^{intrinsic} x_{Ge} + D_{Ge}^{intrinsic}(1 - x_{Ge})$, interdiffusion at the low end of the Ge fraction range (close to pure Si) is dominated by Ge diffusion in SiGe whereas interdiffusion at the high end of the Ge fraction range (close to pure Ge) is dominated by Si diffusion in SiGe. For our samples with a medium Ge fraction, not only x_{Ge} and $1 - x_{Ge}$, but also Ge and Si self-diffusivities are comparable, so the impacts of strain on Ge diffusion and Si diffusion both contribute to q'. As is known, on the atomic scale, Si and Ge diffusions in SiGe can be mediated by either interstitials or vacancies, or both. Aziz showed that compressive strain enhances vacancy mediated self-diffusion while retards interstitial mediated self-diffusion [37, 145]. Therefore, q' for Si-Ge interdiffusion should also depend on the I- and V-mediated fractions, which depend on both temperature and Ge fraction. In Si and Si rich SiGe, Si and Ge self-diffusions are mediated by both interstitials and vacancies [25, 27, 147-150]. Cowern *et al* [68] demonstrated that for small values of Ge composition and strain, low temperature diffusions under inert ambient are mostly mediated by vacancies, with an interstitial fraction 0.22±0.04. As the Ge fraction increases, the vacancy mechanism becomes more and more dominant [25, 27, 151, 152]. Strohm *et al* concluded that when x_{Ge} is over 0.25, Ge self-diffusion is vacancy mediated based on the Ge concentration dependence of both the diffusion activation energy and prefactor [27]. Moreover, with atomistic kinetic Monte Carlo simulations, Castrillo *et al* showed that both Si and Ge self-diffusions are vacancy mediated over the medium Ge fraction range [23, 153]. Our experimental study shows that biaxial compressive strain does enhance the interdiffusivity in the medium Ge fraction range, which is consistent with previous calculations mentioned above.

5.5 Chapter summary

In summary, the role of compressive strain on Si-Ge interdiffusion in epitaxial SiGe heterostructures was systematically investigated both by experiments and by theoretical analysis. The Ge fraction x_{Ge} range (0.36 to 0.75) studied in this work extended the Ge fraction in previous studies to a wider regime. From the measurements of X-ray diffraction and Raman spectroscopy, it was demonstrated that the epitaxial SiGe structures were still pseudomorphic after thermal anneals. A complete theoretical analysis was presented to address the strain's impact on the interdiffusion driving force, the prefactor and activation energy of Si-Ge interdiffusivity. For the temperature range (720 °C to 880 °C) and the Ge fraction range (0.36 to 0.75), the strain energy contribution to the driving force enhanced the interdiffusion by 20%~30%, which should be considered in simulations of Si-Ge interdiffusion. The strain derivative of interdiffusivity, q', was shown to be temperature dependent for the first time. q' was quantitatively extracted from the experimental data in the same range of Ge fraction and temperature, and was shown to have the form of $q' = (-0.081T + 110)$ eV/unit strain, where T is temperature in Kelvin.

Chapter 6 Si-Ge Interdiffusion with Partial Strain Relaxation

In Chapter 4 and 5, Si-Ge interdiffusion was investigated under two ideal conditions: without strain or with full coherent strain. In this chapter, the interdiffusion behaviour with partial strain is studied. This is of great relevance to the semiconductor industry, as strain relaxation is very common in semiconductor devices due to thin film thicknesses [61, 62], high Ge fractions [154], high temperature anneals and ion implantation damage [155, 156] etc. For example, partially relaxed SiGe is very common in MOSFETs, where SiGe in source and drain regions sees ion implantation and high temperature anneals. In HBT applications, it is less common as the SiGe layers are of lower Ge fraction (< 25% is common), which are more immune to strain relaxation.

This issue is very complicated because interdiffusion, strain relaxation and dislocation formation happen simultaneously and, as we discussed, interdiffusion strongly depends on compressive strain. The characterization and theoretical modeling of Si-Ge interdiffusion under such complicated conditions remain a considerable challenge. In this chapter, some new light is shed on this issue.

6.1 Introduction to strain relaxation in epitaxial thin films

6.1.1 Definition of strain relaxation

In Chapter 5, the compressive strain in the $Si_{1-y}Ge_y$ layer decreased as the Ge fraction in this layer decreased due to interdiffusion, but the top four layers still remained pseudomorphic (or coherent) based on the Raman and XRD analysis within the experimental measurement error bar. There was no observable plastic strain relaxation through dislocations. Therefore, strain reduction happens only by Si-Ge interdiffusion, with structure coherency maintained. To avoid confusion, in the following sections of this chapter, the strain relaxation only refers to plastic

relaxation via dislocations, not to strain reduction by Si-Ge interdiffusion. The degree of plastic strain relaxation, R, by the introduction of suitable dislocations at the interfaces of heterostructures [157] can be expressed as

$$R = \frac{a-a_s}{a_r-a_s} \times 100\% \quad (6.1)$$

where a, a_r and a_s are the in-plane lattice parameters of an epitaxial layer with partial strain relaxation, the epitaxial layer with full relaxation and the substrate respectively.

6.1.2 Strain relaxation during thermal anneals

Most of previous studies mentioned in Section 3.1 focused on the thickness dependence of strain relaxation in epitaxial films with constant Ge fractions [61, 62, 64, 158], and tried to find the critical thickness at which the mismatch strain starts to relax (see Figure 3.1). Other researchers also investigated the strain relaxation and dislocation kinetics in the growth of the graded SiGe layers (as virtual substrates) [73, 106, 110, 159, 160].

On the other hand, strain in SiGe films can relax during post-growth anneals [161-166]. In 1994, Gillard *et al* demonstrated that for thin compressively strained SiGe films (the thicknesses fall in the metastable regime), the residual strain after anneals was higher than the theoretical prediction [161]. Based on the experimental measurements of residual strains in SiGe/Si heterostructures after thermal anneals, it was found that at certain time point, relaxation stops when the residual strain is too low to drive threading segments past misfit dislocations. Gillard *et al* concluded that the blocking of threading dislocation segments plays an important role in the late stage of strain relaxation and it may limit the possibility of obtaining 100% relaxed SiGe films even after thermal anneals.

Most of the studies mentioned above focused on the dislocation kinetics during strain relaxation. However, interdiffusion under partial strain relaxation has seldom been reported. In 1994,

Fischer and Zaumseil investigated strain relaxation at high anneal temperatures in a metastable $Si_{0.68}Ge_{0.32}$ (86 nm) layer grown on Si substrate with in-situ XRD [162]. In their study, it was found that the R showed a time dependence. In addition, for a same anneal time, as the temperature increased, the relaxation rate got faster. At relatively lower temperatures, strain relaxation was dominant and there was negligible interdiffusion. However, when the temperature went up to 1000 °C, interdiffusion between the SiGe and Si layers happened. Fischer and Zaumseil just gave a phenomenal description of the Si-Ge interdiffusion with strain relaxation. In 2002, Aubertine *et al* modeled the Si-Ge interdiffusion under partial strain in multiple SiGe quantum wells [15]. However, the Ge fraction in their study was less than 0.20 and the contribution of strain energy to the interdiffusion driving force was ignored. So, a quantitative model is still missing for the Si-Ge interdiffusion under partial strain over a higher Ge fraction range.

In this chapter, the interdiffusion behaviour with partial strain is investigated. The strain relaxation is characterized using XRD and then the quantitative modeling is done for Si-Ge interdiffusion under partial strain.

6.2 Experiments

In the structure of S4585, the compressive $Si_{1-y}Ge_y$ (y = 0.85) layer was designed to be metastable, which tends to relax during thermal anneals. Its structure is shown in Figure 6.1. SIMS measurements were employed to obtain the as-grown and annealed Ge profiles of S4585. Additionally in order to obtain the strain status in each layer of S4585, an ex-situ strain analysis with Raman spectroscopy and XRD was performed. Raman spectroscopy was used to measure the strain in the top two layers while XRD measured the strain in the compressive $Si_{1-y}Ge_y$ and bottom $Si_{1-x}Ge_x$ (x = 0.45) layers.

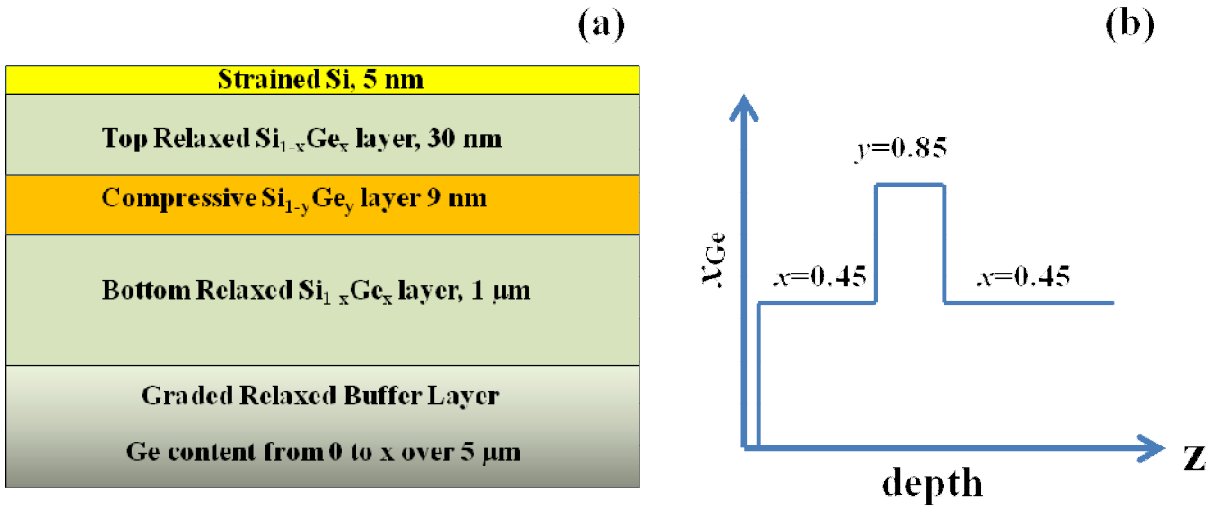

Figure 6.1 (a) Sample structure, and (b) the schematic depth profile of Ge fraction.

6.2.1 Thermal anneals and Ge depth profiling by SIMS

For S4585, the compressive $Si_{1-y}Ge_y$ layer is metastable, which tends to relax during thermal anneals. Three anneal conditions were designed for S4585: 760 °C, 800 °C and 840 °C, and the anneal time was 40 minutes. The Ge profiles of the $Si_{1-y}Ge_y$ layers are shown in Figure 6.2 (a). The Ge peak of the as-grown $Si_{1-y}Ge_y$ layer has a triangle-like shape, since interdiffusion occurred during the growth of the top 2 layers after the $Si_{1-y}Ge_y$ layer was grown. This interdiffusion during the growth was hard to minimize due to the large Ge fraction and higher compressive strain in the layer. Simulations were conducted with the established models under two ideal conditions in our previous work. One model is the unified model without strain (equivalently R=1) built over the full Ge fraction range in Chapter 4, and the other is the interdiffusivity model with full compressive strain (equivalently R=0) in Chapter 5. The SIMS profiles fall in between the model predictions under these two extreme strain conditions. In Figure 6.2, these comparisons indicate that the strain has partially relaxed during the thermal anneals. The strain enhancement of Si-Ge interdiffusion is still there, but less effective.

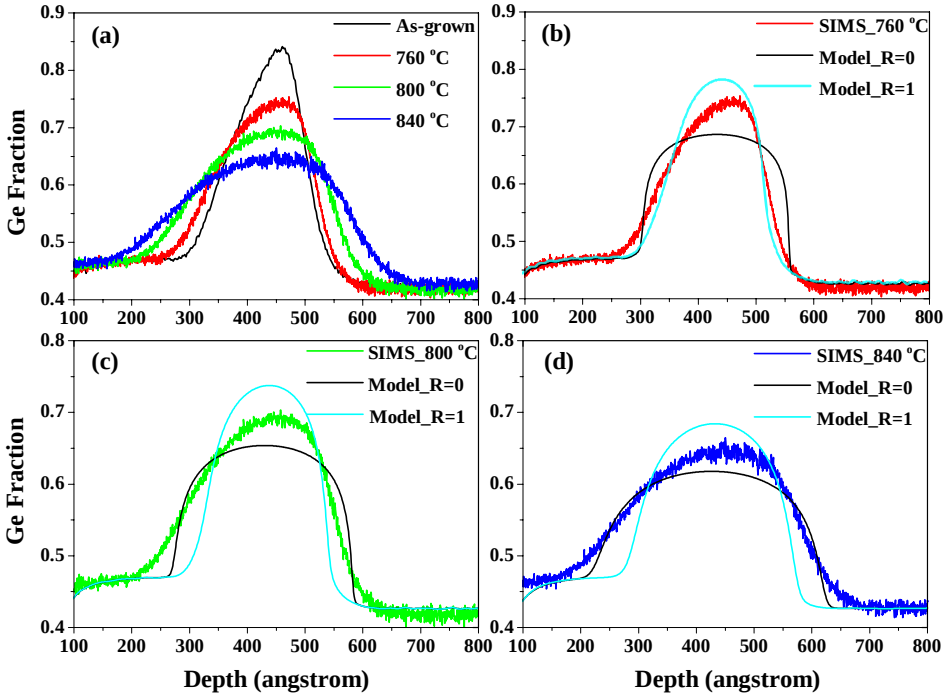

Figure 6.2 (a) Ge profiles measured by SIMS for as-grown and annealed samples; Comparison between SIMS data and model simulations under the two extreme conditions (R=0 and R=1): (b) for 760 °C for 40 mins, (c) for 800 °C for 40 mins and (d) 840 °C for 40 mins.

6.2.2 Ge fraction and strain analysis by HRXRD

In order to study the strain status in the compressive $Si_{1-y}Ge_y$ and bottom $Si_{1-x}Ge_x$ layers, HRXRD measurements were performed. In Figure 6.3, the 004 symmetric and 115 asymmetric XRD scans from S4585 are shown. The strongest peak is from the Si substrate, and on the right of it, there is a broad bump from the thin top Si cap layer. The second strongest peak is from the thick bottom $Si_{1-x}Ge_x$ layer. Unlike the XRD scans from S4065 and S5075 in Chapter 5, the shoulder from the top $Si_{1-x}Ge_x$ layer almost disappears, which is consistent with the SIMS results where the compressive $Si_{1-y}Ge_y$ layer is more triangle-shaped and the thickness of the

top relaxed $Si_{1-x}Ge_x$ layer is greatly reduced after anneals. The peaks from the compressive $Si_{1-y}Ge_y$ layers are relatively broad due to their shape and small thickness. Using the Si substrate peak as a reference, we can see that the peaks from the $Si_{1-y}Ge_y$ layers shift to the right and become more intense and narrower after anneals. This indicates that the $Si_{1-y}Ge_y$ layer becomes thicker and has a lower Ge fraction and lower strain after anneals, as expected due to the Si-Ge interdiffusion and strain relaxation.

In addition, based on the peak positions from the symmetric and asymmetric scans at phi=0° and 180°, the Ge fraction and strain in the $Si_{1-y}Ge_y$ and the bottom $Si_{1-x}Ge_x$ layers were extracted by simulations with the PANalytical Epitaxy software package as in Chapter 5, which are summarized in Table 6.1. The R value of the bottom $Si_{1-x}Ge_x$ layers is around 96%, which indicates that the bottom $Si_{1-x}Ge_x$ layers are very close to full relaxation. There is also about 10% relaxation in the as-grown metastable $Si_{1-y}Ge_y$ layer, and after annealing, the R value of this layer increases up to 50% relaxation, depending on the thermal budget. Based on the SIMS profiles and the XRD strain analysis, it is demonstrated that the interdiffusion and strain relaxation occurred at the same time in S4585. In addition, reciprocal space mappings have been done for S4585 shown in Figure 6.4, but there are no distinct peaks for the $Si_{1-y}Ge_y$ layers, due to the weak diffraction intensity from this layer.

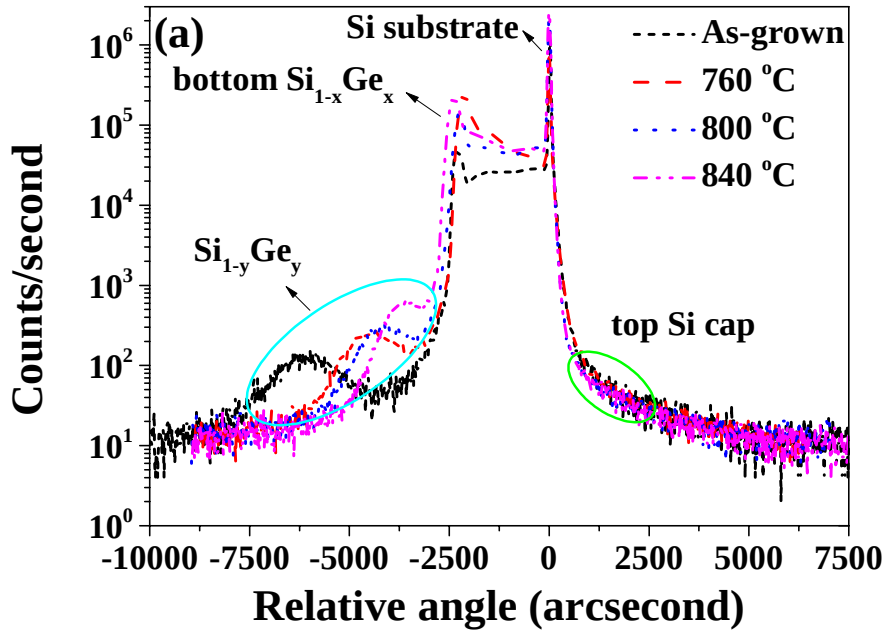

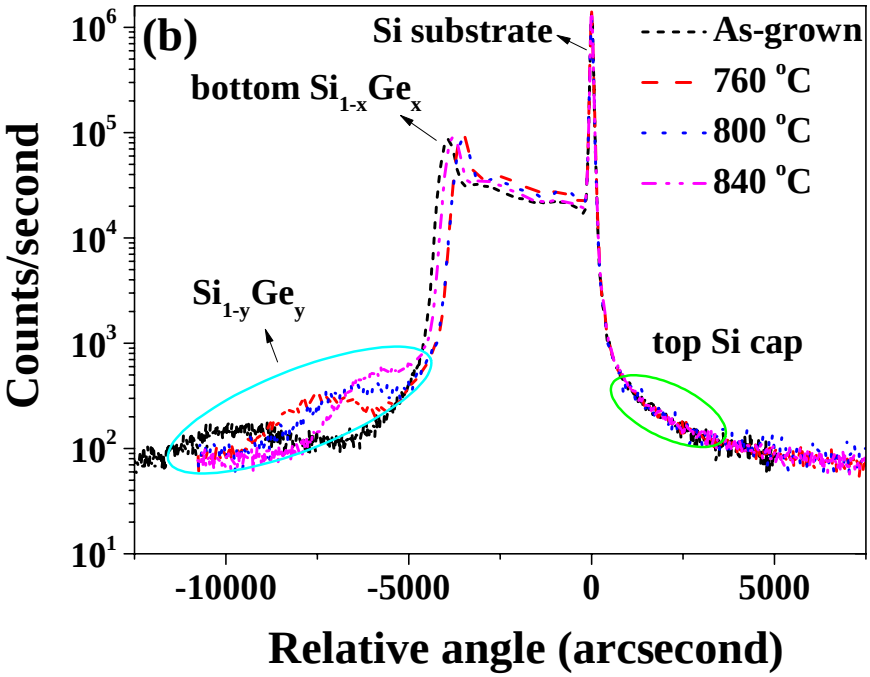

Figure 6.3 (a) 004 symmetric XRD and (b) 115 asymmetric scans at phi=0° from S4585 samples. The most intense narrow peak is from the Si substrate. The second strongest peak is from the bottom $Si_{1-x}Ge_x$ layer. The broad peak on the far left is from the thin $Si_{1-y}Ge_y$ layer.

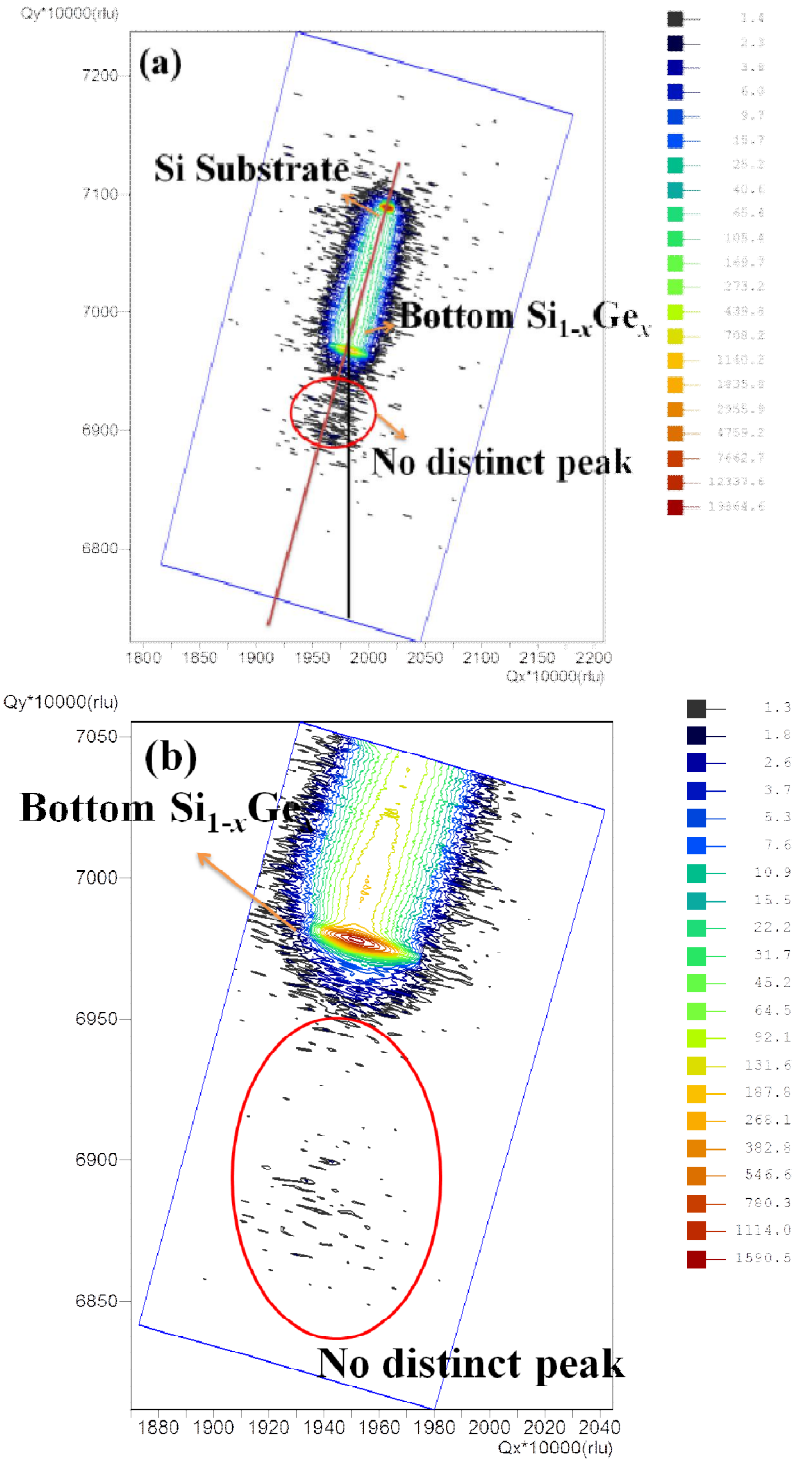

Figure 6.4 115 Reciprocal space mapping: (a) full map including the substrate peak for S4585 annealed at 840 °C for 40 mins, (b) narrow mapping without the substrate peak for S4585 annealed at 800 °C for 40 mins. Due to the weak diffraction intensities from the $Si_{1-y}Ge_y$ layers, there are no distinct peaks from them in the RSM.

Table 6.1 Ge fraction and the relaxation R in the compressive $Si_{1-y}Ge_y$ layers and the bottom $Si_{1-x}Ge_x$ layers from XRD measurements. The error bars of Ge fraction and relaxation R are ±0.01 and ±5 respectively for $Si_{1-y}Ge_y$ layers, and ±0.005 and ±0.5 respectively for the bottom $Si_{1-x}Ge_x$ layers.

sample	Thermal condition	$Si_{1-y}Ge_y$ layer		Bottom relaxed $Si_{1-x}Ge_x$ layer	
		y	R (%)	x	R (%)
S4585	As-grown	0.840	10	0.422	97.0
	760 °C	0.734	45	0.418	96.5
	800 °C	0.683	45	0.425	96.0
	840 °C	0.622	50	0.430	96.0

6.2.3 Ge fraction and strain analysis by Raman spectroscopy

Raman spectroscopy is complementary to HRXRD for measuring the strain in the top thin films, which are hard to dissolve in HRXRD due to their small thicknesses. It is especially useful to obtain the strain information in the top two layers by comparing the Raman peaks from the as-grown sample with the ones from the annealed samples. Raman spectra for the as-grown and three annealed samples are shown in Figure 6.5. There is almost no obvious shift for the three strong peaks from the top $Si_{1-x}Ge_x$ layers. For the top Si cap, its Si-Si peak begins to merge with the Si-Si peak from the top $Si_{1-x}Ge_x$ layer at 840 °C. Based on the correlation equations between Raman peak positions and Ge fraction and strain shown in Chapter 5, the Ge fraction and strain in the top two layers are quantitatively obtained, as shown in Table 6.2. The top silicon layers are still tensilely strained. Compared to the slight compressive strain in the top $Si_{1-x}Ge_x$ layers of S4065 and S5075, the tensile strain in the top $Si_{1-x}Ge_x$ layers of S4585 indicates that the $Si_{1-y}Ge_y$ layers were partially relaxed after anneals, which is consistent with the XRD results in Section 6.2.2.

Table 6.2 Ge fraction and strain in the top two layers from Raman measurements. Si layer is under tensile strain and the top $Si_{1-x}Ge_x$ layer is slightly tensile strained. The error bars of Ge fraction and strain are ±0.01 and ±1.0×10^{-3} respectively. x' denotes the Ge fraction in the top $Si_{1-x}Ge_x$ layer.

sample	Anneal conditions	Top $Si_{1-x}Ge_x$ layer		Top Si
		x'	ε	ε
S4585	As-grown	0.422	0.0045	0.0195
	760 °C 40mins	0.428	0.0037	0.0188
	800 °C 40mins	0.440	0.0026	0.0195
	840 °C 40mins	0.436	0.0030	0.0208

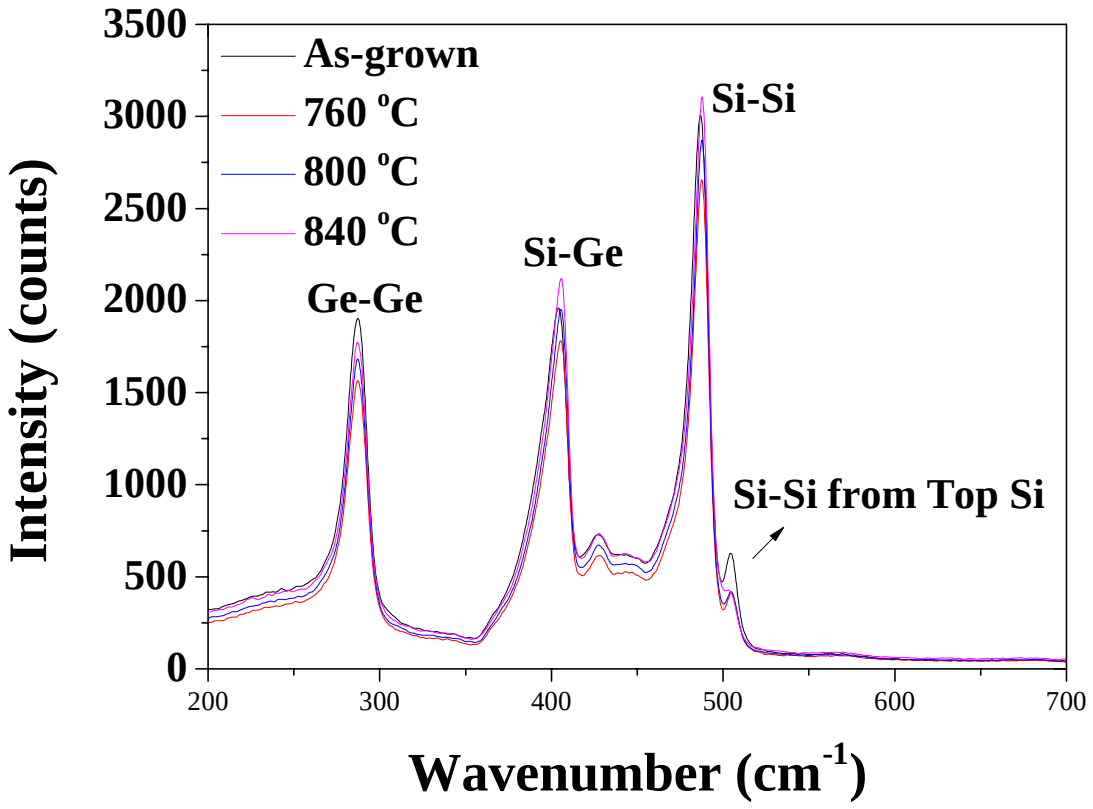

Figure 6.5 Raman spectra from the as-grown and annealed samples of S4585. The three strong peaks are from top $Si_{1-x}Ge_x$ layers. The right small peak is from the top silicon layer, which is under tensile strain.

Compared with the results of S4065 and S5075 discussed in Chapter 5, S4585 is not coherent due to the strain relaxation by misfit dislocations. Therefore, it is expected that the TDD is different in the top three layers from that in the relaxed bottom SiGe layer. As EPD measurements require certain etch depth to form big enough etch pits for microscope observation, it is not suitable to measure the TDD in the top 3 layers of S4585. High resolution TEM is more suitable for dislocation characterizations in ultra thin films, which can be a topic for future work.

6.3 Theoretical modeling for Si-Ge interdiffusion with partial strain relaxation

Based on Fischer and Zaumseil's work [163], for biaxially strained layers with partial strain grown on virtual substrates, the biaxial strain $\boldsymbol{\varepsilon}$ of a partly relaxed layer is given by

$$\varepsilon = \varepsilon_0(1 - R) \qquad 6.2$$

where ε_0 is the lattice mismatch strain in a coherently strained epitaxial film. For $Si_{1-y}Ge_y$/ $Si_{1-x}Ge_x$ heterostructures, conventionally, $\varepsilon_0 = -\eta(x_{Ge} - x_0)$, as the expression in Equation 5.5 in Chapter 5. R is the plastic relaxation defined in Equation 6.1. Correspondingly, the total Helmholtz free energy can be ideally expressed as

$$F = A\int[f_0(x_{Ge}) + Y_{UVW}\varepsilon^2]\,dz = A\int[f_0(x_{Ge}) + Y_{UVW}(1-R)^2\eta^2(x_{Ge} - x_0)^2]\,dz \qquad 6.3$$

where A is the cross-section area normal to the z axis; $f_0(x_{Ge})$ is the Helmholtz free energy per unit volume of the homogeneous solution at the Ge atomic fraction of x_{Ge}; Y_{UVW} is the biaxial modulus, which equals to $E/(1-\upsilon)$, where E is Young's modulus, and υ is Poisson ratio. For our samples, < UVW > is <100>. ε is the biaxial strain.

Following the derivation procedure in Chapter 5, the apparent interdiffusivity with a constant R can be expressed as

$$\widetilde{D}_{apparent} = \left(1 + \frac{2\eta^2(1-R)^2 Y_{UVW}}{f_0''}\right) \widetilde{D}^{relax} e^{\frac{-q'\varepsilon_0(1-R)}{kT}} \quad 6.4$$

where f_0'' is the second derivative of f_0; $\widetilde{D}^{relax}$ is the interdiffusivity without strain in Chapter 4, and q' is the strain derivative of interdiffusivity in Chapter 5, $q' = 110 - 0.081T$. T is the absolute temperature in Kelvin.

In Equation 6.4, the relaxation R appears in two places, $(1-R)^2$ in the large parenthesis for the driving force change and $(1-R)$ in the exponential term for the interdiffusivity change. When the R value equals 1, we can see the apparent interdiffusivity equals $\widetilde{D}^{relax}$, where there is no strain impact. When the R value equals to zero, the apparent interdiffusivity is same as the model with full compressive strain built in Chapter 5. The apparent interdiffusivities with different relaxation R values at 800 °C and 840 °C are compared in Figure 6.6. The apparent interdiffusivity when R=0.5 is in between those when R=0 and R=1. The biaxial compressive strain reduces to $\varepsilon_0(1-R)$, correspondingly, the strain enhancement of interdiffusion decreases, which is consistent with the SIMS results in Figure 6.2. If the R is unchanged during thermal anneals, theoretically the interdiffusion can be simulated with Equation 6.4. However, the real situation is more complicated, because the R value is time-dependent. In next section, more discussion is on this issue.

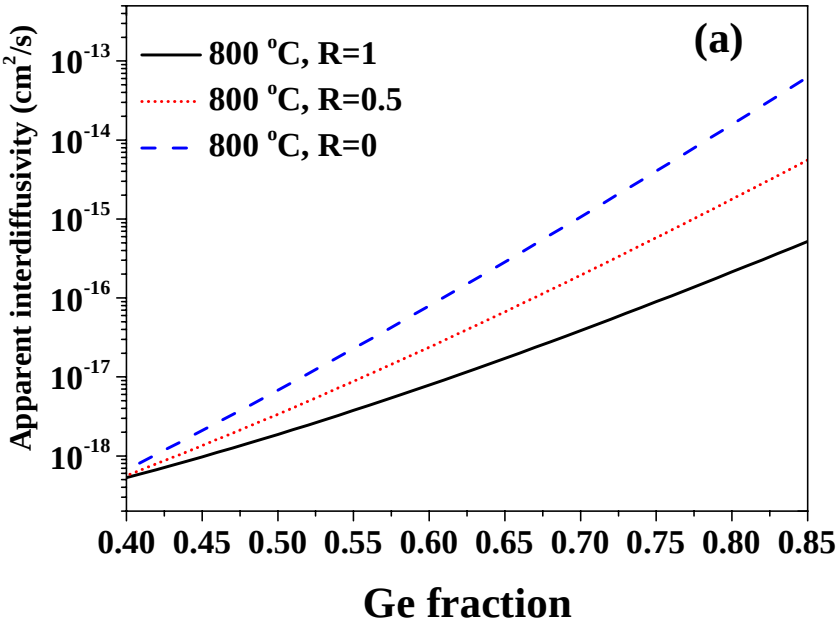

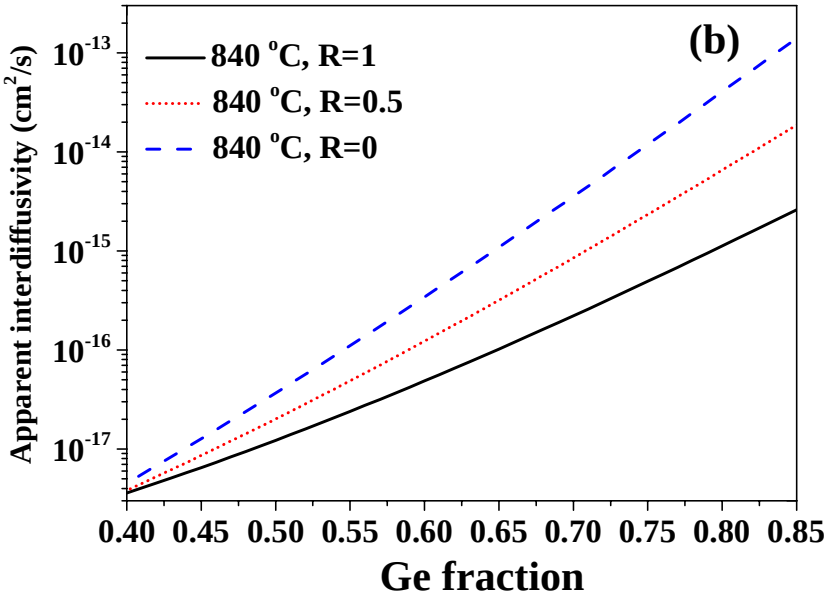

Figure 6.6 Comparison of apparent interdiffusivity vs. x_{Ge} for SiGe on a $Si_{0.60}Ge_{0.40}$ virtual substrate with different relaxation R values: (a) at 800 °C and (b) at 840 °C.

6.4 Time dependence of the relaxation R and Si-Ge interdiffusion

6.4.1 Time dependence of the relaxation R

The R values after anneals depend on multiple factors such as Ge fraction, layer thickness, as-grown relaxation, anneal temperature and time [161-163]. Based on the strain analysis in Section 6.2.2, the R value in the metastable $Si_{1-y}Ge_y$ layer of S4585 increased to about 50% after anneals. In order to obtain better understanding of the time dependence of R, three more anneals are performed at each temperature used in Section 6.2.2 (760 °C, 800 °C, 840 °C). The sample naming convention is the following: as-grown (AG), ramp up and down only (RUDO), ramp up and down plus 10 minutes (RUD10), ramp up and down plus 20 minutes (RUD20) and ramp-up and down plus 40minutes (RUD40). The ramp-up and ramp down rates are 40 °C/min and 100 °C/min respectively. The R values were characterized by the HRXRD method, discussed earlier in Section 6.2.2. The temperature profiles of the four scenarios at 800 °C are shown in Figure 6.7 (a). The time dependence of R at the three anneal temperatures is shown in Figure 6.7 (b).

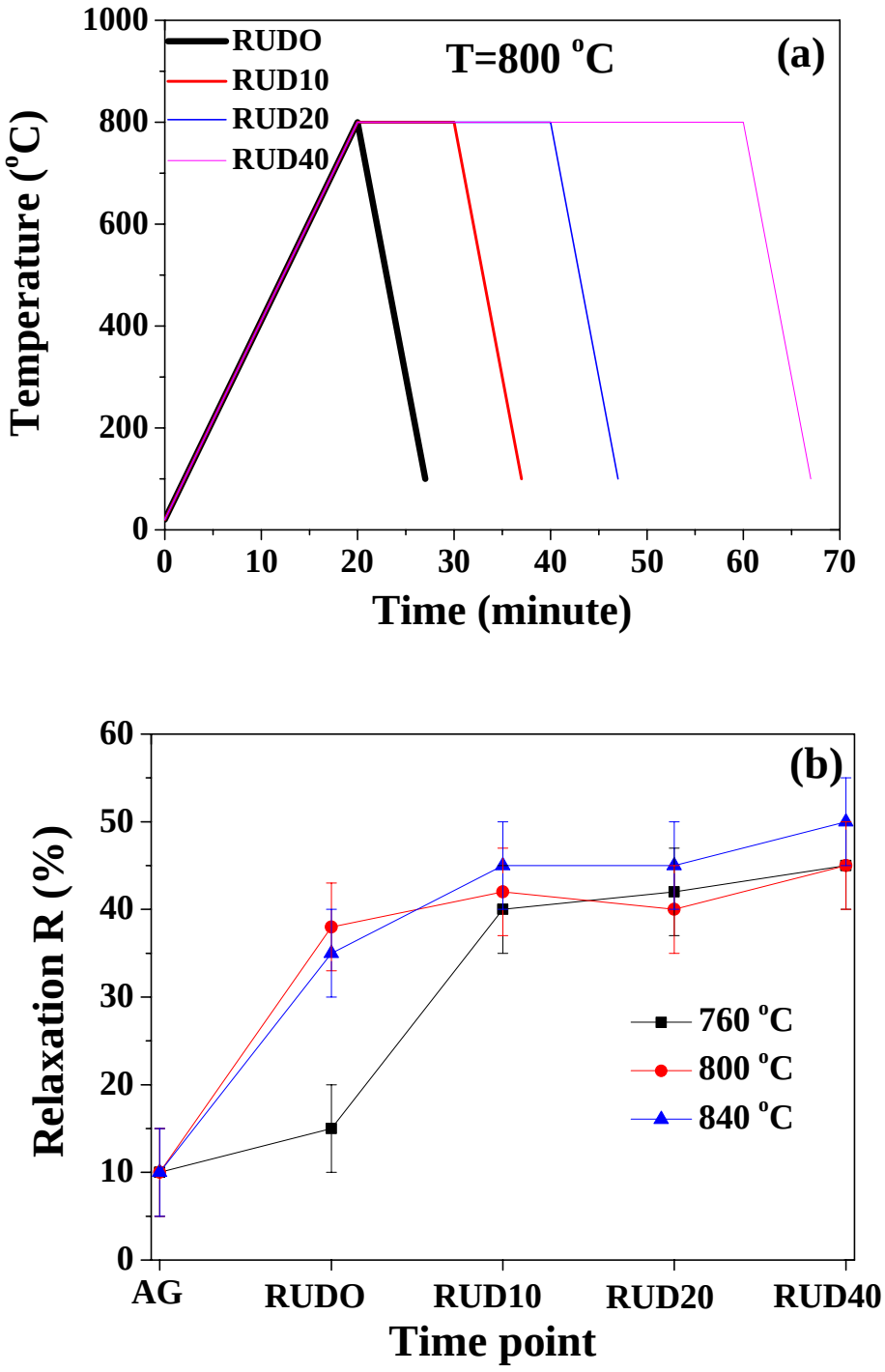

Figure 6.7 (a) Temperature profile for the four anneal scenarios at 800 °C: RUDO, RUD10, RUD20 and RUD40. (b) Time dependence of the relaxation *R* at three different anneal temperatures. For each temperature, there are five time scenarios: AG, RUDO, RUD10, RUD20 and RUD40.

From Figure 6.7 (b), we can see that the R value increased greatly first, then went up to around 50% and gradually saturated with the anneal time, forming a “plateau”. The shape of the time dependence of R in Figure 6.7(b) is consistent with that of the in-situ XRD measurements reported by Fischer and Zaumseil [163]. At 760 °C, the relaxation rate was slower than the other two temperatures, and the R value reached the plateau at RUD10. In contrast, at 800 °C and 840 °C, the R value almost reached the plateau state after the ramp-up stage. Considering the slower ramp-up rate (40 °C/min) compared to the ramp-down one (100 °C/min), it is reasonably thought that the strain relaxation happened dominantly in the ramp-up stages. After that, the R value only increased by small amounts as the anneal time increased.

6.4.2 Time dependence of Si-Ge interdiffusion at 800 °C

The Ge profiles of the partially strained $Si_{1-y}Ge_y$ layers at different time points at 800 °C were measured by SIMS, shown in Figure 6.8. Comparing the SIMS profile of RUDO with the as-grown one, the Si-Ge interdiffusion was negligible during the ramp up and down stages, where the Ge peak decreased by about 1 at.%, which is within the SIMS measurement uncertainty of Ge fraction. If we compare the Ge fraction peaks after the 10, 20 and 40-minutes diffusions, we see that the Ge peak drop in the first 10 minutes is much more than that in the next 10 minutes and the next 20 minutes. As the anneal time increased, the rate of the peak drop in the $Si_{1-y}Ge_y$ layer became slower. According to the model for interdiffusion with partially relaxed compressive strain in Equation 6.4, at 800 °C the interdiffusivity of a 10% relaxed $Si_{0.17}Ge_{0.83}$ (the case of the as-grown sample) is almost 100 times larger than that of a 42% relaxed $Si_{0.27}Ge_{0.73}$ (the case of the RUD10 sample at 800 °C). This big difference in interdiffusivity explains why the Ge peak drop is faster during the first 10 minutes in Figure 6.8.

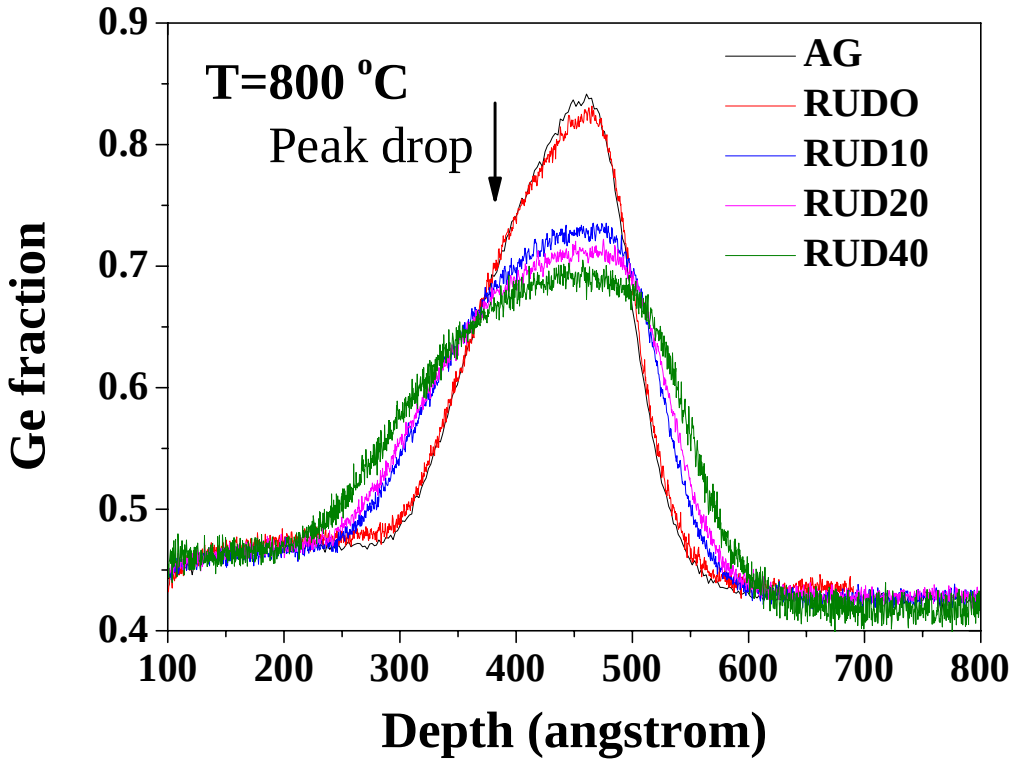

Figure 6.8 Ge profiles measured by SIMS for as-grown and annealed samples with different anneal times.

6.5 Model predictions and discussion

Based on the SIMS data and the time dependence of the R value and Si-Ge interdiffusion in Section 6.4, we can see that for higher anneal temperatures (800 °C and 840 °C), the R value reached a plateau after the ramp-up stage, and Si-Ge interdiffusion was negligible. In other words, strain relaxation happened before Si-Ge interdiffusion in samples annealed at 800 °C and 840 °C. Therefore, Si-Ge interdiffusion can be simulated using the model with a constant R in Section 6.3, which was implemented in TSUPREM-4^{TM}. The average R value of the three relaxation values at RUD10, RUD20 and RUD40 was used for those simulations. At 800 °C for different anneal times (10 minutes, 20 minutes and 40 minutes), an average R value of 42%

was used; while at 840 °C for 40 minutes, an average R value of 47% was used. The comparisons between the model predictions for the anneals at 800°C and 840 °C and the corresponding SIMS profiles are shown in Figure 6.9.

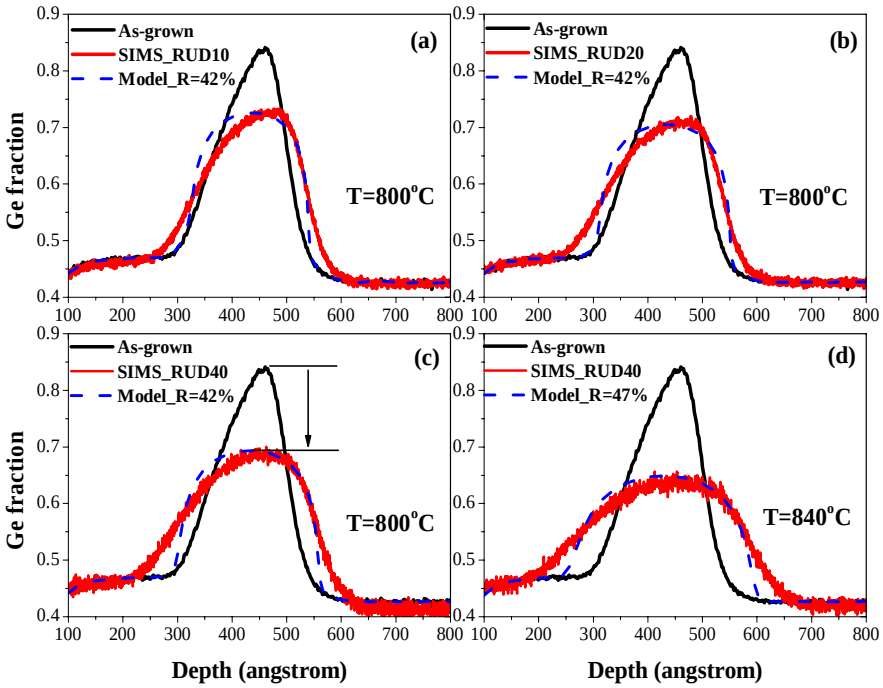

Figure 6.9 Comparisons between the model predictions and SIMS profiles: (a) for RUD10 at 800 °C, R=42%; (b) for RUD20 at 800 °C, R=42%; (c) for RUD40 at 800 °C, R=42%; (d) for RUD40 at 840 °C, R=47%.

From Figure 6.9, it is demonstrated that the peak drops predicted by the modified model in Equation 6.4 match the ones from the SIMS data for all the four anneal conditions within the SIMS measurement error bar. However, in Figure 6.9, we can also see the peak shapes of the model predictions do not perfectly match the experimental ones, i.e., the rising and falling edges of the simulated peaks are steeper than those of the SIMS profiles. The steep edges of the model predictions are caused by the strong concentration and compressive-strain dependence

of Si-Ge interdiffusivity in the model in Equation 6.4. Based on Fick's first law, $J = -D\frac{\partial C}{\partial z}$, the diffusion flux is decided by both the diffusivity and the concentration gradient. From the as-grown SIMS profile of S4585, we can see the rising and falling edges are close to linear, so the concentration gradient is almost constant along the rising and falling edges at time t=0. Therefore, the diffusion flux is primarily decided by the interdiffusivity. At the locations with a larger Ge fraction and thus higher compressive strain, the diffusion flux is much larger. For S4585, the diffusion flux has a very strong Ge-concentration dependence, which is illustrated in Figure 6.10. So according to the model in Equation 6.4, at higher Ge concentrations, the diffusion is much faster than at lower Ge concentrations. As time increases, theoretically the rising and falling edges get steeper.

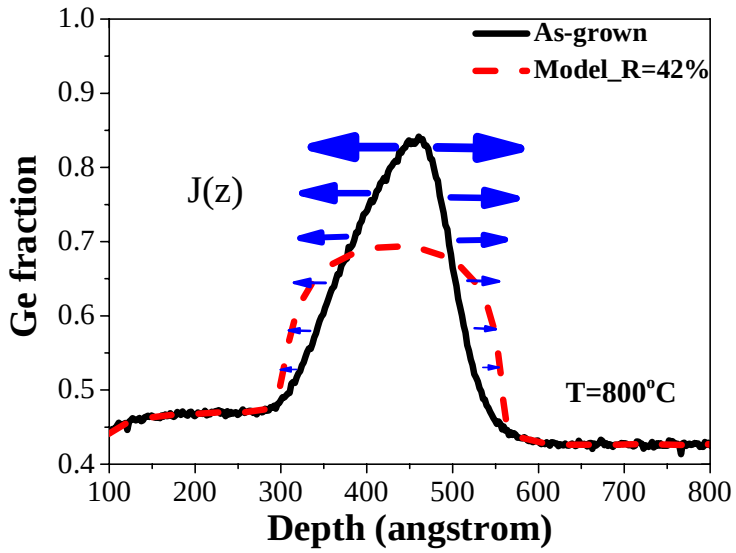

Figure 6.10 Schematic illustration of the diffusion fluxes at different Ge concentrations at the starting time point t=0, based on the model in Equation 6.4.

However, this is not what we observed from the SIMS data. The edges of all the SIMS Ge peaks were flatter and went farther than the edges of the simulated Ge peaks, and the Ge peaks did not get steeper as Equation 6.4 predicted. This issue can be explained by the

dislocation mediated interdiffusion, which is not included in Equation 6.4. Equation 6.4 only accounts for the lattice mediated interdiffusion, $D_{lattice}$. Strain relaxation in SiGe multi-layers is mainly ascribed to the formation of misfit dislocations at the interfaces and their following movements during thermal anneals [15, 106, 110]. For S4585, the dislocation density is expected to be higher when strain relaxation occurs compared to the cases where no strain relaxation happens as in Chapter 4 and 5. In order to estimate the impact of the relaxation induced dislocations, an additional term $D_{dislocation}$ is added to $D_{lattice}$ in calculating the total interdiffusivity D_{total} as Gavelle et al did for modeling Si-Ge interdiffusion in highly defected Ge/Si heterostructures [21]. Then the total interdiffusivity can be expressed as

$$D_{total} = D_{lattice} + D_{dislocation} \quad 6.5$$

where $D_{lattice}$ is the diffusivity in Equation 6.4 for lattice mediated interdiffusion, and $D_{dislocation}$ is the collective diffusivity contributed from relaxation induced dislocations.

In Gavelle et al's study, they used an Arrhenius term to describe the impact of the relaxed induced dislocations on the Si-Ge interdiffusion [21]. In this work, a similar Arrhenius expression is used to estimate the impact of dislocations analytically.

$$D_{dislocation} = D_0^{dis}(x_{Ge})e^{-\frac{E_a^{dis}}{kT}} \quad 6.6$$

where D_0^{dis} and E_a^{dis} are the prefactor and activation energy respectively. In Ref. [21], D_0^{dis} = $0.01\,exp(2.5x_{Ge})$ and E_a^{dis} = $3.1\,eV$. "dis" denotes relaxation induced dislocations.

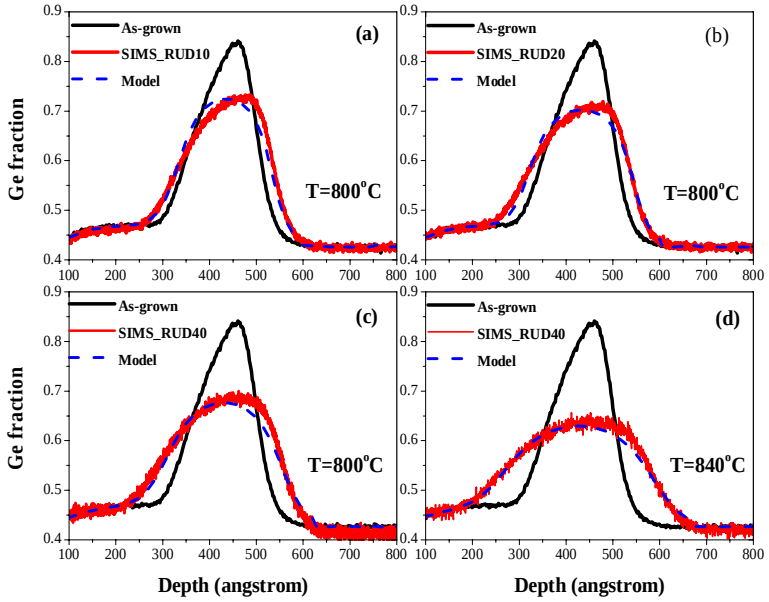

Figure 6.11 Best fittings to the SIMS profiles for the extraction of D_0^{dis} and E_a^{dis} of $D_{dislocation}$: (a) RUD10 at 800°C; (b) RUD20 at 800°C; (c) RUD40 at 800°C and (d) RUD40 at 840°C.

In order to quantify the impact of the dislocations in the tail regions of S4585, the parameters in Equation 6.6 were extracted by fitting the SIMS profiles, as shown in Figure 6.11. The extracted prefactor D_0^{dis} is expressed as $0.017exp(x_{Ge})$ and the activation E_a^{dis} is around 3.15 eV. It should be noted that the structures in Gavelle et al's work were highly defected relaxed Ge films on Si. The dislocation density in their samples is not expected to be the same as that in this work. From Figure 6.11, we can see that in the tail regions the simulation results fit the SIMS profiles much better, compared with the simulations using $D_{lattice}$ only as seen in Figure 6.9. The comparison between the total interdiffusivity D_{total} and the point-defect mediated interdiffusivity $D_{lattice}$ is shown in Figure 6.12. In the relatively lower Ge fraction region, the interdiffusion is strongly affected by the presence of relaxation induced dislocations, and the

interdiffusivity is enhanced by one order of magnitude. However, in the higher Ge fraction region, the total interdiffusivity is dominated by the $D_{lattice}$ term.

On the other hand, Ge doses (in unit of atoms/cm^2), which are the integrated areas underneath the Ge profiles in Figure 6.11, are compared, as shown in Figure 6.13. We can see all the ratios fall in between 0.996 and 1.004. Considering the measurement uncertainty of the SIMS analysis, the Ge doses are conserved.

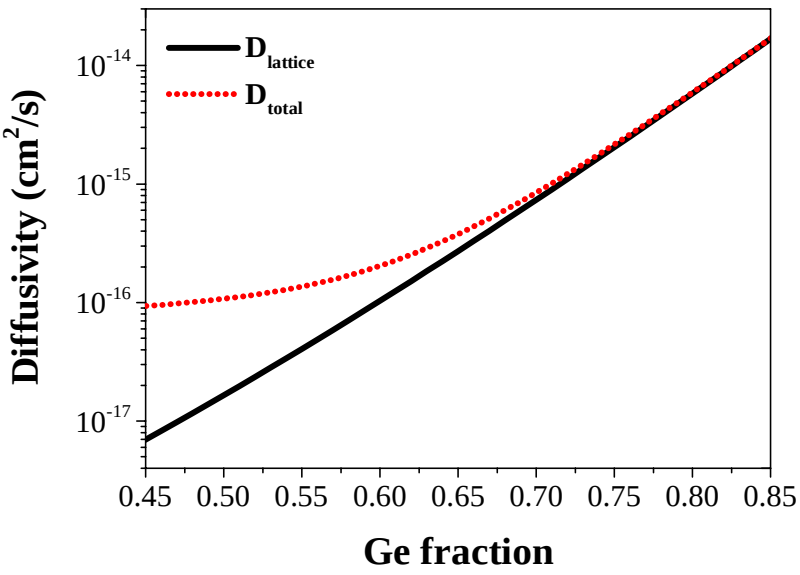

Figure 6.12 Comparison between the total interdiffusivity and $D_{lattice}$ for RUD40 at 840 °C.

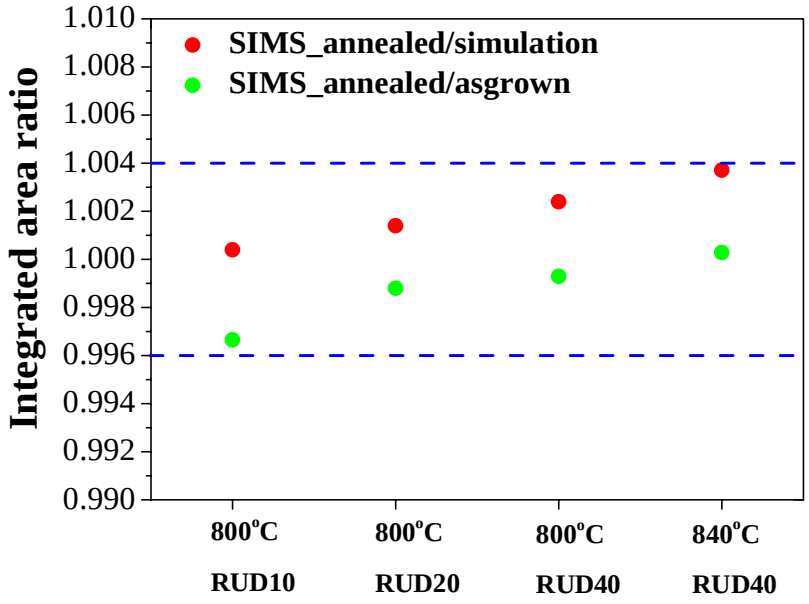

Figure 6.13 Integrated area ratios between the SIMS_annealed and the simulation, and the SIMS_annealed and the as-grown for RUD10, RUD20, and RUD40 at 800 °C, and RUD40 at 840 °C.

6.6 Chapter summary

In summary, this chapter focused on the Si-Ge interdiffusion in partially strain-relaxed epitaxial SiGe heterostructures, which is of great relevance to the semiconductor industry. Unlike sample S4065 and S5075 in Chapter 5, the as-grown compressive $Si_{1-y}Ge_y$ layer in S4585 was metastable and relaxed during the thermal anneals. Characterized by XRD and Raman spectroscopy, the $Si_{1-y}Ge_y$ layer was shown to be partially relaxed, and the R value reached about 50% relaxation after high temperature anneals. Furthermore, the time dependence of the R value in the $Si_{1-y}Ge_y$ layer was investigated by the ex-situ XRD measurements. It was found that the R values reached a “plateau” quickly during the ramp-up stages of the anneals at 800 °C and 840 °C. For the anneals at 800 °C and 840 °C, it means that the strain relaxation happened before Si-Ge interdiffusion.

With the approximation that the R value is constant after the ramp-up stages of the anneals at 800 °C and 840 °C, Si-Ge interdiffusion can be simulated by $D_{lattice}$ with an average value of R. The model gave close predictions of the decrease of the peak Ge concentration in the $Si_{1-y}Ge_y$ layer, which in turn validates the theoretical approach we used in Chapter 5. In addition, the impact of the dislocation mediated interdiffusivity $D_{dislocation}$ was quantified. This enhanced the interdiffusivity about one order of magnitude at the tail regions of S4585.This two-term model enables the prediction of the Si-Ge interdiffusion with strain relaxation, which is very common for SiGe stressors in p-MOSFETs. However, it should be used with caution, because for different samples and annealing conditions, strain relaxation may happen before, with or after Si-Ge interdiffusion. Thus, the time evolution of strain relaxation and Si-Ge interdiffusion should be well understood before using this model. In addition, $D_{dislocation}$ depends on the sample structure and its quality, and should be calculated for each set of samples. More systematic studies on the dislocation impact are necessary to address this issue.

Chapter 7 Summary and Future Work

7.1 Thesis summary

This work investigated the Si-Ge interdiffusion under three strain conditions: with zero strain, with full coherent strain and with partial strain.

As stated in Chapter 1, SiGe heterostructures with higher Ge fraction and larger Ge modulation have big advantages for the next-generation electronic and optoelectronic devices. Due to the lower melting point of SiGe alloys as Ge fraction increases, thermal budgets in the device fabrication should be adjusted to avoid Si-Ge interdiffusion, which degrades the performance of many SiGe devices.

This work contributes to the area of Si-Ge interdiffusion in the following aspects both by experiments and theoretical modeling:

1) Based on the correlation between self-diffusivity, intrinsic diffusivity and interdiffusivity in binary alloy systems, a unified interdiffusivity model was built over the full Ge fraction range for the first time. It unified previous interdiffusivity models and showed a good accuracy over the full Ge fraction range. Additionally, the validity of the unified model was proved by the comparisons between the simulations and the SIMS data from literature and experiments with different ranges of Ge fraction and anneal temperatures. It was demonstrated that our unified model gave reasonable predictions for Si-Ge interdiffusion under conventional furnace anneals, and advanced anneal techniques such as soak and spike RTAs. With wide applicable ranges of temperature and Ge fraction, the model can be applied to the designs of structure, epitaxial growth and process conditions for various SiGe devices. This new model also provides a zero

strain, no dopant effect, and low dislocation density reference for the studies of more impacting factors.

2) With the well-established reference of Si-Ge interdiffusivity, the impact of the biaxial compressive strain on Si-Ge interdiffusion was further investigated under two specific strain scenarios: full coherent strain and partial strain in epitaxial structures.

For the case with full coherent strain, the thickness of the compressive SiGe layer does not exceed the Matthews-Blakeslee equilibrium limit. Combining the advantages of Raman spectroscopy (for near-surface strain analysis) and HRXRD (for strain analysis in embedded layers), the strain was well characterized in the top four layers of the samples. The complete strain analysis demonstrated that the sample structure was still pseudomorphic (or coherent) after thermal anneals. Moreover, the threading dislocation density was estimated (10^5 cm^{-2}) by the EPD technique, which was well under the density (10^7 cm^{-2}) to cause any noticeable impact on interdiffusion. After ruling out the interferences from strain relaxation and threading dislocations, a complete theoretical analysis was presented to address the impact of compressive strain on the interdiffusion driving force, the prefactor and activation energy of interdiffusivity. The role of the compressive strain was modeled in two aspects: a) the strain energy contributes to the interdiffusion driving force; b) the strain derivative q' of interdiffusivity, reflecting the strain-induced changes of both the prefactor and activation energy of interdiffusivity. For the temperature range (720 °C to 880 °C) and the Ge fraction range (0.36 to 0.75), the strain energy contribution to the driving force enhanced the interdiffusion by 20%~30%, which should be considered. Moreover, the strain derivative q' was shown to have a temperature dependence, which was reported for Si-Ge interdiffusion for the first time. Based on the quantitatively extracted q' values from the experimental data in the same ranges of temperature and Ge fraction above, q' was shown to have the form of $q' = (-0.081T + 110)$ eV/unit strain, where T is the absolute temperature.

3) For the case with partial strain, the compressive SiGe layer is metastable and tends to relax during thermal anneals. Based on the strain analysis by ex-situ XRD measurements, the compressive SiGe layer was shown to be partially relaxed (to about 50%) after anneals. Compared to the predictions by the models without strain and with full coherent strain, the strain enhancement of Si-Ge interdiffusion was still present, but less effective due to the strain relaxation and thus dislocation formation. Based on the time dependence analysis of the relaxation R and Si-Ge interdiffusion, it was observed that the R value reached a "plateau" after the ramp-up stage and during this stage the interdiffusion was negligible for the anneals at 800 °C and 840 °C. For the case with partial strain, the apparent interdiffusivity model for full coherent strain needs to be modified to include the effect of R. Compared to the SIMS profiles of the annealed samples, the modified interdiffusivity model with $D_{lattice}$ only gave good predictions of Ge peak drops in the compressive SiGe layers. In addition, the impact of relaxation induced dislocations $D_{dislocation}$ at the tail regions was quantified. The interdiffusivity can be enhanced by one order of magnitude due to the dislocations.

To conclude, a set of interdiffusivity models were established based on the literature data and our experiments. Those models describe the Si-Ge interdiffusion under different strain scenarios, and are important both in technological applications and in fundamental interdiffusion researches. They can be employed to predict and estimate the interdiffusion in SiGe heterostructures for semiconductor devices, and optimize the design of SiGe epitaxial structures and thermal budgets for fabrication processes. For instance, the unified model in Chap 4 has been successfully integrated in CSUPREM, a software product for semiconductor process simulation, of our fund sponsor, Crosslight Software Inc.. On the theoretical side, these models can be used as reference lines for studies on Si-Ge interdiffusion with doping and/or with defects.

7.2 Suggestions for future work

In this work, two significant boundaries (without strain and with full coherent strain) of Si-Ge interdiffusivity have been successfully modeled. These two boundaries can be employed as reference lines. The unified model without strain was well validated with the literature SIMS data and the experimental data in different ranges of Ge fraction and temperature using different anneal tools such as furnace anneal, soak and spike RTAs. However, due to the scope of this thesis, many aspects of Si-Ge interdiffusion are not addressed in this work, and can be topics for future studies.

1) Due to the difficulty of growing high-quality pseudomorphic samples with high Ge fraction (0.85~1), the modeling of the strain impact was limited to the medium Ge fraction range (0.36~0.85) in this work. The strain derivative q' at the high Ge fraction range is still missing. Moreover, due to the prerequisite that the pseudomorphic structures should be maintained during anneals for the extraction of the strain derivative of interdiffusivity, the temperature range was confined to a range of 720 °C to 880 °C. Nevertheless, a valid procedure to extract q' values has been demonstrated in this work. Following this procedure, the strain derivative q' at the two ends of the Ge fraction range can be obtained and then a full picture can be established for the Ge concentration dependent q' over the full Ge fraction range.

2) On the other hand, the work on Si-Ge interdiffusion under partial strain shed some new light on the complicated correlation between interdiffusion, strain relaxation and dislocations. Compared with the Si-Ge interdiffusion under full coherent strain, a noticeable strain relaxation happened prior to Si-Ge interdiffusion. The impact of relaxation induced defects was quantified in this work, but a systematic model for the Si-Ge interdiffusion in SiGe heterostructures with high dislocation densities is still missing. This issue is very challenging, because the interactions between dislocations, point defects and strain fields are very complicated. In addition, for

different sample structures, the time dependences of the degree of strain relaxation R and of dislocation density are expected to vary. To refine the modeling under strain relaxation, an in-situ characterization of strain and dislocation, or an ex-situ strain analysis at more time points is required to obtain a better understanding of the time dependence of strain relaxation and dislocation evolvement. Moreover, the spatial distribution of dislocations should be considered, because there are local strain fields associated with dislocations, which possibly have impact on Si-Ge interdiffusion.

3) The study on Si-Ge interdiffusion in this work is free from the impact of doping. However, in real devices, SiGe alloys are normally doped with elements such as boron and phosphorus. As Si and Ge atoms and point defects interact with dopant atoms, it is expected that Si-Ge interdiffusion varies with the doping species and doping levels. Additionally, dopant diffusion and Si-Ge interdiffusion occur at the same time during thermal anneals, and are closely correlated. For the studies on the impact of doping, the interdiffusivity models in this work can be served as the baselines to estimate the impact of doping quantitatively.

4) In this work, the underlying point defect kinetics during interdiffusion, and the quantitative analysis of the contributions of vacancy- and interstitial-mediated diffusions were not discussed. On the atomic scale, the atoms of Si and Ge diffuse via both vacancies and interstitials. It is predicted by many theoretical studies that as the Ge fraction increases, the vacancy mechanism becomes more and more dominant. It is very valuable to obtain a full picture of the contribution ratios between vacancy and interstitial mechanisms over the full Ge fraction range.

5) In addition, the interdiffusivity modeling in this work is for the Si-Ge interdiffusion under thermal equilibrium. It is an interesting and significant topic to investigate Si-Ge interdiffusion under the conditions of non-equilibrium point defects, which can be introduced via surface reactions during anneals in an oxygen or ammonia ambient. Similarly, the interdiffusivity models

in this work can serve as the baselines to estimate those impacts caused by non-equilibrium point defects.

Bibliography

1. Thompson, S.E., et al., *A 90-nm logic technology featuring strained-silicon.* Electron Devices, IEEE Transactions on, 2004. 51(11): p. 1790-1797.
2. Gomez, L., et al., *Enhanced Hole Mobility in High Ge Content Asymmetrically Strained-SiGe p-MOSFETs.* IEEE Electron Device Letters, 2010. 31(8): p. 782-784.
3. Gomez, L., P. Hashemi, and J.L. Hoyt, *Enhanced Hole Transport in Short-Channel Strained-SiGe p-MOSFETs.* Electron Devices, IEEE Transactions on, 2009. 56(11): p. 2644-2651.
4. Bhuwalka, K.K., et al., *P-channel tunnel field-effect transistors down to sub-50 nm channel lengths.* Japanese Journal of Applied Physics Part 1-Regular Papers Brief Communications & Review Papers, 2006. 45(4B): p. 3106-3109.
5. See, P. and D.J. Paul, *The scaled performance of Si/Si1-xGex resonant tunneling diodes.* IEEE Electron Device Letters, 2001. 22(12): p. 582-584.
6. Kuo, Y.H., et al., *Strong quantum-confined Stark effect in germanium quantum-well structures on silicon.* Nature, 2005. 437(7063): p. 1334-1336.
7. Koester, S.J., et al., *Germanium-on-SOI Infrared Detectors for Integrated Photonic Applications.* Selected Topics in Quantum Electronics, IEEE Journal of, 2006. 12(6): p. 1489-1502.
8. Olubuyide, O.O., *Low Pressure Epitaxial Growth, Fabrication and Characterization of Ge-on-Si Photodiodes*, in *Electrical Engineering and Computer Science*. 2007, Massachusetts Institute of Technology.
9. Liu, J., et al., *Ge-on-Si laser operating at room temperature.* Optics Letters, 2010. 35(5): p. 679-681.
10. Xia, G.M., J.L. Hoyt, and M. Canonico, *Si-Ge interdiffusion in strained Si/strained SiGe heterostructures and implications for enhanced mobility metal-oxide-semiconductor field-effect transistors.* Journal of Applied Physics, 2007. 101(4): p. 044901.
11. Xia, G.R., et al., *Impact of ion implantation damage and thermal budget on mobility enhancement in strained-Si n-channel MOSFETs.* IEEE Transactions on Electron Devices, 2004. 51(12): p. 2136-2144.
12. Jung, J.W., et al., *Effect of thermal processing on mobility in strained Si/strained Si1-yGey on relaxed Si1-xGex (x < y) virtual substrates.* Applied Physics Letters, 2004. 84(17): p. 3319-3321.
13. Dehlinger, G., et al., *High-speed germanium-on-SOI lateral PIN photodiodes.* IEEE Photonics Technology Letters, 2004. 16(11): p. 2547-2549.
14. *Jifeng's personal communication*. 2010.
15. Aubertine, D.B., et al., *Observation and modeling of the initial fast interdiffusion regime in Si/SiGe multilayers.* Journal of Applied Physics, 2002. 92(9): p. 5027-5035.
16. Aubertine, D.B. and P.C. McIntyre, *Influence of Ge concentration and compressive biaxial stress on interdiffusion in Si-rich SiGe alloy heterostructures.* Journal of Applied Physics, 2005. 97(1): p. 013531.
17. Ozguven, N. and P.C. McIntyre, *Silicon-germanium interdiffusion in high-germanium-content epitaxial heterostructures.* Applied Physics Letters, 2008. 92(18): p. 181907.
18. Meduna, M., et al., *Interdiffusion in Ge rich SiGe/Ge multilayers studied by in situ diffraction.* Physica Status Solidi a-Applications and Materials Science, 2009. 206(8): p. 1775-1779.
19. Meduna, M., et al., *Interdiffusion in SiGe alloys with Ge contents of 25% and 50% studied by X-ray reflectivity.* Physica Status Solidi a-Applications and Materials Science, 2008. 205(10): p. 2441-2448.

20. Liu, X.-C. and D.R. Leadley, *Silicon-germanium interdiffusion in strained Ge/SiGe multiple quantum well structures.* Journal of Physics D-Applied Physics, 2010. 43(50): p. 055102.
21. Gavelle, M., et al., *Detailed investigation of Ge-Si interdiffusion in the full range of Si1-xGex(0 <= x <= 1) composition.* Journal of Applied Physics, 2008. 104(11): p. 113524.
22. Chen, R. and S.T. Dunham, *Kinetic lattice Monte Carlo simulations of interdiffusion in strained silicon germanium alloys.* Journal of Vacuum Science & Technology B, 2010. 28(1): p. C1G18-C1G23.
23. Castrillo, P., et al., *Physical modeling and implementation scheme of native defect diffusion and interdiffusion in SiGe heterostructures for atomistic process simulation.* Journal of Applied Physics, 2011. 109(10): p. 103502.
24. McVay, G.L. and A.R. Ducharme, *DIFFUSION OF GERMANIUM IN SILICON.* Journal of Applied Physics, 1973. 44(3): p. 1409-1410.
25. McVay, G.L. and A.R. Ducharme, *DIFFUSION OF GE IN SIGE ALLOYS.* Physical Review B, 1974. 9(2): p. 627-631.
26. Zangenberg, N.R., et al., *Ge self-diffusion in epitaxial Si1-xGex layers.* Physical Review Letters, 2001. 87(12): p. 125901.
27. Strohm, A., et al., *Self-diffusion of Ge-71 in Si-Ge.* Physica B-Condensed Matter, 2001. 308: p. 542-545.
28. Strohm, A., et al., *Self-diffusion of Ge-71 and Si-31 in Si-Ge alloys.* Zeitschrift Fur Metallkunde, 2002. 93(7): p. 737-744.
29. Kube, R., et al., *Simultaneous diffusion of Si and Ge in isotopically controlled Si1-xGex heterostructures.* Materials Science in Semiconductor Processing, 2008. 11(5-6): p. 378-383.
30. Kube, R., et al., *Composition dependence of Si and Ge diffusion in relaxed Si1-xGex alloys.* Journal of Applied Physics, 2010. 107(7): p. 073520.
31. Fischetti, M.V. and S.E. Laux, *Band structure, deformation potentials, and carrier mobility in strained Si, Ge, and SiGe alloys.* Journal of Applied Physics, 1996. 80(4): p. 2234-2252.
32. Leitz, C.W., et al., *Hole mobility enhancements and alloy scattering-limited mobility in tensile strained Si/SiGe surface channel metal–oxide–semiconductor field-effect transistors.* Journal of Applied Physics, 2002. 92(7): p. 3745-3751.
33. Currie, M.T., et al., *Carrier mobilities and process stability of strained Si n- and p-MOSFETs on SiGe virtual substrates.* Journal of Vacuum Science & Technology B, 2001. 19(6): p. 2268-2279.
34. Lin, F., et al., *Thermal stability of a Si/Si1−xGex quantum well studied by admittance spectroscopy.* Journal of Applied Physics, 2000. 87(4): p. 1947-1950.
35. Olesinski, R.W. and G.J. Abbaschian, *The Ge–Si (Germanium-Silicon) system.* Bulletin of Alloy Phase Diagrams, 1984. 5(2): p. 180-183.
36. Dismukes, J.P., L. Ekstrom, and R.J. Paff, *Lattice Parameter and Density in Germanium-Silicon Alloys1.* The Journal of Physical Chemistry, 1964. 68(10): p. 3021-3027.
37. Aziz, M.J., et al., *Pressure and stress effects on the diffusion of B and Sb in Si and Si-Ge alloys.* Physical Review B, 2006. 73(5): p. 054101.
38. Wortman, J.J. and R.A. Evans, *Young's Modulus, Shear Modulus, and Poisson's Ratio in Silicon and Germanium.* Journal of Applied Physics, 1965. 36(1): p. 153-156.
39. DeHoff, R., *Thermodynamics in Materials Science*. 2006, New York: CRC. p232.
40. Robert, W.B., Samuel, M. Allen, W. Craig, Carter, *Kinetics of Materials*. 1st ed. 2005: Wiley.
41. Mehrer, H., *Diffusion in Solids:Fundamentals, Methods, Materials, Diffusion-controlled Processes*. SOLID-STATE SCIENCES, ed. P.F. M. Cardona, K. von, Klitzing, R. Merlin, H.-J. Queisser, H.Stormer. 2007, Berlin, Heidelberg, New York: Springer.

42. Glicksman, M.E., *Diffusion in solid: Field Theory, Solid-state Principles and Applications*. 1999, New York: Wiley. 309-329.
43. Cahn, J.W., *On spinodal decomposition.* Acta Metallurgica, 1961. 9(9): p. 795-801.
44. Cook, H.E. and D. de Fontaine, *On the elastic free energy of solid solutions—I. Microscopic theory.* Acta Metallurgica, 1969. 17(7): p. 915-924.
45. Cook, H.E., D. De Fontaine, and J.e. Hilliard, *A model for diffusion on cubic lattices and its application to the early stages of ordering.* Acta Metallurgica, 1969. 17(6): p. 765-773.
46. Erdélyi, Z., et al., *On the range of validity of the continuum approach for nonlinear diffusional mixing of multilayers.* Philosophical Magazine A, 1999. 79(8): p. 1757-1768.
47. Aubertine, D.B., *An X-ray Diffraction Study of Concentration and Strain Dependent Interdiffusion in Silicon-Germanium Thin Films*, in *Materials Science and Engineering*. 2004, Stanford University.
48. Dong, Y., et al., *A unified interdiffusivity model and model verification for tensile and relaxed SiGe interdiffusion over the full germanium content range.* Journal of Applied Physics, 2012. 111(4): p. 044909.
49. Kirkendall, E.O., *Diffusion of Zinc in Alpha Brass.* Transaction AIME, 1942. 147: p. 104-110.
50. Smigelskas, A.D. and E.O. Kirkendall, *Zinc Diffusion in Alpha Brass.* Transaction AIME, 1947. 171: p. 130-142.
51. Darken, L.S., *DIFFUSION, MOBILITY AND THEIR INTERRELATION THROUGH FREE ENERGY IN BINARY METALLIC SYSTEMS.* Transactions of the American Institute of Mining and Metallurgical Engineers, 1948. 175: p. 184-201.
52. A.V. Nazarov and K.P. Gurov, Fizika Metallov Metallovedenie, 1974. 37: p. 496.
53. Colombo, L., *TIGHT-BINDING THEORY OF NATIVE POINT DEFECTS IN SILICON.* Annual Review of Materials Research, 2002. 32(1): p. 271-295.
54. Tang, M., et al., *Intrinsic point defects in crystalline silicon: Tight-binding molecular dynamics studiesof self-diffusion, interstitial-vacancy recombination, and formation volumes.* Physical Review B, 1997. 55(21): p. 14279-14289.
55. Balluffi, R.W. and J.M. Bkakely, *Special aspects of diffusion in thin films.* Thin Solid Films, 1975. 25(2): p. 363-392.
56. Hu, S.M., *Diffusion in Silicon and Germanium*, in *Atomic Diffusion in Semiconductor*, D. Shaw, Editor. 1973, Plenum Press: London and New York.
57. Blöchl, P.E., et al., *First-principles calculations of self-diffusion constants in silicon.* Physical Review Letters, 1993. 70(16): p. 2435-2438.
58. Holt, D.B. and B.G. Yacobi, *Extended Defects in Semiconductors:Electronic Properties, Device Effects and Structures*. 2007, New York: Cambridge University Press.
59. Love, G.R., *Dislocation pipe diffusion.* Acta Metallurgica, 1964. 12(6): p. 731-737.
60. Erdélyi, Z., I.A. Szabó, and D.L. Beke, *Interface Sharpening instead of Broadening by Diffusion in Ideal Binary Alloys.* Physical Review Letters, 2002. 89(16): p. 165901.
61. Van Der Merwe, J.H., *Crystal Interfaces. Part II. Finite Overgrowths.* Journal of Applied Physics, 1963. 34(1): p. 123-127.
62. Matthews, J.W. and A.E. Blakeslee, *Defects in epitaxial multilayers: I. Misfit dislocations.* Journal of Crystal Growth, 1974. 27(0): p. 118-125.
63. Leadley, D.R., et al., *Analysis of hole mobility and strain in a Si/Si 0.5 Ge 0.5 /Si metal oxide semiconductor field effect transistor.* Semiconductor Science and Technology, 2002. 17(7): p. 708.
64. People, R. and J.C. Bean, *Calculation of critical layer thickness versus lattice mismatch for GexSi1–x/Si strained ‐ layer heterostructures.* Applied Physics Letters, 1985. 47(3): p. 322-324.
65. Okada, Y. and Y. Tokumaru, *Precise determination of lattice parameter and thermal expansion coefficient of silicon between 300 and 1500 K.* Journal of Applied Physics, 1984. 56(2): p. 314-320.

66. Slack, G.A. and S.F. Bartram, *Thermal expansion of some diamondlike crystals.* Journal of Applied Physics, 1975. 46(1): p. 89-98.
67. Cowern, N.E.B., et al., *DIFFUSION IN STRAINED SI(GE).* Physical Review Letters, 1994. 72(16): p. 2585-2588.
68. Cowern, N.E.B.K., W. J. ; De Kruif, R. C. M. ;Van Berkum, J. G. M. ; De Boer, W. B.;Gravesteijn, D. J. and Bulle-Liewma C. W. T. , *Interdiffusion Mechanisms in Coherently strained SiGe Multilayers.* 1996: p. 195.
69. Kasper, E. and S. Heim, *Challenges of high Ge content silicon germanium structures.* Applied Surface Science, 2004. 224(1–4): p. 3-8.
70. Parsons, J., et al., *Relaxation of strained silicon on Si(0.5)Ge(0.5) virtual substrates.* Applied Physics Letters, 2008. 93(7): p. 072108.
71. Samavedam, S.B., et al., *Relaxation of strained Si layers grown on SiGe buffers.* Journal of Vacuum Science & Technology B, 1999. 17(4): p. 1424-1429.
72. Welser, J., J.L. Hoyt, and J.F. Gibbons, *Electron mobility enhancement in strained-Si n-type metal-oxide-semiconductor field-effect transistors.* Electron Device Letters, IEEE, 1994. 15(3): p. 100-102.
73. Leitz, C.W., *High Mobility Strained Si/SiGe Heterostructure MOSFETs:Channel Engineering and Virtual Substrate Optimization*, in *Materials Science and Engineering*. 2002, Massachusetts Institute of Technology.
74. MacKnight, R.B., et al. *RTP application and technology options for the sub-45 nm nodes*. in *Advanced Thermal Processing of Semiconductors, 2004. RTP 2004. 12th IEEE International Conference on*. 2004.
75. Le Royer, C., et al. *High Performance FDSOI MOSFETs and TFETs Using SiGe Channels and Raised Source and Drain*. in *Silicon-Germanium Technology and Device Meeting (ISTDM), 2012 International*. 2012.
76. Witters, L., et al., *8 angstrom Tinv Gate-First Dual Channel Technology Achieving Low-V(t) High Performance CMOS*. 2010 Symposium on Vlsi Technology, Digest of Technical Papers. 2010. 181-182.
77. Munkang, C., et al. *14 nm FinFET Stress Engineering with Epitaxial SiGe Source/Drain*. in *Silicon-Germanium Technology and Device Meeting (ISTDM), 2012 International*. 2012.
78. Morin, P., et al., *Managing annealing pattern effects in 45 nm low power CMOS technology.* Solid-State Electronics, 2010. 54(9): p. 897-902.
79. Xia, G. and J.L. Hoyt, *Si-Ge interdiffusion under oxidizing conditions in epitaxial SiGe heterostructures with high compressive stress.* Applied Physics Letters, 2010. 96(12): p. 122107.
80. Vickerman, J.C., *Secondary ion mass spectrometry–basic concepts, instrumental aspects, applications and trends. A. BENNINGHOVEN, F. G. RUDENAUER and H. W. WERNER, Wiley, New York, 1987, 1277 pages.* Surface and Interface Analysis, 1987. 10(8): p. 435-435.
81. Tsaur, B.Y., Z.L. Liau, and J.W. Mayer, *Ion‐beam‐induced silicide formation.* Applied Physics Letters, 1979. 34(2): p. 168-170.
82. Ishitani, T. and R. Shimizu, *Computer simulation of atomic mixing during ion bombardment.* Applied physics, 1975. 6(2): p. 241-248.
83. Sánchez-Almazán, F., et al., *Matrix effects in SIMS depth profiles of SiGe relaxed buffer layers.* Applied Surface Science, 2004. 231–232(0): p. 704-707.
84. Zalm, P.C., et al., *Facts and artefacts in the characterization of Si/SiGe multiayers with SIMS.* Surface and Interface Analysis, 1991. 17(8): p. 556-566.
85. Jackman, J.A., et al., *Matrix effects in sims depth profiles of SiGe superlattices.* Nuclear Instruments and Methods in Physics Research Section B: Beam Interactions with Materials and Atoms, 1990. 45(1–4): p. 592-596.

86. Jiang, Z.X., et al., *Quantitative SIMS analysis of SiGe composition with low energy O2+ beams.* Applied Surface Science, 2006. 252(19): p. 7262-7264.
87. Ehrke, H.U. and H. Maul, *Quantification of Ge and B in SiGe using secondary ion mass spectrometry.* Materials Science in Semiconductor Processing, 2005. 8(1–3): p. 111-114.
88. Perova, T.S., et al., *Composition and strain in thin Si1−xGex virtual substrates measured by micro-Raman spectroscopy and x-ray diffraction.* Journal of Applied Physics, 2011. 109(3): p. 033502.
89. Hollander, B., R. Butz, and S. Mantl, *INTERDIFFUSION AND THERMALLY INDUCED STRAIN RELAXATION IN STRAINED SI1-XGEX/SI SUPERLATTICES.* Physical Review B, 1992. 46(11): p. 6975-6981.
90. Pezzoli, F., et al., *Strain-induced shift of phonon modes in alloys.* Materials Science in Semiconductor Processing, 2006. 9(4–5): p. 541-545.
91. Pezzoli, F., et al., *Raman spectroscopy determination of composition and strain in heterostructures.* Materials Science in Semiconductor Processing, 2008. 11(5–6): p. 279-284.
92. Dietrich, B., et al., *Measurement of stress and relaxation in Si1−xGex layers by Raman line shift and x‐ray diffraction.* Journal of Applied Physics, 1993. 74(5): p. 3177-3180.
93. Rath, S., et al., *Alloy effects on the Raman spectra of Si 1− x Ge x and calibration protocols for alloy compositions based on polarization measurements.* Semiconductor Science and Technology, 2003. 18(6): p. 566.
94. Shin, H.K., D.J. Lockwood, and J.M. Baribeau, *Strain in coherent-wave SiGe/Si superlattices.* Solid State Communications, 2000. 114(10): p. 505-510.
95. Milekhin, A.G., et al., *Size-selective Raman scattering in self-assembled Ge/Si quantum dot superlattices.* Nanotechnology, 2002. 13(1): p. 55.
96. Sui, Z., H.H. Burke, and I.P. Herman, *Raman scattering in germanium-silicon alloys under hydrostatic pressure.* Physical Review B, 1993. 48(4): p. 2162-2168.
97. Wolf, I.D., *Micro-Raman spectroscopy to study local mechanical stress in silicon integrated circuits.* Semiconductor Science and Technology, 1996. 11(2): p. 139.
98. Wermelinger, T. and R. Spolenak, *Stress Analysis by Means of Raman Microscopy*, in *Confocal Raman Microscopy*, T. Dieing, O. Hollricher, and J. Toporski, Editors. 2011, Springer Berlin Heidelberg. p. 259-278.
99. Anastassakis, E., et al., *Effect of static uniaxial stress on the Raman spectrum of silicon.* Solid State Communications, 1970. 8(2): p. 133-138.
100. Chandrasekhar, M., J.B. Renucci, and M. Cardona, *Effects of interband excitations on Raman phonons in heavily doped n-Si.* Physical Review B, 1978. 17(4): p. 1623-1633.
101. Anastassakis, E., A. Cantarero, and M. Cardona, *Piezo-Raman measurements and anharmonic parameters in silicon and diamond.* Physical Review B, 1990. 41(11): p. 7529-7535.
102. Nakashima, S., et al., *Raman investigation of strain in Si／SiGe heterostructures: Precise determination of the strain-shift coefficient of Si bands.* Journal of Applied Physics, 2006. 99(5): p. 053512.
103. Zhylik, A., et al., *High-resolution x-ray diffraction investigation of relaxation and dislocations in SiGe layers grown on (001), (011), and (111) Si substrates.* Journal of Applied Physics, 2011. 109(12): p. 123714.
104. D.Keith Bowen, B.K.T., *High Resolution X-ray Diffractometry and Topography*. 1998, Bristol, PA: Taylor&Francis.
105. Csiszar, S.I., *X-ray Diffraction and X-ray absorption of strained CoO and MnO thin films*, in *Mathematics and Natural Sciences*. 2005, University of Groningen: Netherlands.

106. Mooney, P.M. and J.L. Jordan-Sweet, *High Resolution X-ray Diffraction Applied to Strain Relaxation of Lattice Mismatched Semiconductor Films.* JCPDS-International Centre for Diffraction Data, 1999.
107. Konya, T., *X-ray thin film measurement techniques III. High Resolution X-ray Diffractometry.* The Rigaku Journal, 2009. 25(2): p. 1-8.
108. Franssila, S., *Introduction to Microfabrication*. Second ed. 2010, United Kindom: John Wiley&Sons. 534.
109. Sieg, R.M., et al., *Anti-phase domain-free growth of GaAs on offcut (001) Ge wafers by molecular beam epitaxy with suppressed Ge outdiffusion.* Journal of Electronic Materials, 1998. 27(7): p. 900-907.
110. Mooney, P.M., et al., *Nucleation of dislocations in SiGe layers grown on (001)Si.* Journal of Applied Physics, 1994. 75(8): p. 3968-3977.
111. Mooney P M, J.-S.J.L., Stephenson G B, LeGoues F K and Chu J O. *High Resolution X-ray Diffraction Measurements of Strain Relaxed SiGe/Si Structures*. in *Advances in X-Ray Analysis, 38: 43rd Annual Denver X-Ray Conference on application of X-Ray analysis*. 1995.
112. Williams, D. and C.B. Carter, *Thinking in Reciprocal Space*, in *Transmission Electron Microscopy*. 2009, Springer US. p. 211-219.
113. Ewald, P., *Introduction to the dynamical theory of X-ray diffraction.* Acta Crystallographica Section A, 1969. 25(1): p. 103-108.
114. *Guide files in Epitaxy Software*.
115. Lin, H., et al., *X-ray diffraction analysis of step-graded InxGa1−xAs buffer layers grown by molecular beam epitaxy.* Journal of Crystal Growth, 2011. 323(1): p. 17-20.
116. Lin, H., *GROWTH AND CHARACTERIZATION OF GeSn AND SiGeSn ALLOYS FOR OPTICAL INTERCONNECTS*, in *Materials Science and Engineering*. 2012, STANFORD UNIVERSITY.
117. Atici, Y., *Study of threading dislocations in the plan-view sample of SiGe/Si(001) superlattices by transmission electron microscopy.* Journal of Electronic Materials, 2005. 34(5): p. 612-616.
118. Neily, S., et al., *On triple dislocation nodes observed by TEM in a Ge0.4Si0.6 film grown on a slightly deviating (0 0 1)Si substrate.* Philosophical Magazine Letters, 2011. 91(8): p. 510-515.
119. Hsu, J.W.P., et al., *Surface morphology of related GexSi1−x films.* Applied Physics Letters, 1992. 61(11): p. 1293-1295.
120. Luo, Y.H., et al., *Compliant effect of low-temperature Si buffer for SiGe growth.* Applied Physics Letters, 2001. 78(4): p. 454-456.
121. Kim, M., *Limited-Area Growth of Ge and SiGe on Si*, in *Materials Science and Engineering*. 2011, Massachusetts Institute of Technology.
122. Gupta, S., *Substrate and Channel Engineering for Improving Performance of Strained-SiGe MOSFETs*, in *Materials Science and Engineering*. 2006, Massachusetts Institute of Technology.
123. Ishida, K., Masahiro Akiyama, and S. Nidhi., *Misfit and treading dislocations in GaAs layers grown on Si substrates by MOCVD.* Jpn J Appl Phys, 1987. 26: p. L163-L165.
124. Shimizu, M., et al., *Dislocation-density studies in MOCVD GaAs on Si substrates.* Journal of Crystal Growth, 1988. 93(1–4): p. 475-480.
125. Stirland, D.J., G.J. Rees, and A. Ritson, *The relationship between etch pit density and dislocation density for (001)GaAs.* Journal of Crystal Growth, 1986. 79(1–3): p. 493-502.
126. Stirland, D.J., *Quantitative defect etching of GaAs on Si: Is it possible?* Applied Physics Letters, 1988. 53(24): p. 2432-2434.
127. Werner, J., K. Lyutovich, and C.P. Parry, *Defect imaging in ultra-thin SiGe (100) strain relaxed buffers.* The European Physical Journal - Applied Physics, 2004. 27(1-3): p. 367-370.
128. Griglione, M., et al., *Diffusion of Ge in Si1-xGex/Si single quantum wells in inert and oxidizing ambients.* Journal of Applied Physics, 2000. 88(3): p. 1366-1372.

129. Iyer, S.S. and F.K. Legoues, *THERMAL RELAXATION OF PSEUDOMORPHIC SI-GE SUPERLATTICES BY ENHANCED DIFFUSION AND DISLOCATION MULTIPLICATION.* Journal of Applied Physics, 1989. 65(12): p. 4693-4698.
130. Baribeau, J.M., *X-RAY REFLECTOMETRY STUDY OF INTERDIFFUSION IN SI/GE HETEROSTRUCTURES.* Journal of Applied Physics, 1993. 74(6): p. 3805-3810.
131. Baribeau, J.M., *X-ray scattering analysis of interface roughness and diffusion.* Journal of Vacuum Science & Technology B, 1998. 16(3): p. 1568-1574.
132. Prokes, S.M., O.J. Glembocki, and D.J. Godbey, *STRESS AND ITS EFFECT ON THE INTERDIFFUSION IN SI1-XGEX/SI SUPERLATTICES.* Applied Physics Letters, 1992. 60(9): p. 1087-1089.
133. Prokes, S.M. and K.L. Wang, *INTERDIFFUSION MEASUREMENTS IN ASYMMETRICALLY STRAINED SIGE/SI SUPERLATTICES.* Applied Physics Letters, 1990. 56(26): p. 2628-2630.
134. Schorer, R., et al., *STRUCTURAL STABILITY OF SHORT-PERIOD SI/GE SUPERLATTICES STUDIED WITH RAMAN-SPECTROSCOPY.* Physical Review B, 1991. 44(4): p. 1772-1781.
135. Boucaud, P., et al., *Photoluminescence and intersubband absorption spectroscopy of interdiffused Si/SiGe quantum wells.* Journal of Applied Physics, 1996. 80(3): p. 1414-1421.
136. Shaw, D., *SELF-DIFFUSION AND IMPURITY DIFFUSION IN GE AND SI.* Physica Status Solidi B-Basic Research, 1975. 72(1): p. 11-39.
137. Borg, R.J. and G.J. Dienes, *An Introduction to Solid State Diffusion*. 1988, San Diego: Academic. pp53-73.
138. Bublik, V.T., et al., *DIFFUSE X-RAY DETERMINATION OF ENERGY OF MIXING AND ELASTIC-CONSTANTS OF GE-SI SOLID-SOLUTIONS.* Physica Status Solidi B-Basic Research, 1974. 66(2): p. 427-432.
139. *TSUPREM-4TM*. 2007, Synopsys, Inc.: Mountain View, CA.
140. Theiss, S.D., F. Spaepen, and M.J. Aziz, *Pressure‐enhanced interdiffusion in amorphous Si/Ge multilayers.* Applied Physics Letters, 1996. 68(9): p. 1226-1228.
141. Gillin, W.P. and D.J. Dunstan, *Strain and interdiffusion in semiconductor heterostructures.* Physical Review B, 1994. 50(11): p. 7495-7498.
142. Cahn, J.W. and J.E. Hilliard, *Free Energy of a Nonuniform System. I. Interfacial Free Energy.* The Journal of Chemical Physics, 1958. 28(2): p. 258-267.
143. Cook, H.E. and D. De Fontaine, *On the elastic free energy of solid solutions—II. Influence of the effective modulus on precipitation from solution and the order-disorder reaction.* Acta Metallurgica, 1971. 19(7): p. 607-616.
144. Greer, A.L. and F. Spaepen, *Synthetic Modulated Structures*, ed. L.L. Chang and B.C. Giesson. 1985, Orlando: Academic Press.
145. Aziz, M.J., *Thermodynamics of diffusion under pressure and stress: Relation to point defect mechanisms.* Applied Physics Letters, 1997. 70(21): p. 2810-2812.
146. Caliste, D., K.Z. Rushchanskii, and P. Pochet, *Vacancy-mediated diffusion in biaxially strained Si.* Applied Physics Letters, 2011. 98(3): p. 031908.
147. Fahey, P.M., P.B. Griffin, and J.D. Plummer, *Point defects and dopant diffusion in silicon.* Reviews of Modern Physics, 1989. 61(2): p. 289-384.
148. Ural, A., P.B. Griffin, and J.D. Plummer, *Self-Diffusion in Silicon: Similarity between the Properties of Native Point Defects.* Physical Review Letters, 1999. 83(17): p. 3454-3457.
149. Hasanuzzaman, M. and Y. Haddara, *Modeling silicon–germanium interdiffusion by the vacancy exchange and interstitial mechanisms.* Journal of Materials Science: Materials in Electronics, 2008. 19(6): p. 569-576.
150. Hasanuzzaman, M., Y.M. Haddara, and A.P. Knights, *Modeling germanium diffusion in Si1−xGex/Si superlattice structures.* Journal of Applied Physics, 2009. 105(4): p. 043504.

151. Laitinen, P., et al., *Self-Diffusion of Si-31 and Ge-71 in Relaxed Si0.20Ge0.80 Layers.* Physical Review Letters, 2002. 89(8): p. 085902.
152. Silvestri, H.H., et al., *Diffusion of silicon in crystalline germanium.* Semiconductor Science and Technology, 2006. 21(6): p. 758.
153. Castrillo, P., et al., *Atomistic modeling of defect diffusion and interdiffusion in SiGe heterostructures.* Thin Solid Films, 2010. 518(9): p. 2448-2453.
154. Hartmann, J.M., A. Abbadie, and S. Favier, *Critical thickness for plastic relaxation of SiGe on Si(001) revisited.* Journal of Applied Physics, 2011. 110(8): p. 083529.
155. Da, Z., T. White, and B.-y. Nguyen, *Embedded Source/Drain SiGe Stressor Devices on SOI: Integrations, Performance, and Analyses.* Electron Devices, IEEE Transactions on, 2006. 53(12): p. 3020-3024.
156. Wong, C.P., et al., *Impact of Implantation and Annealing on Channel Strain of Transistors with Embedded Silicon-Germanium Source and Drain.* Japanese Journal of Applied Physics, 2011. 50: p. 040208.
157. Dunstan, D.J., *Strain and strain relaxation in semiconductors.* Journal of Materials Science: Materials in Electronics, 1997. 8(6): p. 337-375.
158. Bean, J.C., et al., *GexSi1−x/Si strained ‐ layer superlattice grown by molecular beam epitaxy.* Journal of Vacuum Science & Technology A, 1984. 2(2): p. 436-440.
159. Leitz, C.W., et al., *Dislocation glide and blocking kinetics in compositionally graded SiGe/Si.* Journal of Applied Physics, 2001. 90(6): p. 2730-2736.
160. Fischer, A., et al., *Strain and surface phenomena in SiGe structures.* Physical Review B, 1996. 54(12): p. 8761-8768.
161. Gillard, V.T., W.D. Nix, and L.B. Freund, *Role of dislocation blocking in limiting strain relaxation in heteroepitaxial films.* Journal of Applied Physics, 1994. 76(11): p. 7280-7287.
162. Fischer, G.G. and P. Zaumseil, *In situ X-ray investigation of the high-temperature behaviour of strained Si 1-x Ge x /Si and Si 1-y C y /Si heterostructures.* Journal of Physics D: Applied Physics, 1995. 28(4A): p. A109.
163. Fischer, G.G. and P. Zaumseil, *Simulation of the Process of Strain Relaxation in Si1—xGex/Si(100) Heterostructures.* physica status solidi (a), 1997. 164(2): p. 767-778.
164. Stach, E.A., et al., *In-situ transmission electron microscopy studies of the interaction between dislocations in strained SiGe/Si (001) heterostructures.* Philosophical Magazine A, 2000. 80(9): p. 2159-2200.
165. Vdovin, V.I., et al., *Thermally induced strain relaxation in SiGe/Si heterostructures with low-temperature buffer layers.* physica status solidi (c), 2005. 2(6): p. 1938-1942.
166. Yugova, T.G., et al., *Thermally stimulated relaxation of misfit strains in Si1−x Gex/Si(100) heterostructures with different buffer layers.* Crystallography Reports, 2005. 50(6): p. 1020-1026.

Appendices

Appendix A: Overview of the simulation implement in TSUPREM-4™

TSUPREM-4™ is an industry mainstream two-dimension (2-D) finite element simulation tool for simulating the processing used in the manufacture of silicon integrated circuits. TSUPREM-4™ simulates the incorporation and redistribution of impurities in a 2-D device cross-section perpendicular to the surface of the silicon wafer. TSUPREM-4™ can model typical processing steps for device fabrications, such ion implantation, diffusion, silicon oxidation and silicidation, epitaxial growth of various materials and etching of these materials. In this work, we have used TSUPREM-4™ to simulate Si-Ge interdiffusion in SiGe heterostructures. Here an overview of the simulation implement in TSUPREM-4™ is given.

First, the SIMS data need to be incorporated into TSUPREM-4™. The as-grown SIMS data work as the initial condition of Ge concentration distribution for the partial derivative equation of Fick's second law. The SIMS data after anneals are used for comparisons with the simulation predictions.

Second, a grid structure is defined and generated, because the continuous diffusion processes are numerically modeled by using finite element solution techniques. A nonuniform rectangular grid is specified by means of the "**line**" statements in this work, and then it is converted to a triangular grid by adding diagonals automatically. The "**line**" statement is used to specify a series of grid lines. The location of each line is given by the "**location**" parameter, and the spacing between lines is specified with the optional "**spacing**" parameter (see the line statements of the TSUPREM-4™ code as follows). For the user-specified grid lines, the "spacing" is specified for line i on the "line" statement, and the real spacing is given by h_i = $spacing \times grid.fac$, where $grid.fac$ is a unitless factor by which all grid spacing specifications

are multiplied. Due to the one-dimension diffusion in this work, we need to define a fine mesh along the diffusion direction y (in the main text of this thesis, z is used to denote this direction) while the x direction has a coarse mesh, as shown in Figure A1. The mesh is much finer at the interdiffusion region of interest than at Si substrate for better accuracy. In addition, the adaptive gridding (both refinement and unrefinement) during diffusion is disabled to make sure that the diffusion simulation is not influenced by the automatical adaptive gridding.

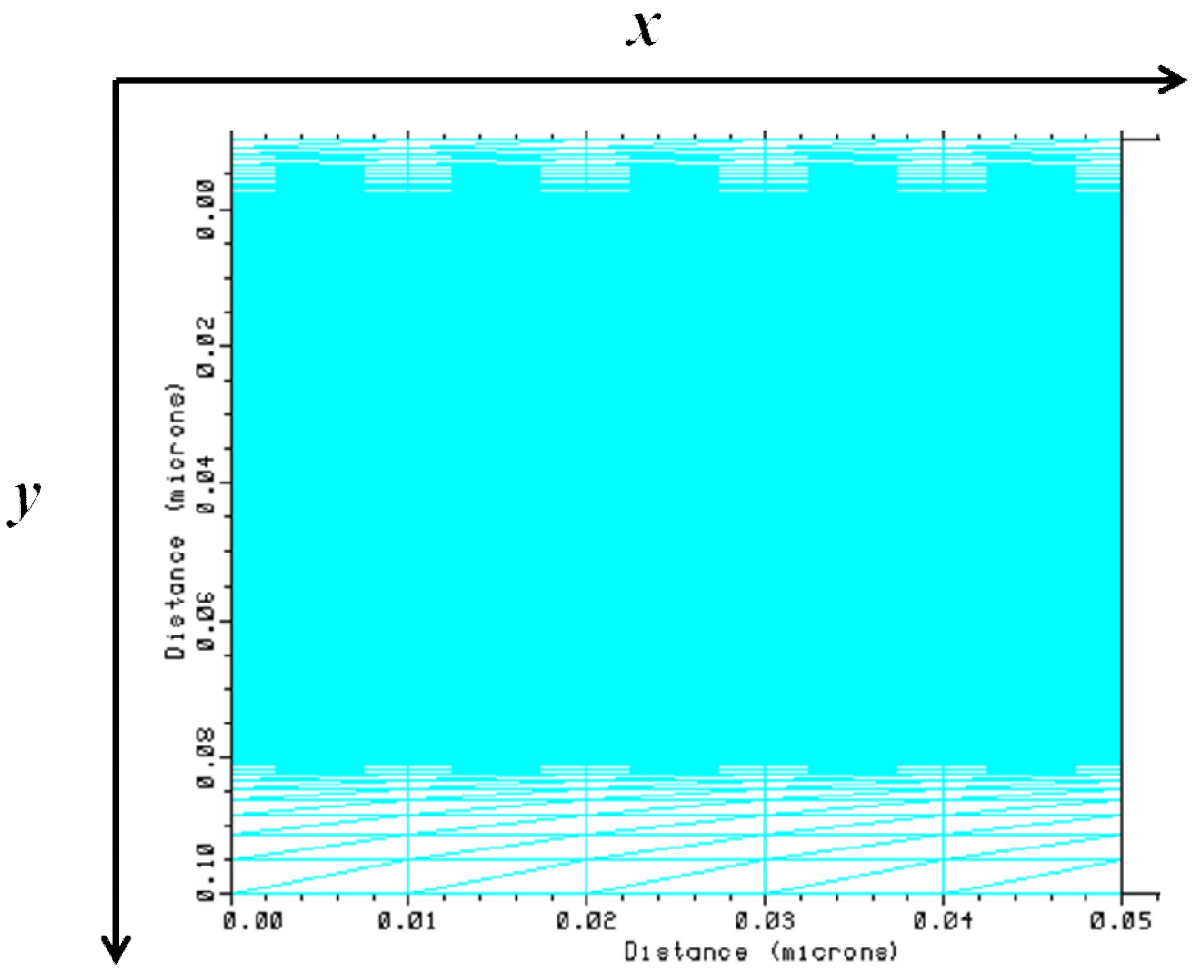

Figure A1 Definition and generation of the grid for diffusion simulation.

Third, the Ge atoms are defined as a new impurity in TSUPREM-4^{TM}, and then we can define the interdiffusivity models in this work for the Ge flux. Then, the temperature and time of thermal

anneals are defined by the command “diffusion”. With the initial Ge concentration profiles and constant boundary conditions, the partial derivative equation of Fick’s second law can be solved with the finite element solution technique in TSUPREM-4^{TM} automatically.

At last, the Ge concentration distribution after anneals can be extracted from each node, and can be plotted out for the comparison with experimental data.

All the simulations are implemented in TSUPREM-4^{TM} with the model established in Chapter 4 to 6. The codes of the modeling in TSUPREM-4^{TM} are shown as follows:

$$ This code is to extract the strain enhancing factor based on the new model

$$ it takes as-grown SIMS data as input, simulates and compares annealed data vs. model prediction

$$ Set the filenames and annealing parameters

assign name=T n.val=760

assign name=time n.val=40

assign name=XgeVirtualSubstrate n.val=0.357

$$ As-grown and annealed SIMS data files for S4065

assign name=InputFile c.val= “S4065_asgrown_SIMS.txt”

assign name=DataAnnealed c.val= “S4065SIMS_760C40mins.txt”

assign name=DataAnnealed c.val= “S4065SIMS_800C40mins.txt”

assign name=DataAnnealed c.val= “S4065SIMS_840C40mins.txt”

assign name=DataAnnealed c.val= “S4065SIMS_880C40mins.txt”

$$ As-grown and annealed SIMS data files for S5075

assign name=InputFile c.val= “S5075_asgrown_SIMS.txt”

assign name=DataAnnealed c.val= “S5075SIMS_720C40mins.txt”

assign name=DataAnnealed c.val= “S5075SIMS_760C40mins.txt”

assign name=DataAnnealed c.val= “S5075SIMS_800C40mins.txt”

assign name=DataAnnealed c.val= “S5075SIMS_840C40mins.txt”

$$ As-grown and annealed SIMS data files for S4585

assign name=InputFile c.val= “S4585_asgrown_SIMS.txt”

assign name=DataAnnealed c.val= "S4585SIMS_760C40mins.txt"

assign name=DataAnnealed c.val= "S4585SIMS_800C10mins.txt"

assign name=DataAnnealed c.val= "S4585SIMS_800C20mins.txt"

assign name=DataAnnealed c.val= "S4585SIMS_800C40mins.txt"

assign name=DataAnnealed c.val= "S4585SIMS_840C40mins.txt"

$$ mesh setting up

line x loc=0 spacing=0.01

line x loc=0.01 spacing=0.01

line y loc=-0.01 spacing=0.001

line y loc=0.00 spacing=0.0001

line y loc=0.005 spacing=0.0001

line y loc=0.012 spacing=0.0001

line y loc=0.050 spacing=0.0001

line y loc=0.0800 spacing=0.0001

line y loc=0.1000 spacing=0.001

line y loc=0.2000 spacing=0.0100

line y loc=0.450 spacing=0.100

init boron=5e14 material=silicon

$$define Ge diffusion and method employed in the simulation

impurity name=Ge new

method variable=Ge none abs.err=0.1 ^dif.adap

$$ disable diffusion adapative griding

profile impurity=Ge inf=@Inputfile

$$modeling setup to extract strain derivative q'

$$atomic concentration is translated into Ge fraction

intermed name=Yge express=Ge/1e22

*intermed name=Xge express=(5-sqrt(25-2.32*Yge))/1.16*

intermed name=Xge0 value=@XgeVirtualSubstrate

$$the expression of the strain derivative q'

*intermed name=b2 value=0.0418*q/kT*

$$parameters of Ge and Si self diffusivities

intermed name=Ta express=273.15+@T

intermed name=Rgas value=8.314

*intermed name=D0si express=exp(6.489+4.9641*Xge-7.8285*Xge*Xge)*

intermed name=DEsi express=exp(-((4.76(1-Xge)+3.32*Xge+1.54*(1-Xge)*Xge))/kT)*

*intermed name=D0ge express=exp(6.636+8.028*Xge-11.318*Xge*Xge)*

*intermed name=DEge express=exp(-(((1-Xge)*4.83+3.13*Xge+1.63*(1-Xge)*Xge))/kT)*

intermed name=Xs express=1-Xge

*intermed name=Fsia express=(4017*Xge-17574)/Ta/Rgas*

*intermed name=Fgea express=(4017*Xge-18913)/Ta/Rgas*

*intermed name=Fsi express=Xs*Xge*Fsia*

*intermed name=Fge express=Xs*Xge*Fgea*

$$Si-Ge interdiffusivity without strain

*intermed name=Did express=(1-Xge)*D0ge*DEge*(1+Fge)+Xge*D0si*DEsi*(1+Fsi)*

$$the relaxation R

intermed name=R value=0

intermed name=Rmi express=1-R

$$strain term contributes to the driving force

intermed name=Vmol express=13e-6

*intermed name=foo express=(Rgas*Ta/(Xge*(1-Xge))-17574+2678*Xge)/Vmol*

intermed name=Yng express=120e9(1-Xge)+91.3e9*Xge*

intermed name=Vpoi express=0.264(1-Xge)+0.251*Xge*

intermed name=M2d express=Yng/(1-Vpoi)

*intermed name=Sdri express=2*0.0418*0.0418*M2d*Rmi*Rmi/foo*

$$Si-Ge interdiffusivity under full coherent strain (R=0)

*intermed name=D express=(1+Sdri)*Did*exp(b2*Rmi*(Xge-Xge0))*

$$Fick's second law

equation variable=Ge mat=Si +

*addtoexp=DIV(D*GRAD(Ge))*

$$thermal budgets of anneals

$$ramp up process of thermal annealing

Diffusion time=(@T-25)/40 temp=25 t.final=@T inert

$$steady state of thermal annealing

diffusion time=@time temp=@T inert

$$ ramp down process of thermal annealing

Diffusion time=(@T-25)/100 temp=@T t.final=25 inert

$$plot the simulation profile of Ge

sel z=Ge

plot.1 ^axis ^clear color=2 line.typ=1 symbol=1 ^curve

$$save the simulation data in .txt file

if ("@save"=="Y")

SELECT Z=Ge

EXTRACT OUT.FILE=ZZS5075dong760T40Minnew_1218.txt +

PREFIX="% Ge profile simulated"

FOREACH DEPTH (0 TO 0.12 STEP 0.0001)

EXTRACT SILICON X=0.005 DISTANCE=@(DEPTH) Y.EXT VAL.EXT

END

EXTRACT CLOSE

if.end

stop

Appendix B: Impact of the ramp-up and ramp-down processes on interdiffusion simulation

This appendix shows the comparisons between simulations with and without the thermal budget during the temperature ramp-up and ramp down processes for S4065 and S5075, in Figure B1. From Figure B1, it is demonstrated that the simulated curves with and without the thermal budget during the temperature ramp-up and ramp down processes are almost overlapped with each other. The impact of these thermal budget is negligible for the extraction of the strain derivative q' of interdiffusivity in Chapter 5. Moreover, in Chapter 6, it is directly proved by the SIMS measurements that there is little interdiffusion during the temperature ramp-up and ramp-down processes, shown in Figure 6.8.

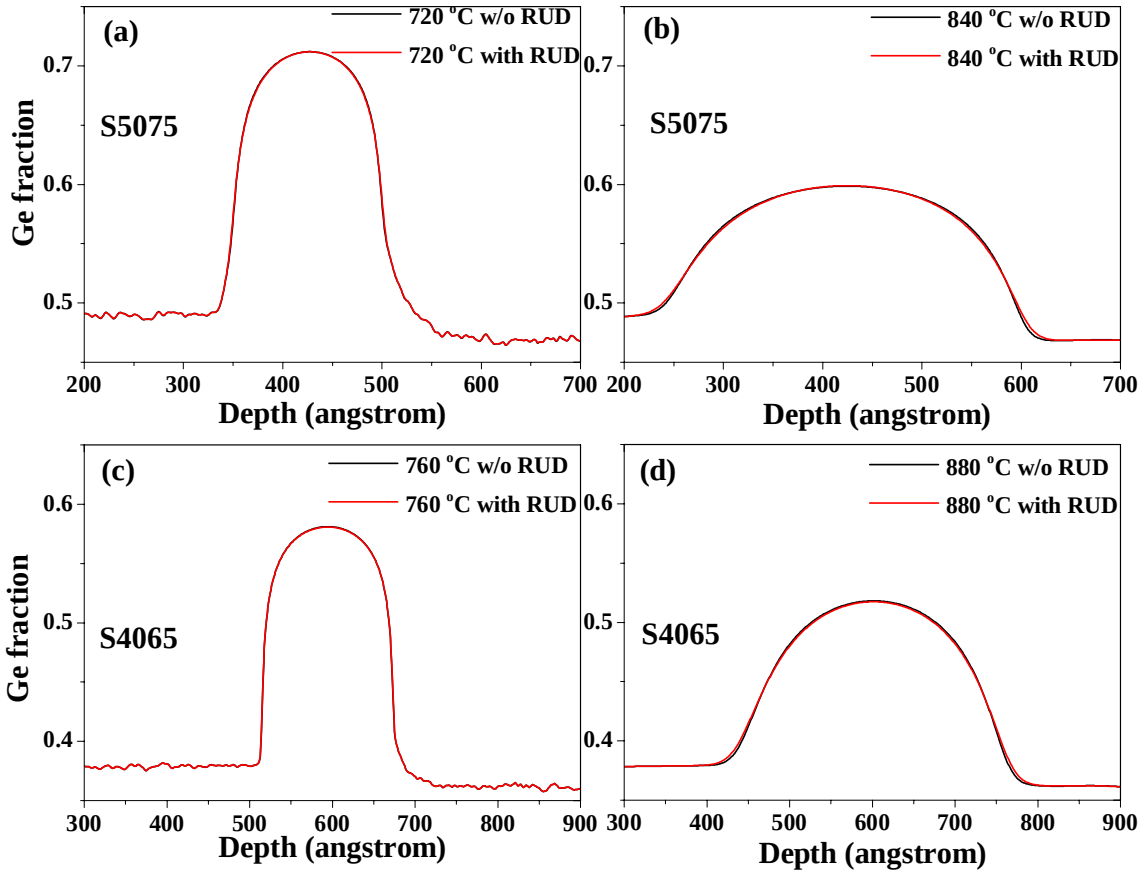

Figure B1 The comparisons between simulations with and without temperature ramp-up ad –down processes (RUD): (a) at 720 °C for S5075; (b) at 840 °C for S5075; (c) at 760 °C for S4065; (d) at 880 °C for S4065.

Appendix C: Simulation procedure in software Epitaxy

Epitaxy is a part of PANalytical's software package, which provides functionality for plotting and analyzing high-resolution X-ray diffraction data of rocking curves, 2-axes scans, reciprocal space maps and wafer maps. Epitaxy offers a wealth of key information on thin heteroepitaxial layers, particularly single-crystal and highly textured thin-layer samples, such as lattice mismatch and relaxation, composition and layer thickness.

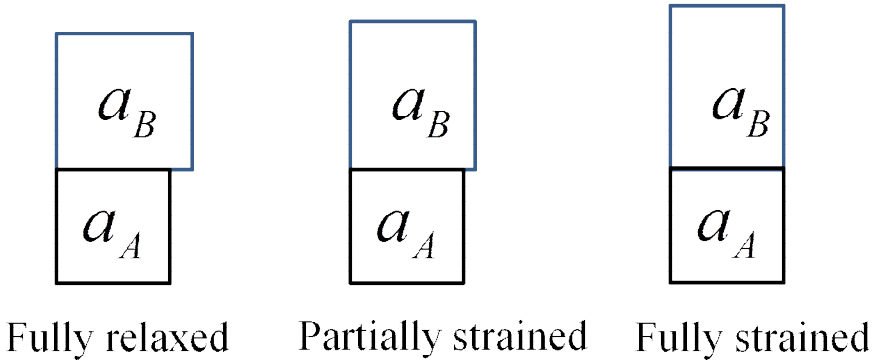

Figure C1 Three typical scenarios of mismatch strain between two layers with a cubic crystalline structure. The lattice parameter of B is larger than that of A, $a_B > a_A$.

In Epitaxy, the relaxation R is used to model the change in the unit cell distortion that occurs in the imperfect interfaces, which occur when misfit dislocations are present. This parameter is used to calculate the correct peak positions in simulated rocking curves. Let's first see the three types of the scenarios of mismatch strain between two layers with a cubic crystalline structure: fully relaxed, partially strained and fully strained, shown in Figure C1. For the fully relaxed case (R=100%), the B layer is undistorted (as bulk), so the unit cells of the A and B layers are a square in a two-dimension cross section view. For the fully strained case (R=0), the B layer is elastically distorted such that the unit cells have the same in-plane lattice parameter, and the interface does not contain misfit dislocations. For the partially strained case (0<R<100%), the B

layer is distorted, but its in-plane lattice parameter is larger than that of the A layer while smaller that of bulk B. In addition, misfit dislocations exist at the interface.

For a multi-layered epitaxial structure with different R values in each layer, an iteration method is employed to define the R values, shown in Equation C1. Figure C2 shows how the relaxation is defined for the interface between any two layers: layer N and layer (N+1). [114]

$$R_{N+1} = \frac{a^*_{N+1} - a^*_N}{a_{N+1} - a^*_N} \times 100\% \qquad \text{C1}$$

where a^*_N and a^*_{N+1} are the in-plane lattice parameters of layer N and layer N+1 with partial strain relaxation, and a_{N+1} is the in-plane lattice parameter of layer N+1 with full strain relaxation.

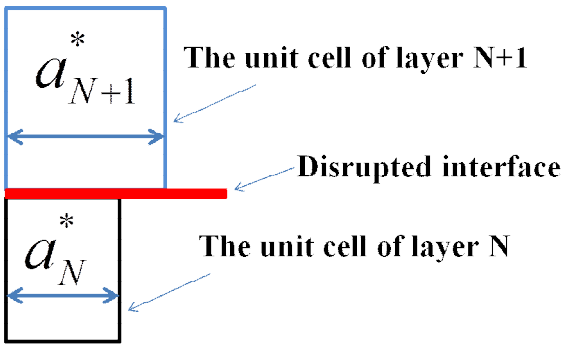

Figure C2 Schematic structure of two layers with partial strain relaxation: layer N+1 and layer N. Strain is relaxed via misfit dislocations at the interface.

In this work, Epitaxy is employed to do the rocking curve analysis for the three samples (S4065, S5075 and S4585). The information of Ge composition and strain relaxation in the compressive layers can be derived from a set of four scans, including two symmetric scans and two asymmetric scans at phi=0° and 180°. The simulation procedure is shown as follows.

First, based on the peak positions from XRD scans at phi=0° and 180°, the apparent miscut and tilt angles can be calculated by Equation 3.18 and 3.19 in Chapter 3, or measured directly with the software, Epitaxy. The average peak positions (relative to the substrate peak) without tilt impact can be calculated by Equation 3.20, or measured directly with Epitaxy for compressive $Si_{1-y}Ge_y$ layers and bottom $Si_{1-x}Ge_x$ layers, shown in Figure C3.

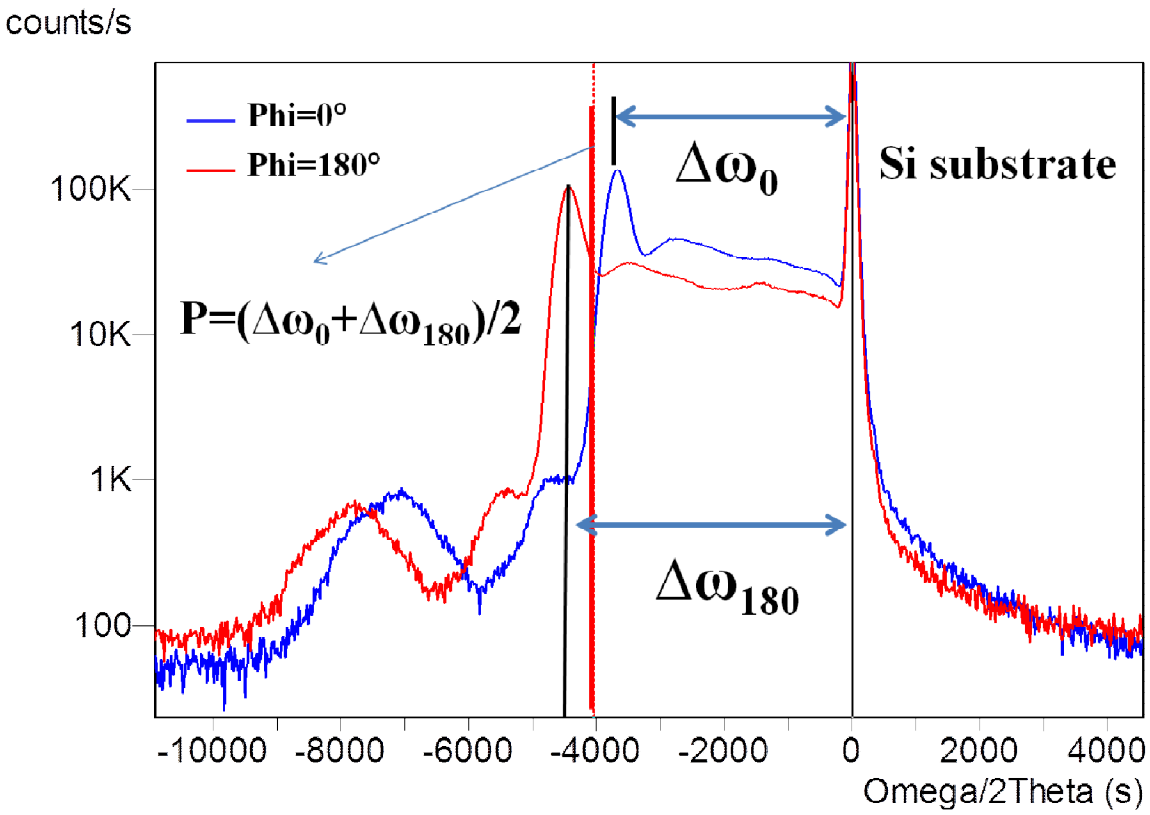

Figure C3 Schematic diagram to show how to calculate the average peak position (denoted by P) without tilt impact, $P = (\Delta\omega_0 + \Delta\omega_{180})/2$, from the two scans at Phi=0° and 180°.

Second, by matching the simulation peaks with the accurate peak positions (relative to the substrate peak) in Epitaxy, the information of strain and Ge fraction can be extracted for the compressive $Si_{1-y}Ge_y$ and bottom $Si_{1-x}Ge_x$ layers. For the simulations in Epitaxy, an identical multilayered structure as the real sample is built, shown in Figure C4. The thick graded buffer is not included, because there is no difference in the simulation without this layer. There are two

key parameters (R and Ge fraction) for each layer to decide the peak positions in Epitaxy simulations. Tens of different combinations of R and Ge fraction are tried during peak matching to obtain the R value and Ge fraction for the perfect matching. More instructions are described in the guide of Software Epitaxy [114].

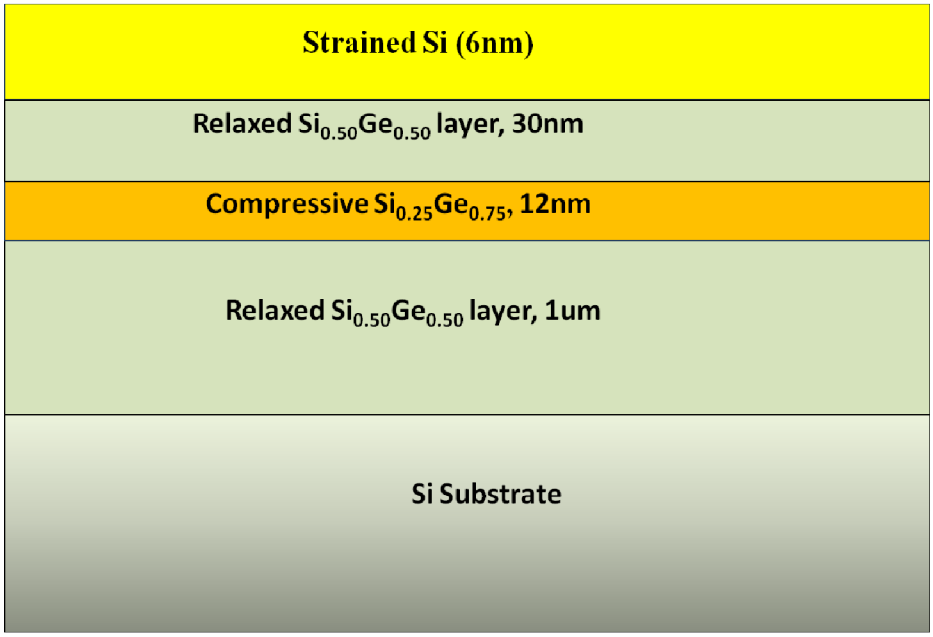

Figure C4 An identical multilayered structure built in Epitaxy simulation. The complicated graded buffer is not included.

For instance, the figures of peak matching in Epitaxy for an annealed S5075 sample (annealed at 760 °C) are shown in Figure C5. The peak from Si substrate works as the reference line. The simulated peaks from the compressive $Si_{1-y}Ge_y$ layer and bottom $Si_{1-x}Ge_x$ layer are right at the average positions of the scans at phi=0° and 180°.

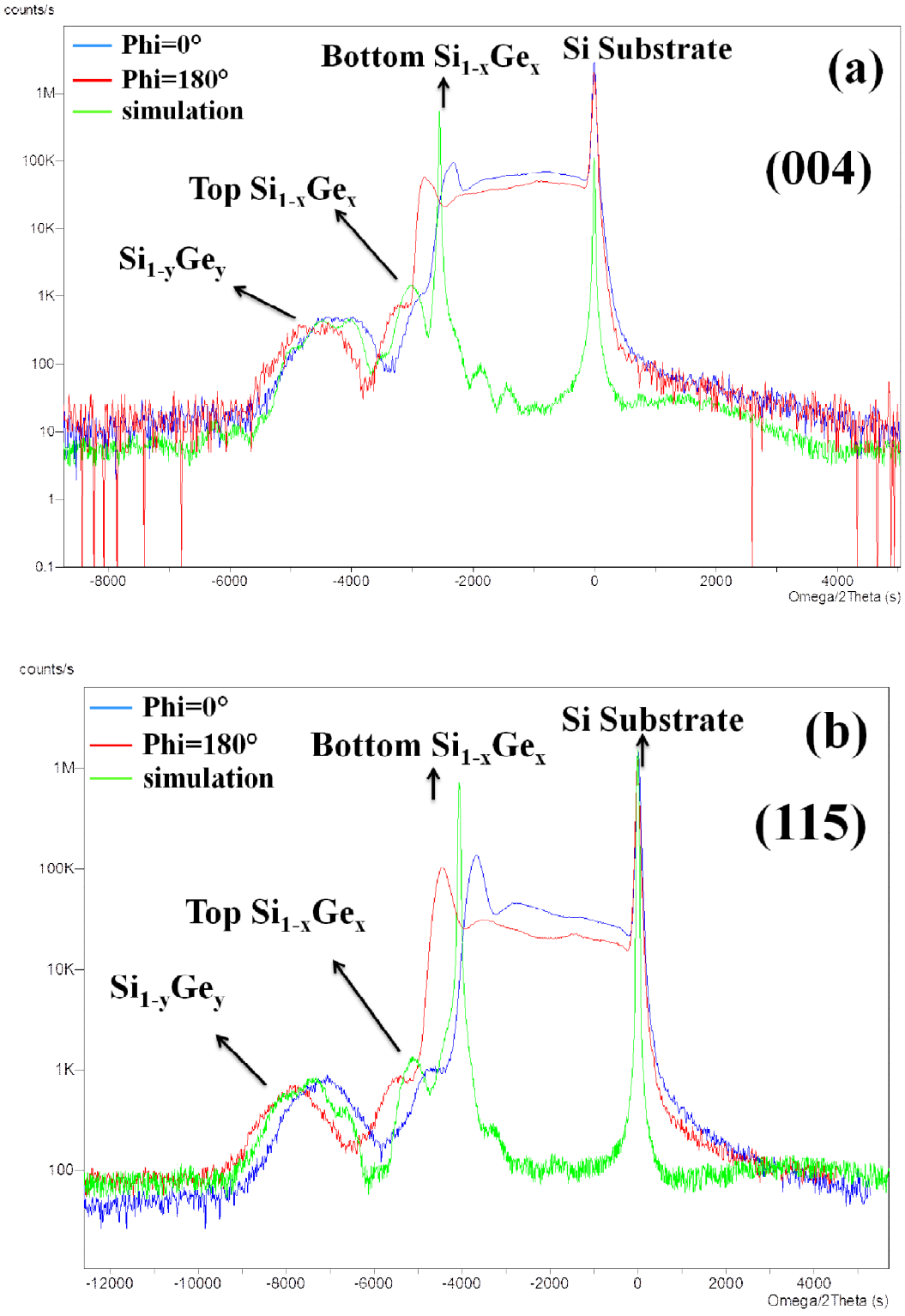

Figure C5 Peak matching in Epitaxy for annealed S5075 sample (annealed at 760 °C): (a) for 004 scans at phi=0° and 180°; (b) for (115) scans at phi=0° and 180°.

Appendix D: temperature dependence of Young's modulus and Poisson's ratio of Si and Ge, and the calculation of the biaxial Young's modulus for SiGe alloys

This appendix shows the temperature dependence of Young's modulus and Poisson's ratio of Si and Ge for interdiffusivity modeling. All the equations and data are from Aziz *et al*'s work in Ref. [37].

For biaxially strained thin films, the biaxial modulus is defined as

$$Y = E/(1-\upsilon) \qquad \text{D1}$$

where E is Young's modulus and υ is Poisson's ratio. E and υ are determined by the components of the elastic stiffness tensor or elastic compliance tensor.

For Si, temperature dependent values for the component of the elastic stiffness tensor s_{11}, and for two components of the elastic compliance tensor c_{11} and c_{12} are known. For biaxial strain in the Si (001) crystal plane, E and υ are expressed respectively as

$$\begin{aligned} E &= 1/s_{11} \\ \upsilon &= c_{12}/(c_{11}+c_{12}) \end{aligned} \qquad \text{D2}$$

For Ge, the measured values are known for c_{11} and cs, which defined as $cs = (c_{11}-c_{12})/2$. For biaxial strain in the Ge (001) crystal plane, E and υ are expressed respectively as

$$\begin{aligned} E &= cs(3c_{11}-4cs)/(c_{11}-cs) \\ \upsilon &= (c_{11}-2cs)/2(c_{11}-cs) \end{aligned} \qquad \text{D3}$$

Aziz *et al* fitted s_{11}, c_{11} and c_{12} for Si, and c_{11} and cs for Ge respectively to a quadratic function $y(T)$ of absolute temperature

$$y = aT^2 + bT + c \qquad \text{D4}$$

All the fitting parameters are shown in Table D1 as follows. And the temperature dependence of E and υ for Si and Ge is shown in Figure D1.

Table D1 Fitting parameters obtained from the best fit of empirical data to Equation D4.

Material	Elastic constants	a	b	c
Si	s_{11} (10^{-13} cm^2/dyn)	3.1020×10^{-7}	2.6613×10^{-4}	7.6626
	c_{11} (10^{11} dyn/ cm^2)	-6.4311×10^{-7}	-5.120810^{-4}	16.2250
	c_{12} (10^{11} dyn/ cm^2)	-4.1687×10^{-7}	1.769610^{-5}	5.8248
Ge	c_{11} (10^{11} dyn/ cm^2)	-4.8758×10^{-7}	-1.161210^{-3}	12.8390
	cs (10^{11} dyn/ cm^2)	-3.5593×10^{-8}	-5.157710^{-4}	4.2583

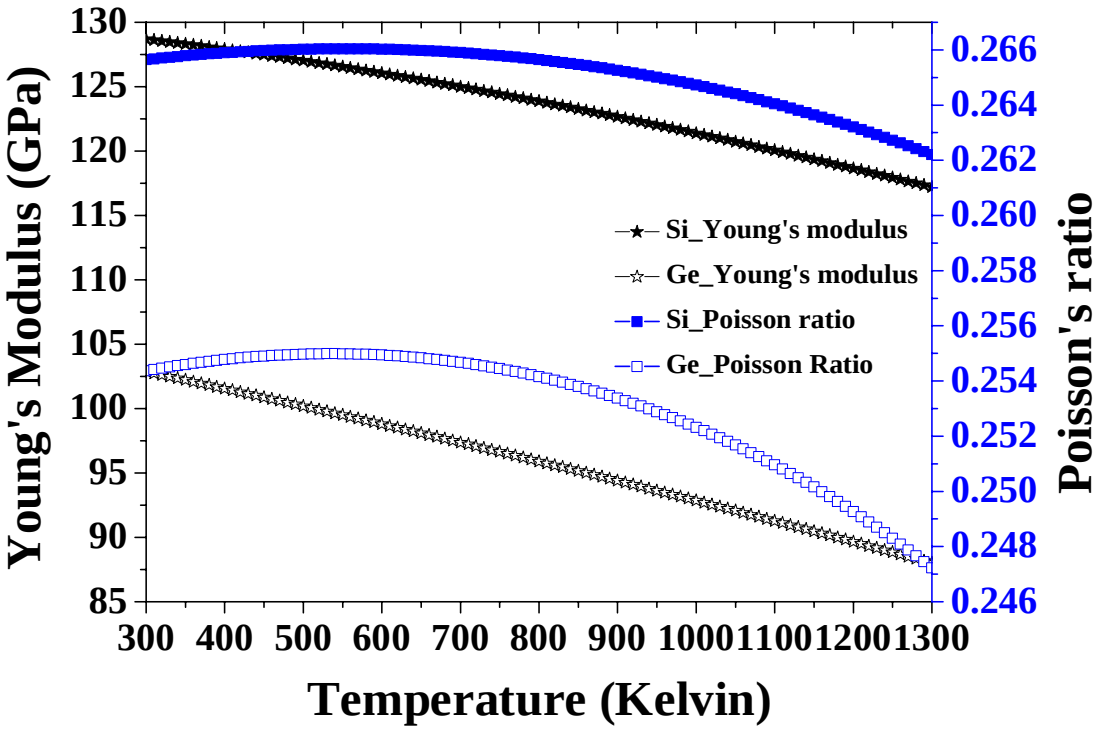

Figure D1 Temperature dependence of E and υ for Si and Ge.

Finally, the biaxial modulus $Y(T,x)$ for a $Si_{1-x}Ge_x$ alloy at temperature T is estimated by linear compostion-weighted interpolation between $Y_{Si}(T)$ and$Y_{Ge}(T)$:

$$Y(T,x) = (1-x)Y_{Si}(T) + xY_{Ge}(T) \quad \text{D5}$$